Communauté
UNIVERSITÉ Grenoble Alpes

THÈSE

Pour obtenir le grade de

DOCTEUR DE LA COMMUNAUTÉ UNIVERSITÉ GRENOBLE ALPES

Spécialité : Physique Subatomique et Astroparticules

Arrêté ministériel : 25 mai 2016

Présentée par

Romain VIROT

Thèse dirigée par **Benoit CLEMENT**
et codirigée **par Torsten SOLDNER**

préparée au sein de **L'Institut LAUE LANGEVIN**
dans **l'École doctorale de Physique**

Développement de sources de calibration pour la spectroscopie du proton

Development of calibration sources for proton spectroscopy

Thèse soutenue publiquement le **4 juillet 2017**,
devant le jury composé de :

Monsieur PATRICK NEDELEC
PROFESSEUR, UNIVERSITE DE LYON 1, Rapporteur
Monsieur CHRISTIAN WEINHEIMER
PROFESSEUR, WWU MÜNSTER - ALLEMAGNE, Rapporteur
Monsieur JEAN-MARIE DE CONTO
PROFESSEUR, UNIVERSITE GRENOBLE ALPES, Président
Monsieur ULLI KOESTER
CHERCHEUR, INSTITUT LAUE-LANGEVIN , Examinateur

Acknowledgments

As becoming a physicist was my childhood dream, I would like to gratefully and sincerely thank the two persons that allowed me to pursue this dream and who also guided and helped me during this project, Torsten Soldner and Benoit Clément.

I would like to thank all those who assisted me in one way or another for this work. The people of the SCI group for their support with the detector electronics, David Jullien for his precious advices and tools and Simon Baudoin for the LN_2 line. Didier Berruyer for the rare talent to produce with such an interest the perfectly executed exotic parts I asked for. Gertrud Konrad, as a colleague but also as a friend, thank you, notably for the electrostatic field calculation you ran for me, but particularly for just being there when I needed.

Of course I am also very grateful to all the people that I met during those few years at the ILL and that I became friend with: Andrew, Aurélien, Camille, Christoph, Damien, Fabien, Felix and Felix, Florian, Heiko, Loris, Lukas, Michi, Stefan...

I also warmly thank my friends Baj, Guillaume, John, Sébastien, Thibault...

My parents, my brother, my niece Gabriella, thank you for your presence, support and love.

My warmest and deepest thank you is of course dedicated to the one that made me find the strength to finish this work, my beloved Grumpy... and to zozolino, of course.

Abstract

Proton spectroscopy in neutron beta decay gives a complementary access to λ (ratio of the weak coupling constants $\frac{g_A}{g_V}$) and enables new searches for physics beyond the Standard Model. In experiment, low-energy protons (E$<$ 751.4 eV) are usually guided and selected using electromagnetic fields. Precise knowledge of the electrostatic potentials is mandatory as it can drastically bias proton selection. For instance, electrostatic potentials have to be known with an accuracy of a few mV in the proton spectroscopy instruments aSPECT and PERC in order to reach their aspired precision. As experimental conditions can directly impact the field (temperature effects on electrode position and work function, surface conditions, charging traps, etc.), it is mandatory that electrostatic measurements are performed in-situ. Further systematic effects are related to proton detection. In addition to prior off-line detector characterization, it is important to verify detector resolution, homogeneity, backscattering probability etc. in-situ. The protons from neutron decay itself are not suitable for this purpose because of their broad energy distribution and insufficient localization.

The goals of this project were to create calibration sources for in-situ electrostatic measurements and proton detector characterizations and to build a dedicated test setup to characterize and optimize the sources.

For electrostatic measurements, the process of positron moderation was identified as most promising. Positron moderation creates a beam of positively charged particles with a very narrow energy spread (FWHM of a few tens of meV) and with a well-defined emission angular distribution. Such a beam would allow to directly compare, inside the spectrometer, potential differences between different electrodes.

For detector characterization, available commercial proton sources are difficult to couple to high magnetic fields and often induce a deterioration of the vacuum quality in experiments, making it complicated to use detection systems at high voltage (-15 to -30 kV). Electron Stimulated Desorption (ESD) of hydrogen adsorbed on a crystal surface was found to provide the desired properties: a sharp and well-defined energy distribution of the created proton beam and compatibility with ultrahigh vacuum.

The aSPECTino spectrometer was built as test setup. It is a MAC-E filter which uses electro-magnetic fields to guide and select low-energy charged particles before detecting them in a solid-state detector. The detector is set at high voltage to post-accelerate the selected particles. The resistive coils of the spectrometer produce a magnetic field between 3.5 and 16 mT which is sufficient to confine low-energy positrons. Low-energy protons with a small radial momentum component can also be effectively guided onto the detector.

CALIPSO, which stands for CALIbration Positron/proton SOurce, is a two-in-one calibration source: one apparatus is designed to provide, not at the same time, both positrons and protons. Its core is a tungsten (110) crystal. In the case of positrons the tungsten crystal is coupled to a ^{22}Na positron source. The crystal serves as positron moderator and re-emits a fraction of the primary positrons from

the Na source, with low energy and a small angular and energy spread. In the proton configuration the same crystal is used as substrate for adsorbed hydrogen. ESD is induced by electrons emitted from a hot cathode and hitting the tungsten crystal.

This thesis introduces the physical processes used to create the low-energy positron and proton beams of CALIPSO as well as the design and the development of both the *a*SPECTino spectrometer and the CALIPSO source. It presents first experimental results of the preliminary characterizations of *a*SPECTino and CALIPSO. The expected performances of CALIPSO in both configurations and the sensitivity for comparisons of electrode potentials are derived and demonstrated by simulations.

Résumé

La spectroscopie du proton issu de la décroissance du neutron donne un accès complémentaire à λ (rapport des constantes de couplage faibles $\frac{g_A}{g_V}$) et permet la recherche de physique au-delà du Modèle Standard. Au sein des expériences, les protons de basse-énergie (E<751.4 eV) sont guidés et sélectionnés grâce à des champs électromagnétiques. La connaissance précise du potentiel électrostatique est primordiale car celui-ci peut biaiser la sélection des protons. Il faut une précision de quelques mV dans les expériences de spectroscopie du proton aSPECT et PERC pour leur permettre d'atteindre la précision de mesure désirée. Comme les conditions expérimentales impactent le champ (effets de température sur la position des électrodes et leur fonction de travail, condition de surface, pièges qui se chargent etc.), il est nécessaire de pouvoir effectuer la mesure du champ électrostatique in-situ. D'autres effets systématiques sont reliés à la détection de protons: résolution du détecteur, homogénéité, probabilité de rétrodiffusion etc. in-situ.

Les objectifs de ce projet sont de créer des sources de calibration pour des mesures électrostatiques in-situ et la caractérisation de détecteurs de protons et de construire une chambre d'essai dédiée à la caractérisation et l'optimisation des sources.

Pour les mesures électrostatiques, la modération des positrons a été identifiée comme prometteuse. Ce processus crée un faisceau de particules chargées positivement avec une largeur spectrale très faible (FWHM de quelques dizaines de meV) et avec une distribution angulaire bien définie. Un tel faisceau pourrait permettre de comparer, au sein du spectromètre, les différences de potentiels entre des électrodes.

Pour la caractérisation des détecteurs, les sources de protons disponibles sur le marché sont difficiles à coupler aux forts champs magnétiques et induisent souvent une détérioration de la qualité du vide dans les expériences, rendant ardue l'utilisation d'un détecteur sous haute tension (entre -15 et -30 kV). La Désorption Stimulée par Electrons (ESD) de l'hydrogène adsorbé sur la surface d'un cristal s'avère posséder les qualités requises: une distribution en énergie piquée et bien définie et une compatibilité avec l'ultravide.

Le spectromètre aSPECTino a été créé en tant que système de test. C'est un filtre MAC-E qui utilise des champs EM pour guider et sélectionner les particules chargées de basse énergie avant de les détecter à l'aide d'un détecteur sous haute tension pour accélérer les particules sélectionnées. Dans le spectromètre règne un champ magnétique entre 3.5 et 16 mT qui est suffisant pour confiner les positrons de basse-énergie. Les protons de basse-énergie avec un faible moment radial peuvent aussi être guidés vers le détecteur.

CALIPSO, qui signifie CALIbration Positron/proton SOurce, est une source de calibration deux en un : elle peut fournir indépendamment des positrons et des protons et est basée autour d'un cristal de tungstène (110). Pour la source de positrons ce cristal est couplé à une source de positron ^{22}Na. Il sert alors de modérateur et réémet une fraction des positrons primaires issus de la source

^{22}Na avec une faible énergie et une distribution angulaire et spectrale étroite. Dans la configuration proton le même cristal est utilisé en tant que substrat pour l'adsortion d'hydrogène. L'ESD est induit par les électrons émis par une source thermoionique et frappants le cristal de tungstène.

Cette thèse présente les processus physiques utilisés pour créer les faisceaux de positrons et de protons de basse-énergie de CALIPSO ainsi que la conception et le développement du spectromètre aSPECTino et de la source CALIPSO. Elle présente les premiers résultats expérimentaux de la caractérisation préliminaire d'aSPECTino et de CALIPSO. Les performances attendues de CALIPSO pour ses deux configurations et pour la sensibilité de comparaison des potentiels d'électrodes sont dérivés et démontrés à l'aide de simulations.

Contents

Page

List of Figures xi

List of Tables xv

1. Introduction 1
   1.1. Need for a moderated positron calibration source 5
   1.2. Need for a low-energy proton calibration source 8
   1.3. Developing the calibration sources 9

2. Electron-Stimulated Desorption 11
   2.1. The MGR model 12
      2.1.1. General description 12
      2.1.2. Escape probability 13
      2.1.3. Limits of the model 15
   2.2. Hydrogen on tungsten (110) 15
      2.2.1. Tungsten (110) 15
      2.2.2. Adsorption process 16
      2.2.3. Proton desorption 18
   2.3. Expected output properties 18

3. Positrons in matter 21
   3.1. Properties and creation of positrons 22
   3.2. Positron interactions in a metal 23
      3.2.1. Positron backscattering and diffraction 23
      3.2.2. Thermalization and diffusion 25
   3.3. Re-emission of moderated positrons 27
      3.3.1. Work function 28
      3.3.2. Re-emission efficiency 29
      3.3.3. Typical output properties 31

4. Geant4 simulations 35
   4.1. Structure of the Geant4 simulations 36
      4.1.1. Generation of primary events 38
      4.1.2. Definition of the system geometry 39
      4.1.3. Simulation output 40
   4.2. Integration of Electro-Magnetic fields 41
      4.2.1. Structured vs un-structured grids 41
      4.2.2. Field computation 42
      4.2.3. Field interpolation for structured grids 44
      4.2.4. Un-structured grids 45

4.3. Moderated positron re-emission process . . . 51
4.3.1. Estimation of the process . . . 52
4.3.2. Implementation in Geant4 . . . 52
4.4. Data analysis tools . . . 53
4.4.1. ROOT . . . 53
4.4.2. Data analysis program . . . 54

5. The *a*SPECTino spectrometer 57
5.1. MAC-E filter concept . . . 58
5.1.1. Particle transport in EM fields . . . 59
5.1.2. Transmission function . . . 62
5.2. Design and characteristics of the spectrometer . . . 64
5.2.1. Vacuum chamber . . . 64
5.2.2. Magnetic field . . . 67
5.2.3. Electrostatic field . . . 71
5.3. Detection system . . . 72
5.3.1. Data acquisition system . . . 74
5.3.2. Detector calibration . . . 76

6. The CALIPSO source 81
6.1. Design of the apparatus . . . 82
6.1.1. Gas inlet . . . 85
6.1.2. Moderated positron source . . . 86
6.1.3. Proton source . . . 90
6.2. Crystal holder . . . 92
6.2.1. Cold source . . . 92
6.2.2. Crystal block . . . 93
6.2.3. Piezo motor . . . 95

7. Results and outlook 99
7.1. Preliminary tests of the crystal holder . . . 99
7.1.1. Cold source . . . 100
7.1.2. Crystal cleaning and annealing . . . 102
7.2. Procedure for potential comparison . . . 106
7.3. Strong magnetic field environment . . . 110
7.3.1. Positron configuration . . . 110
7.3.2. Proton configuration . . . 111

Conclusion 113

A. Data analysis program 115

B. Multi-channel power supply 119

C. Lead-castle for the ^{22}Na source 123

D. Résumé en Français 127
D.1. Introduction . . . 127
D.1.1. Nécessité d'une source de calibration de positrons modérés 127
D.1.2. Nécessité d'une source de calibration de protons . . . 128

D.1.3. Développement des sources de calibration 128
D.2. La désorption stimulée par électrons (ESD) 129
D.2.1. Le modèle MGR 129
D.2.2. L'hydrogène sur du tungstène (110) 130
D.3. Les positrons dans la matière 131
D.3.1. Propriétés et création des positrons 131
D.3.2. Intéractions des positrons dans le métal 132
D.3.3. La ré-émission de positrons modérés 133
D.4. Simulations Geant4 134
D.4.1. Structure des simulations Geant4 134
D.4.2. Intégration des champs électromagnétiques 134
D.4.3. Processus de réémission des positrons modérés 135
D.4.4. Programme d'analyse des données 135
D.5. Le spectromètre *a*SPECTino 136
D.5.1. Filtre MAC-E 136
D.5.2. Description du spectromètre 136
D.5.3. Système de détection 137
D.6. La source CALIPSO 137
D.6.1. Conception de la source 138
D.6.2. Support du cristal 138
D.7. Résultats et perspectives 139
D.7.1. Tests préliminaires du support du cristal 139
D.7.2. Procédure pour la comparaison des potentiels 140
D.7.3. Comportement sous champ magnétique intense 140
D.8. Conclusion 141

Bibliography **143**

List of Figures

Page

1.1. Classification of elementary particles of the Standard Model . . . 2
1.2. Free neutron β-decay correlation coefficients 4
1.3. Potential barrier accuracy impact on a correlation coefficient . . . 5
1.4. Temperature dependency of the work function 7

2.1. Potential energy curves and critical position in the MGR model . 14
2.2. Tungsten (110) bulk and surface structure 16
2.3. Proton ESD yield dependencies 17
2.4. Proton ESD threshold behavior 18
2.5. Proton ESD rate for the H-W110 system 19
2.6. Energy and angular spread of proton ESD from tungsten 20

3.1. Interactions of a positron beam with a solid 24
3.2. Backscattering probabilities for positrons 25
3.3. Makhovian implantation profile of positrons in tungsten 26
3.4. Feynman diagram of positron annihilation 27
3.5. Ps annihilation spectra 28
3.6. Work function of a surface 29
3.7. Positron source/moderator geometries 31
3.8. Angular distribution and energy spread of re-emitted positrons . . 33

4.1. Global structure of the simulations 36
4.2. Geant4 file structure 37
4.3. Geant4 stepper precision 38
4.4. Geant4 events and tracks 38
4.5. Geometry: from SolidWorks to Geant4 39
4.6. ROOT output file structure 40
4.7. Structured grid problematic behavior near boundaries 42
4.8. Example of a 3D un-structured mesh mapping 43
4.9. Flowchart of the magnetic field map interpolation routine 44
4.10. Bi and tri-linear interpolation scheme for structured grids 45
4.11. Description of the tree structure 46
4.12. Quadtrees and Kd-trees description 47
4.13. Cell duplication problem on Quadtrees and Kd-trees 48
4.14. Celltree construction scheme 49
4.15. Bi and tri-linear interpolation scheme for un-structured grids . . . 51
4.16. Test routine for moderated positron re-emission 53
4.17. Screenshot of the data analysis tool 55

5.1. Principle of the aSPECTino spectrometer 60
5.2. $\mathbf{E} \times \mathbf{B}$ drift 61
5.3. Magnetic mirror effect 62
5.4. Picture of the aSPECTino spectrometer 64
5.5. aSPECTino experimental zone 65
5.6. Scheme of the aSPECTino spectrometer 66
5.7. Maxwell coils 68
5.8. Simulation of the magnetic field in aSPECTino along z 69
5.9. Larmor radius calculations in aSPECTino 70
5.10. Pictures of some aSPECTino coils 70
5.11. aSPECTino electrodes 72
5.12. Detector setup 73
5.13. Preamp signal seen on a scope 74
5.14. ADC card box 75
5.15. ^{133}Ba simulated spectrum 77
5.16. ^{133}Ba measured spectrum 78
5.17. Positrons simulated spectrum compared to measured background 78

6.1. Picture of the main components of CALIPSO 83
6.2. Scheme of the CALIPSO source 85
6.3. Scheme of the aSPECTino source cross 86
6.4. Scheme of the positron configuration of CALIPSO 87
6.5. ^{22}Na simulated positron spectrum 88
6.6. Plans of the ^{22}Na source capsule 89
6.7. Electric potentials inside CALIPSO 89
6.8. Low-energy positrons extraction 90
6.9. Positron beam distortion due to $\mathbf{E} \times \mathbf{B}$ fields 91
6.10. Exploded view of the crystal holder 93
6.11. Open view of the crystal holder 95
6.12. Pictures of the crystal heater 96
6.13. Side view of the crystal heater and crystal temperature sensor . . 96
6.14. Picture of the CALIPSO piezo rotator 97

7.1. Crystal holder installation in aSPECTino 100
7.2. Cooling of the crystal holder 101
7.3. Thermal radiation screen for the crystal holder 102
7.4. Tungsten crystal cleaning and annealing procedure 103
7.5. Picture of the hot cathode of the crystal heater 104
7.6. Temperature response of the crystal holder to a heat-load 104
7.7. Picture of the damaged part of the crystal holder 105
7.8. Zoom on the tungsten disk and tantalum plates 105
7.9. Principle of potentials comparison in aSPECT using CALIPSO . 109
7.10. Proton configuration in strong a magnetic field 111

A.1. Data analysis program screenshot 1 116
A.2. Data analysis program screenshot 2 117

B.1. Multi-channel power supply PCB plan 120
B.2. Multi-channel power supply PCB scheme 120
B.3. Front panel of the multi-channel power supply 121
B.4. View of the inside of the multi-channel power supply 121
B.5. Output of the multi-channel power supply 122

C.1. Closed ^{22}Na source lead castle 124
C.2. Opened ^{22}Na source lead castle 124
C.3. Lock of the ^{22}Na source lead castle 125

List of Tables

Page

1.1. Electron work function of several metals 7

3.1. e^+ properties 22
3.2. e^+ radioactive sources 23
3.3. Electron and positron work function values of several materials . . 30
3.4. Positron moderators diffusion length and typical efficiency 32

5.1. Earth magnetic field in the experimental area 68
5.2. *a*SPECTino coils characteristics 71
5.3. ^{133}Ba source low-energy photons 76

6.1. CALIPSO feedthroughs and connectors 84

7.1. Results of potentials comparison simulation 107

Chapter 1

Introduction

Almost in the beginning was curiosity.

(Isaac Asimov, The Intelligent Man's Guide to the Physical Sciences)

Contents

1.1. Need for a moderated positron calibration source . . 5
1.2. Need for a low-energy proton calibration source . . . 8
1.3. Developing the calibration sources 9

The 20$^{\text{th}}$ century saw the emergence of many major breakthroughs in physics and an impressive development of particle physics in particular. One can for instance cite the confirmation of the atomic structure of matter in 1911 [Rut11], the discovery of the neutron in 1932 [Cha32] or the proposition of the quark model in 1964 [GM64, Zwe64] and its confirmation in 1968 [B$^+$69a, B$^+$69b]. The will to identify and classify elementary particles and their interactions led to the creation of the Standard Model of particle physics (SM) in the 1960's. After several evolutions, directed by both theoretical and experimental researches, the current formulation was finalized in the mid 1970's[1], resulting in a theory that describes the electromagnetic, weak, and strong interactions. A table of all known elementary particles is shown in Figure 1.1. The SM is a great success and offers very precise predictions, such as for the electron magnetic moment, measured to 3 parts in 10^{13} [HFG08] or the proof of the existence of the Higgs field by the discovery of the Higgs boson in 2012 [A$^+$12, C$^+$12], 48 years after its prediction [EB64, Hig64, GHK64]. However it fails to explain several crucial phenomena of the universe, like the baryon asymmetry or the existence and nature of dark matter.

The SM is expected to be a low-energy limit of a larger framework, whose Beyond the Standard Model (BSM) physics should emerge above a certain mass

[1] This work awarded Glashow, Weinberg and Salam the Nobel Prize in Physics in 1979.

scale Λ_{BSM}, supposedly of the order of one TeV or above [CRM13]. The approach of high-energy physics of searching for BSM physics is to directly create new particles from ultra-relativistic particle collisions, as in the case of the LHC at CERN which produces proton-proton collisions with an energy, in the center of mass frame, of around 13 TeV [CER17b]. On the other hand, as virtual effects due to BSM physics can appear well below Λ_{BSM} [Sig14], many high-precision, low-energy experiments are performed and search for tiny deviations from the SM predictions which, if detected, would imply BSM processes. Such researches are complementary to direct production methods performed in high-energy physics[2].

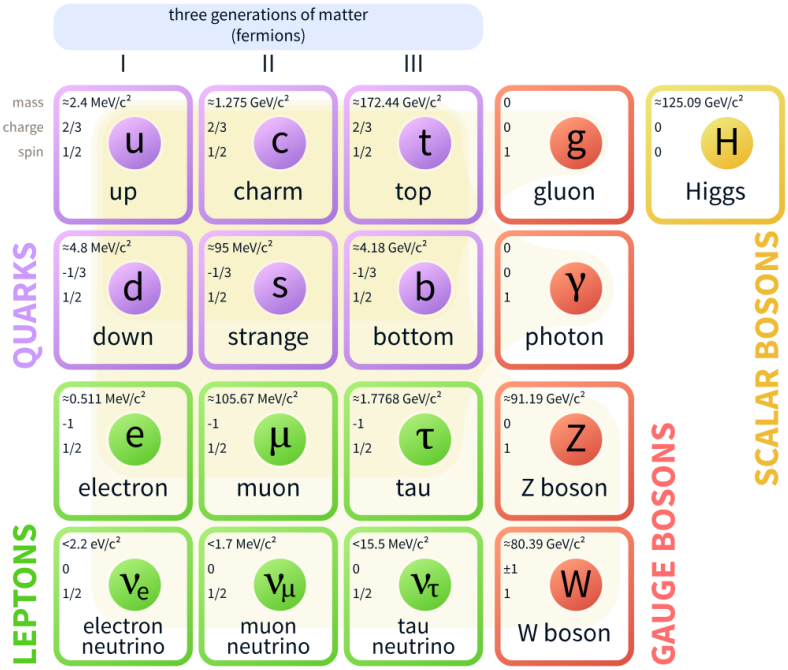

Figure 1.1. Classification of the elementary particles of the Standard Model of particle physics. All those particles can be sorted into two families: fermions and bosons. Fermions have a half-integer spin (1/2 in the case of elementary particles), are all massive[3]and both quarks and leptons can be sorted into three generations. Bosons on the other hand have an integer spin and can be massless, as in the case of gluons and photons. Gauge bosons carry the three fundamental forces considered in the SM: gluons for the strong nuclear force, photons for the electromagnetic force and Z^0 and $W^{\pm}$ for the weak force. As gravity is not part of the SM there are no bosons mediating this force in this theory. The Higgs field gives a mass to the fermions and the weak force bosons. Image taken from [Wik17a].

[2]High-energy physics is not limited to a direct production approach and is also sensitive to virtual processes.

[3]Even though only upper limits can be set on the mass of neutrinos, the discovery of neutrino oscillations implies that they are not massless [F+98, A+01, A+02].

The free neutron is an unstable particle that decays with a lifetime $\tau = 880.2 \pm 1.0$ s [P+16]:

$$n \rightarrow p + e^- + \overline{\nu_e} + 782 \text{ keV}. \tag{1.1}$$

This β-decay is a very popular low-energy BSM probe as it is described in the SM by only three parameters while there are more than a dozen observables. There are also no nuclear structure corrections to be considered, resulting in a clean and over-determined system. The triple differential decay rate of neutrons, neglecting the neutrino masses, can be written as [Jac98]:

$$\begin{aligned} \mathrm{d}^3\Gamma = & \frac{1}{(2\pi)^5}\frac{G_\mathrm{F}^2|V_\mathrm{ud}|^2}{2} p_\mathrm{e} E_\mathrm{e} \left(E_0 - E_\mathrm{e}\right)^2 \mathrm{d}E_\mathrm{e}\mathrm{d}\Omega_\mathrm{e}\mathrm{d}\Omega_\nu \\ & \times \xi \left[1 + a\frac{\mathbf{p}_\mathrm{e}\cdot\mathbf{p}_\nu}{E_\mathrm{e}E_\nu} + b\frac{m_\mathrm{e}}{E_\mathrm{e}} + \frac{\langle \mathbf{s}_\mathrm{n}\rangle}{s_\mathrm{n}}\left(A\frac{\mathbf{p}_\mathrm{e}}{E_\mathrm{e}} + B\frac{\mathbf{p}_\nu}{E_\nu} + D\frac{\mathbf{p}_\mathrm{e}\times\mathbf{p}_\nu}{E_\mathrm{e}E_\nu}\right)\right], \end{aligned} \tag{1.2}$$

where G_F is the Fermi weak coupling constant, V_ud is the upper left element of the Cabibbo-Kobayashi-Maskawa (CKM) matrix[4], $\mathbf{p}_\mathrm{e}$, $\mathbf{p}_\nu$, E_e and E_ν are respectively the electron (neutrino) momenta and total energies, E_0 is the electron spectrum endpoint total energy, m_e is the electron mass, $\mathbf{s}_\mathrm{n}$ is the neutron spin and Ω_i correspond to the solid angles. ξ is a factor which is inversely proportional to the neutron decay rate. a, A, B and D are the angular correlation coefficients, shown in Figure 1.2 and b is the Fierz interference term. We can also define the proton asymmetry relative to the neutron spin C in analogy to the β asymmetry A or the neutrino asymmetry B. A, B and C are related by kinematics:

$$C = -x_\mathrm{C}(A + B), \tag{1.3}$$

with $x_\mathrm{C} = 0.27484$ being a kinematical factor. Within the framework of the SM, we can express the angular correlation coefficients a, A, B and C as [Kon11]:

$$\begin{aligned} a &= \frac{1-|\lambda|^2}{1+3|\lambda|^2}, & A &= -2\frac{|\lambda|^2 + |\lambda|\cos\phi}{1+3|\lambda|^2}, \\ B &= 2\frac{|\lambda|^2 - |\lambda|\cos\phi}{1+3|\lambda|^2}, & C &= x_\mathrm{C}\frac{4|\lambda|\cos\phi}{1+3|\lambda|^2}, \end{aligned} \tag{1.4}$$

with $\lambda = L_\mathrm{A}/L_\mathrm{V}$ is the ratio of the weak axial-vector ($L_\mathrm{A}G_\mathrm{F}V_\mathrm{ud}$) to the vector coupling constant ($L_\mathrm{V}G_\mathrm{F}V_\mathrm{ud}$) and ϕ the phase angle between them. λ, while not being a fundamental quantity, plays an important role in many fields, like in particle physics, astrophysical processes or even neutrino detector calibrations for example [Abe08].

[4]The CKM matrix, also known as the quark-mixing matrix, informs on the strength of flavour-changing weak decays of quarks.

The sensitivities of a, A, B and C towards λ near the world average value ($\lambda = -1.2723(23)$ [P+16]) are [Abe08]:

$$\frac{da}{d\lambda} = 0.298, \qquad \frac{dA}{d\lambda} = 0.374, \tag{1.5}$$

$$\frac{dB}{d\lambda} = 0.076, \qquad \frac{dC}{d\lambda} = -0.124. \tag{1.6}$$

Among these correlation coefficients several are related to the detection or precise spectroscopy of protons issued from the decay, like the proton asymmetry parameter C or the electron-antineutrino correlation parameter a. As shown in Equations 1.2 and 1.5 a is very sensitive to λ and, contrary to the β asymmetry A, is not correlated to the neutron spin. Precise measurements of a are of particular interest in order to determine λ with a completely different systematics than via the β asymmetry. This correlation coefficient can be derived from the precise measurement of the proton recoil spectrum. On the other hand coefficients B and C are quite insensitive to λ and open the possibility to search for new physics, for example through constraints on possible right-handed currents (V+A) or scalar or tensor-like interactions [CGH13]. Furthermore C only requires the detection of protons and is therefore in principle easier to measure than B, which requires coincident detection of electron and proton.

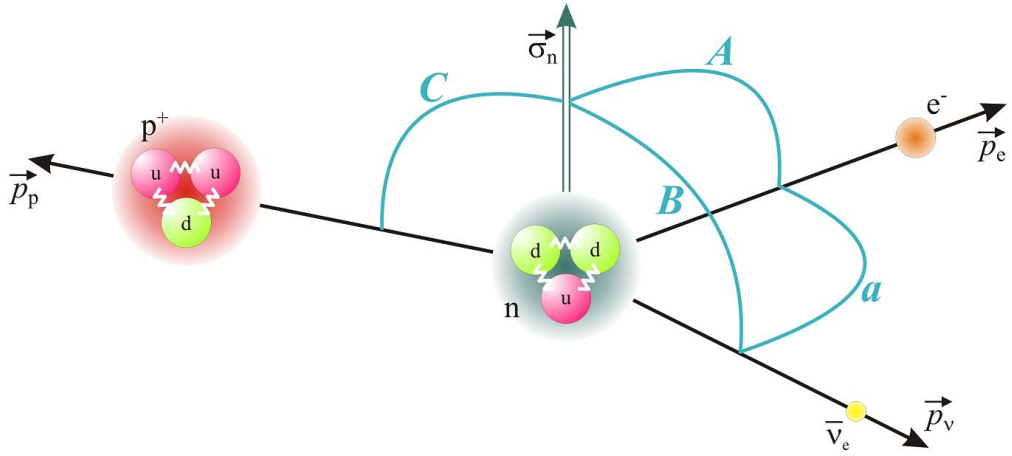

Figure 1.2. Free neutron β-decay and some of the corresponding correlation coefficients. The proton asymmetry parameter C describes the correlation between the neutron spin and the proton momentum whereas the electron-antineutrino correlation parameter a can be derived from the measurement of the proton recoil spectrum. Image taken from [Kon11].

1.1. Need for a moderated positron calibration source

Protons issued from the free neutron β-decay have a low energy ($E_k \leq 751$ eV) and measuring precisely their recoil spectrum is therefore a sensitive task. They are usually guided and selected using electro-magnetic fields and small undesired electrostatic potentials can alter the measurement, inducing a systematic error. For instance the aSPECT experiment [ZBvdG+00, GBB+04] is dedicated to the measurement of the electron-antineutrino correlation parameter a by measuring the proton recoil spectrum using a MAC-E filter[5] [BPT80]. Figure 1.3 shows the impact of a shift in the selection potential compared to the potential where protons are created: those potentials have to be known with an accuracy of 7 mV to reach the aspired precision of the experiment $\Delta a/a = 0.3\%$ [Kon11]. Other experiments, such as PERC[6] or Nab[7], require the same order of magnitude for the electrostatic field accuracy [K+12, P+09]. State-of-the-art and next generation proton spectroscopy experiments therefore require an in-depth analysis of the electrostatic field along the proton trajectory.

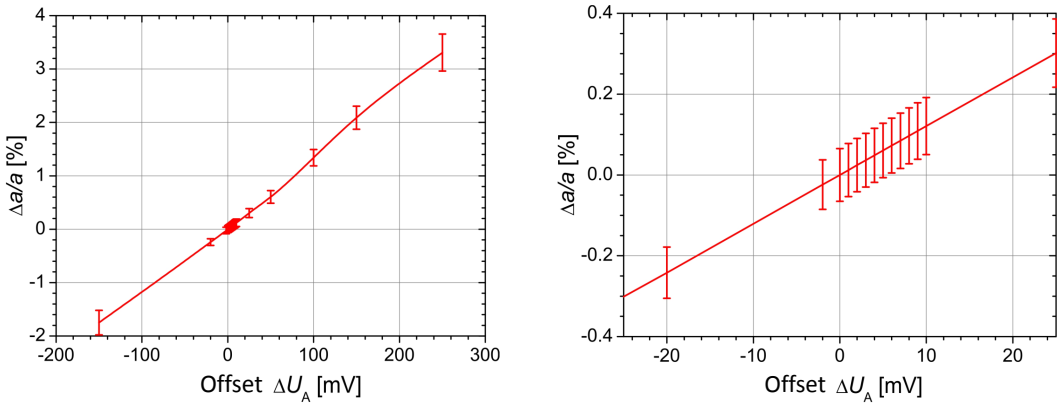

(a) (b)

Figure 1.3. (a): Sensitivity of the measurement of the electron-antineutrino correlation coefficient a to an offset of the potential barrier U_A used for proton selection in the aSPECT spectrometer. (b): Zoom of Figure 1.3a: an offset of 20 mV for U_A induces a shift of $\Delta a/a = 0.25(5)\%$. Both figures are taken from [Kon11].

[5] A MAC-E filter (Magnetic Adiabatic Collimation combined with an Electrostatic field) uses electro-magnetic fields to precisely select charged particles. Such setup is typically used for low-energy charged particles and when a high resolution is required. More details are given in Section 5.1.

[6] The PERC (Proton and Electron Radiation Channel) facility is a next-generation free neutron β-decay apparatus which is being built at the FRM-II in Munich, Germany. It aims to "deliver an intense beam of decay electrons and protons, under well defined and precisely variable conditions" and to perform measurements in the 10^{-4} level [K+12].

[7] The Nab instrument is developed at the SNS of the Oak Ridge National Laboratory, USA. It is dedicated, amongst others, to the measurement of the electron-antineutrino correlation parameter a with an accuracy at the 10^{-3} level [P+09].

In order to determine those potentials the electron work function (eWF) of the electrodes have to be measured. This surface property corresponds to the energy required to extract an electron from the bulk of the electrode into the vacuum and therefore shifts the vacuum potential produced by an electrode compared to the potential applied to the electrode. Work function[8] is more precisely described in Section 3.3.1. eWF of the electrodes of the apparatuses are generally measured using a Kelvin probe scanner[9]. This measurement cannot be performed in-situ and usually implies the electrodes to be cut in small parts so they could fit in the Kelvin probe. As a result this procedure is performed once the measurement is finished and the corrections are applied afterwards. Difficulties arise from the differences in conditions between the measurement routine of the experiment and the electrode eWF measurement. The work function value is sensitive to many parameters, such as:

- **Crystallographic orientation of the surface:** as detailed in Section 3.3.1 the surface of a polycrystalline metal exhibits different WF values, depending on the crystallographic orientation of each surface cluster. This leads to a patch effect whose range is the maximum WF difference between two possible crystallographic orientations. In order to minimize this effect the electrodes are usually coated using gold, which exhibits a small eWF difference between its different orientations compared to other metals, as shown in Table 1.1.
- **Temperature of the electrode:** the WF dependency on the temperature is complex and affects materials and their respective crystallographic orientations in different ways. The work function can be decomposed in two components [Kie86]:

  $$\varphi = \varphi_{\mathrm{u}} + \delta_{\varphi_{\mathrm{hkl}}}, \tag{1.7}$$

  with φ the total WF value, φ_{u} the uniform part of the WF, which exhibits a linear dependency to the temperature, and $\delta_{\varphi_{\mathrm{hkl}}}$ the WF lattice correction, all expressed in eV. The latter is the dominant term with an effect that can shift the WF value by up to around ± 1 meV/K. Calculated values of $\delta_{\varphi_{\mathrm{hkl}}}$ are shown for Na and Al in Figure 1.4 as examples.
- **Surface contamination:** both the nature and the coverage ratio of contaminants (i.e., adsorbates) affect the WF value of a surface, which can result in either a positive shift in the case of electronegative adsorbates or a negative shift for electropositive ones [Kaj10]. This effect can be so strong that it can be used to determine the adsorption coverage of certain

[8] The term work function (WF) refers to both electron work function (eWF) and positron work function.

[9] A Kelvin probe measures the contact potential difference between two materials: the sample and the probe. Through a physical contact between the two objects the Fermi levels of the sample and the Kelvin probe tip will align, creating a potential difference between the two. The opposite potential applied to reach a null charge state corresponds to the contact potential difference between the tip of the Kelvin probe and the sample. Using a well defined reference sample with a precisely known eWF, a Kelvin probe can measure absolute eWF with a resolution of the order of a few meV under proper conditions.

adsorbed species, as in the case of alkali metal adsorbates on a metallic surface [GR70].

Table 1.1. Electron work function values for different metals and crystallographic orientations. The absolute maximum difference between shown orientations is also indicated. Values taken from [Hay16].

	Electron WF Φ_- (eV)			
	Orientation			
Material	(100)	(110)	(111)	$\lvert\Delta_{\Phi_{-\max}}\rvert$ (eV)
Ag	4.64	4.52	4.74	0.22
Al	4.20	4.06	4.26	0.20
Au	5.47	5.37	5.31	0.16
Cu	5.10	4.48	4.94	0.62
Ni	5.22	5.04	5.35	0.31

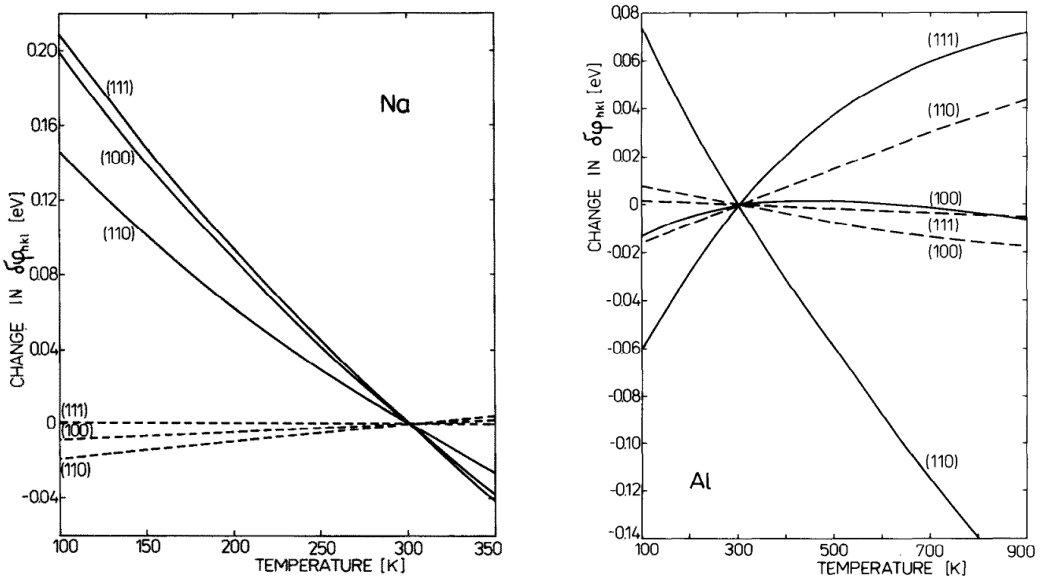

(a) (b)

Figure 1.4. (a): Impact of the temperature on the electron work function lattice correction value $\delta_{\varphi_{\mathrm{hkl}}}$ of sodium for three low-index faces. The dashed lines represent the thermal expansion contribution while the full lines also consider the lattice vibration effect, which is the dominant contributor to $\delta_{\varphi_{\mathrm{hkl}}}$. (b): Same as Figure 1.4a but for aluminum. Both figures taken from [Kie86].

Because of the high magnetic field required to confine protons, proton spectroscopy experiments usually use supra-conducting coils and the inside of the

vacuum vessel is often at a low-temperature. In addition to the direct WF shift described above, this can affect the electrode system in many ways: shrinking of the electrodes, displacement or surface contamination by rest gas condensation for example.

All of those effects impact the electrostatic field of the apparatus in ways that are very difficult to reproduce in different setups (e.g., a Kelvin probe apparatus). Therefore, for an electrostatic field accuracy of a few tens of mV or less, it is crucial, if not mandatory, to scan the electrostatic field in-situ, in real measurement conditions.

A calibration source of positively charged particles with a very narrow energy spread could fulfill this need. In theory a very well defined proton calibration source would be the perfect candidate but a low-enough energy spread (i.e., of the order of a few tens of meV) is in practice impossible to achieve. Positrons, electrons' anti-particles, carry the same positive charge as protons and a moderated positron calibration source can provide positrons with a very sharp energy distribution. Through positron-specific processes, a high-energy beam ($0 \leq E \leq \sim 1$ MeV) of primary positrons issued from a radioactive source and hitting a well-prepared positron moderator can create a well defined (Full Width at Half Maximum (FWHM)$\sim$ 40 meV) beam of low-energy ($E \sim 3$ eV) positrons. The application of a calibration source of this kind would offer a real answer to the emerging problem of the electrostatic field accuracy in proton spectroscopy experiments.

1.2. Need for a low-energy proton calibration source

Many commercial proton source are available on the market and are based on the extraction of ions from a plasma. This plasma is built from a hydrogen gas which is ionized using electrons. Such setups require differential pumping and usually operate at pressures between 10^{-5} mbar and 10^{-8} mbar. The induced vacuum deterioration in UHV systems can be fatal for sensitive solid-state detectors used in proton spectroscopy which are usually held at high-voltage [Bor10]. Furthermore those sources usually use strong electric and/or magnetic fields to confine electrons and maximize the ion production. This kind of technology is not well-adapted to the needs for a in-situ proton calibration source for free neutron β-decay experiments.

Another physical process, issued from surface science, could be used to create a low-energy and low-intensity beam of protons: Electron-Stimulated Desorption. By first covering a well-defined surface with hydrogen atoms and then bombarding it with low-energy electrons, protons can be desorbed from the surface without the need for a plasma or any kind of confinement. The creation of a low-intensity and low-energy proton beam with a non-perturbing source could allow to characterize proton detectors safely, in-situ. Such characterizations could not be efficiently performed with a positron source as their interactions with matter differ a lot (e.g., different back-scattering ratios, energy deposition in the entrance

dead layer, ionisation density etc.). Furthermore, in the case of MAC-E filter spectrometers, to provide an accurate knowledge of the transmission function[10] by directly scanning it.

1.3. Developing the calibration sources

This thesis focuses on two major and complementary topics: the creation of a low-energy charged particle spectrometer named *a*SPECTino and the creation of a two-in-one (proton and positron) low-energy calibration source named CALIPSO.

The *a*SPECTino spectrometer was designed and built first since it was a required apparatus to develop and test the CALIPSO source. This three meters long apparatus uses resistive coils to guide charged particles which are then detected using a solid state detector set at high-voltage. Electrodes can be installed along the particles path in order to select them.

Concerning the CALIPSO source, the initial project was to develop two different calibration sources: one of moderated positrons, to scan electrostatic fields inside experiments, and one of low-energy protons to characterize proton detectors. During the first phase of the sources development the possibility to create a single apparatus that could be used to create both kind of low-energy particles (protons and moderated positrons) emerged. As a result the CALIPSO source was designed with the goal of emitting low-energy protons and moderated positrons, not at the same time, with very little modifications to the setup. It was also conceived as compact (approximately the size of a can) and as mobile as possible.

This work was conducted at the Institut Laue-Langevin (ILL) in Grenoble, France, in the Nuclear and Particle Physics group. Chapters 2 and 3 introduce the physics related to the creation of the low-energy proton and positron beams with CALIPSO. Chapter 4 details the structure of the simulations that were used to develop both the *a*SPECTino spectrometer and the CALIPSO source. The concept, design and characteristics of *a*SPECTino and CALIPSO are respectively presented in Chapter 5 and Chapter 6 while Chapter 7 describes the different characterizations that should be performed on the CALIPSO source. Finally Appendices A to C detail several technical elements of this work: the data analysis software, the multichannel current supply and the lead castle for the ^{22}Na source.

[10] The transmission function is the response of the spectrometer: it describes under which conditions (energy, emission angle, selection potential etc.) a charged particle will be reflected or not by the selection potential of the apparatus. More details can be found in Section 5.1.2.

Chapter 2

Electron-Stimulated Desorption

> Self-education is, I firmly believe, the only kind of education there is.
>
> *(Isaac Asimov, In Science Past, Science Future (1975), 208)*

Contents

2.1. The MGR model 12
2.1.1. General description 12
2.1.2. Escape probability 13
2.1.3. Limits of the model 15
2.2. Hydrogen on tungsten (110) 15
2.2.1. Tungsten (110) 15
2.2.2. Adsorption process 16
2.2.3. Proton desorption 18
2.3. Expected output properties 18

One task of the CALIPSO source is to provide a proton beam with a well-defined and narrow energy, without degrading the vacuum. This chapter will demonstrate by a review of literature that ESD is a suitable process to fulfill these requirements. Principles important for this work will be introduced.

Historically surface chemistry used to revolve around thermal excitation and desorption[1] of adsorbed species and the use of single crystal surfaces in such studies only started in the 1960's. Even though desorption induced by electrons or photons appeared respectively in 1918 [Dem18] and 1937 [Ter37], it was only around the mid 1960's that first studies using electronic excitations really emerged and opened a new side of surface science [Lid00]. This field grew quickly and a special attention was given to the Electron-Stimulated Desorption (ESD) where

[1] The desorption is "the process of removal of atoms, molecules, and radicals from the surface of a solid" [Age94].

adsorbed species are hit by low-energy electrons ($E \leq 500$ eV), resulting in the desorption of neutral and ionic fragments.

The ESD was used to develop, in 1974, the Electron-Stimulated Desorption Ion Angular Distribution (ESDIAD): adsorbed species on a mono-crystalline substrate form sharp ion beams under low-energy electron bombardment. This technique is used to gather information about the dynamical aspects of surface species as the beam direction is a function of the direction of the bond broken by the excitation.

In parallel to the ESDIAD development the Photon-Stimulated Desorption (PSD) field grew and in the early 1980's the acronym DIET (Desorption Induced by Electronic Transition), which includes ESD and PSD, appeared [Mad94]. DIET processes are of great interest for both surface science academic studies (e.g., surface photochemistry or dynamics of charge transfer) and surface science technology (e.g., partial pressure measurements or electron- and photon-beam lithography). It is worth noting that DIET processes may also be responsible of the exosphere composition of some planets, such as Mercury for example [MSG+11].

This chapter is dedicated to the description of the ESD process and focuses on the aspects related to the use of these phenomena to form a low-energy proton beam. Detailed information about ESD and more generally DIET can be found in reviews such as [TTTM83, RY91, Age94].

2.1. The MGR model

In 1964 two independent researches resulted in a major step towards a better comprehension of the ESD. On one side Redhead, working at Ottawa, was focusing on vacuum technology and studying the impact of electronically induced processes on both total and partial pressure measurements of ion gauges and mass spectrometers [Red64]. On the other side, in Chicago, Gomer and Menzel were looking at those effects from the point of view of the surface chemistry of surface interactions [MG64b, MG64a]. This led to one of the first and most famous ESD models, named after its authors: the Menzel-Gomer-Redhead (MGR) model [Men95].

Many ESD models exist, general or specific, and can be sorted into two categories: single-electron excitations and many-electron excitations. Single-electron excitations models, such as the MGR model detailed below, where the first proposed for ESD. Many-electrons excitations models, like the Knotek-Feibelman model [KF78, KF79], were developed later to explain a sufficient enough DIET in the case of strongly bound adsorbates.

2.1.1. General description

Desorption of adsorbed particles by direct kinetic energy transfer by a low-energy electron cannot be a dominant mechanism for ESD: the mass difference between the electron and the adsorbate limits the energy transfer. For instance an incident electron with an energy $E = 100$ eV can only transfer up to ~ 0.1 eV to an

hydrogen atom [Age94]. In such a scenario it could be enough to induce the desorption of physisorbed hydrogen but not for chemisorbed hydrogen or for heavier particles (physisorbed nor chemisorbed)[2]. The desorption induced by low-energy electrons is rather due to the electronic excitation of the adsorption bonding.

The MGR model uses adiabatic approximations and provides a one-dimensional semi-classical description of the ESD process. The adsorbate(A)-metal(M) system is first considered in its ground state, noted $(\mathrm{M}+\mathrm{A})$. Following an incident low-energy electron interaction, the system undergoes a Franck-Condon (FC) transition into an excited state. The semi-classical interpretation of the FC transitions assumes that nuclear motion can be neglected during the excitation time (10^{-15} s). The system state wavefunction can therefore be separated into a product of two terms, the electronic and the nuclear one. The resulting excited state can be:

- **Antibonding[3]:** $(\mathrm{M}+\mathrm{A})^{\mathrm{a}}$
- **Metastable:** $(\mathrm{M}+\mathrm{A})^{*}$
- **Ionic:** $(\mathrm{M}^{-}+\mathrm{A}^{+})$

A schematic representation of the ground state and the three possible excited states with respect to the distance above the surface z is shown in Figure 2.1a, with z_0 representing the center of the equilibrium position of the ground state configuration. The adiabatic approximation implies that the system is first electronically excited and then undergoes a nuclear motion over a time scale of $\sim 10^{-13}$ s. This motion converts potential energy into kinetic energy and, depending of the excited state, can lead to the adsorbate escaping (i.e., desorption). Curve crossing in Figure 2.1a implies Auger processes or tunneling with the electron sea of the substrate. As a result the $(\mathrm{M}+\mathrm{A})$ system excitation can lead to desorption of neutral (excited or not) or ionic adsorbate but also, through de-excitation and re-neutralization, to the same ground state.

2.1.2. Escape probability

The escape probability P_{e} can be expressed as [RY91]:

$$P_{\mathrm{e}} = \exp\left(-\int_{z_0}^{z_{\mathrm{c}}} R(z)\mathrm{d}z/v\right), \tag{2.1}$$

with z_{c} the critical position, $R(z)$ the recapture rate and v the velocity. $R(z)$ scales inversely to the characteristic lifetime of the excited or ionic state, $\tau(z)$.

The critical position z_{c} defines the position above which a transition leads to desorption. As illustrated in Figure 2.1b if a transition, a de-excitation from an

[2] Adsorption can be categorized as a function of the bond nature between the adsorbate and the substrate. Physisorption refers to weak van der Waals polarization forces whereas chemisorption implies a chemical bond (i.e., electronic exchange between the adsorbate and the substrate). The bond energy range in those two cases is around a few tenth of an eV and a few eV, respectively.

[3] An antibonding state, if occupied, weakens the bond between the two atoms it concerns.

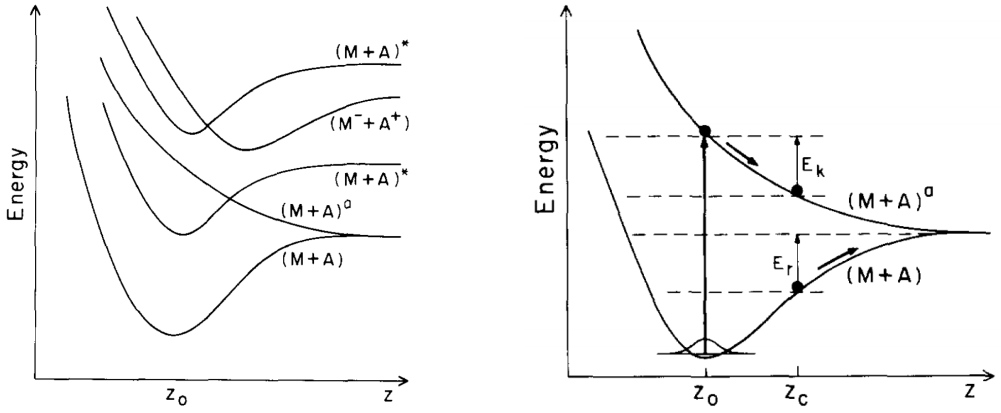

(a) (b)

Figure 2.1. (a): Potential-energy curves issued from the MGR model, with the different system states detailed in the text. Those potentials are affected by the work function of the surface. Because of the Franck-Condon principle, electronic excitations only affect the system state, and not its distance from the surface z. This is a simplified picture: in reality there are many possible excited states, which translate into many possible potential-energy curves. (b): Illustration of the critical position z_c. If the anti-bonding state de-excitation occurs before z_c the desorbing particle is recaptured into the ground state. Otherwise it escapes as a neutral desorbed particle. Both figures taken from [RY91].

anti-bounding state for example, occurs after z_c the particle has enough kinetic energy (E_k) to escape the recapture barrier (E_r), which leads to a desorption. On the other hand if $z < z_c$ when the transition occurs then the particle is recaptured. The critical position can be defined for all the other excited states of the system.

The desorption probability for an ion is related to the ratio of the ion escaping time to the ionic lifetime. The reneutralization of the ion before or after z_c leads respectively to the recapture into the ground state or to neutral desorption whereas ionic desorption is only possible if the ion is not reneutralized.

In the classical framework of the MGR model the kinetic energy E_k of a particle is given as:

$$E_k = Mv^2/2 = V(z_0) - V(z), \tag{2.2}$$

with M and v respectively the mass and speed of the particle and $V(z)$ the value of the excited-state potential evaluated at the position z. Equation (2.1) can be written as:

$$P_e = \exp\left(-\sqrt{\frac{M}{2}}\int_{z_0}^{z_c} R(z)\mathrm{d}z/\sqrt{V(z_0)-V(z)}\right). \tag{2.3}$$

As expected from Equation (2.3) there is an isotope effect affecting the desorption probability which was observed experimentally [HM82, MYKU70, Mad73].

2.1.3. Limits of the model

The MGR model exhibits two major limits:

- **No explanation of the nature of the repulsive potential for positive ions:** The radius of positive ions is much smaller than the one of their corresponding atom but in the MGR model the ionic state potential curve is shifted to higher z values compared to neutral states, as shown in Figure 2.1a. This shift is opposed to what is expected from a smaller particle but required in the MGR model to allow ionic desorption.
- **Requirement for a long-lived antibonding state:** The typical lifetime of such an excited state on a metal surface is of the order of 10^{-16} s [CGFE79] whereas it takes around two orders of magnitude longer for a typical ion to escape the surface. The long-lived antibonding state required in the MGR model for ionic or neutral desorption is not realistic.

Those issues were treated by bringing some modifications to the MGR model, as in the case of the Antoniewicz model developed in 1980 [Ant80]. The Antoniewicz model also considers the negative ionic ESD experimentally observed [HL78, Yu79]. However as the MGR model describes well the ESD system used in this work and described in the following section (hydrogen on tungsten (110)) [SW77], no other models will be introduced here.

2.2. Hydrogen on tungsten (110)

2.2.1. Tungsten (110)

Tungsten can offer, under adequate treatment a clean and well defined surface making this metal a very popular choice for surface studies. The cleaning and annealing[4] procedure, described in Section 7.1.2, requires the tungsten crystal to be heated to temperatures up to 1900 °C.

Hydrogen adsorbate on a tungsten (110) crystal (H/W(110)) bombarded by low-energy electrons can emit protons using the same crystal and under comparable conditions as for low-energy positrons, as described in Chapters 3 and 6.

Tungsten is a metal which has a body-centered cubic Bravais lattice[5] which is illustrated in Figure 2.2a. Plane (110)[6] is also shown in the latter figure and a 2D view of the tungsten (110) surface is detailed in Figure 2.2b.

[4] Annealing involves heating a metal above its recrystallization temperature (between 1300 °C to 1900 °C for tungsten [ZYY+14]) in order to removes the crystal defects.

[5] Bravais lattice uses characteristic symmetries to organize crystals into seven families (cubic, tetragonal, orthorhombic, hexagonal, monoclinic, trigonal and triclinic) and four lattice centering types (primitive, base-centered, face-centered and body-centered). Due to some redundancy in the combination of crystal families and lattice centering types (e.g., a base-centered cubic crystal is similar to a primitive tetragonal, with the latter offering a simpler description of the crystal), there is a total of only 14 Bravais lattices.

[6] Miller indices are used to define directions and planes in a crystal using a vector of the Bravais lattice. In a cubic lattice, because of the system symmetries, plane (110) is equivalent to planes (101) and (011).

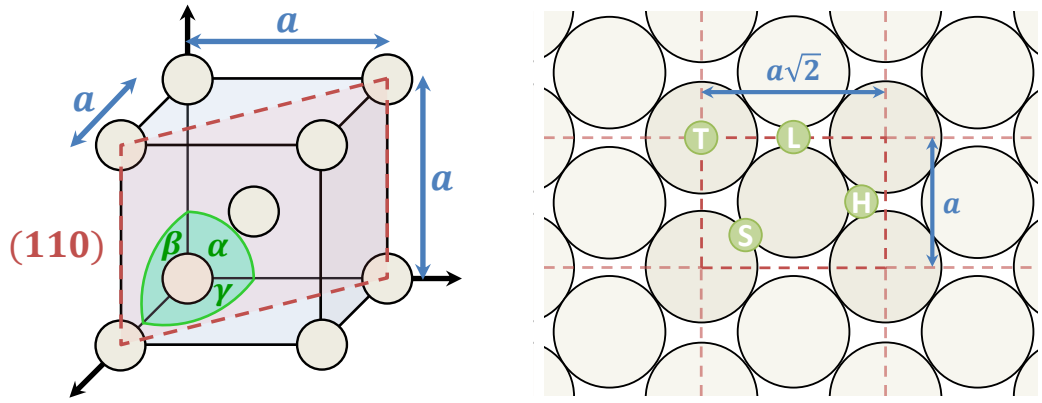

(a) (b)

Figure 2.2. (a): Body-Centered Cubic (BCC) crystal structure defined by a unit cell of length $a = b = c$ and with $\alpha = \beta = \gamma = 90°$. A unit cell is composed of eight atoms at each corner of the cube (each shared by in total eight unit cells) and one atom in its center, resulting in $N = 8 \times \frac{1}{8} + 1 = 2$ atoms per unit cell. For a better visibility the atoms of the lattice are shown smaller than they are: atoms should touch each other along the cube large diagonal. (b): Tungsten (110) surface scheme. Possible adsorption site examples are represented for hydrogen atoms: top (T), long bridge (L), short bridge (S) and threefold hollow (H). In this scheme tungsten and hydrogen atoms are represented at scale. Only one adsorbate can be adsorbed per tungsten surface atom.

As shown in Figure 2.2b the tungsten (110) atom surface density can be expressed as:

$$\rho_{W_{110}} = \frac{2\text{atoms}}{a^2\sqrt{2}}, \tag{2.4}$$

with $a = 3.1652$ Å [Her11] the lattice constant of tungsten, resulting in a surface density of $\rho_{W_{110}} = 1.4 \times 10^{15}\text{atoms/cm}^2$.

2.2.2. Adsorption process

The different possible adsorption sites on tungsten (110) are shown in Figure 2.2b. In the case of the H-W(110) system the molecule approaches preferentially the surface near top sites and hydrogen atoms are preferentially adsorbed onto threefold hollow sites [BM08]. H_2 binding energy is $\Delta E_{\text{H2(g)}} = -4.57$ eV whereas the binding energy of a single hydrogen atom onto a tungsten (110) substrate is $\Delta E_{\text{Hbind}} - 3.15$ eV [FKNM12]: H_2 dissociative chemisorption on tungsten (110) is an exothermic process (i.e., energetically favorable). The estimated hydrogen desorption energy $E_{\text{H}_{\text{desorb.}}}$ can be calculated as:

$$E_{\text{H}_{\text{desorb.}}} = -2\Delta E_{\text{Hbind}} + \Delta E_{\text{H2(g)}}. \tag{2.5}$$

As a result when a H_2 gas molecule gets close to the tungsten (110) surface there is a high probability that it undergoes dissociative chemisorption [CB96]: the molecule interacts with a surface site and dissociates with the two atoms being adsorbed.

The adsorption of hydrogen on such sites can lead to H^+ desorption. During desorption, as the hydrogen coverage diminishes so does the proton ESD yield. The desorbed proton initial yield is used as a metric to estimate the efficiency of the process. The proton yield, under similar electron bombardment, increases strongly if the adsorption is performed at a temperature lower than about 160 K, as shown in Figure 2.3a. The proton yielding sites populated only at low temperature can be presumably attributed to step edges imperfection of the tungsten surface [ZWG93].

Furthermore the adsorption coverage θ also impacts, non-linearly, the proton yield from ESD of H/W(110), as shown in Figure 2.3b. The surface adsorption coverage θ is defined as the ratio between the number of adsorption sites occupied to the number of adsorption sites available (i.e., one hydrogen atom per surface tungsten atom). As one site can only be filled with one adsorbate, this means that at saturation coverage $\theta = 1$ the surface hydrogen density is the same as for tungsten.

From Figures 2.3a and 2.3b one can see that hydrogen adsorption should be performed on a clean and cold tungsten (110) surface until saturation is reached to maximize the proton emission under ESD.

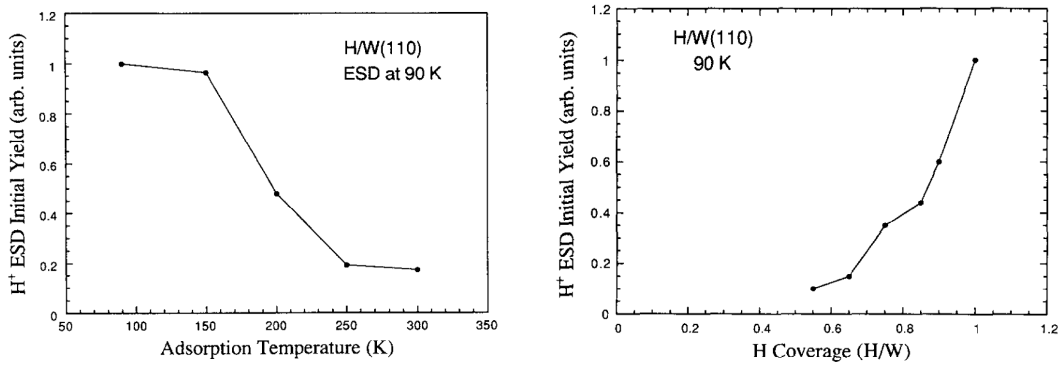

(a) (b)

Figure 2.3. (a): Adsorption temperature dependency of the proton ESD signal. Performing the hydrogen adsorption at a temperature $T \leq 160$ K improves significantly the initial proton ESD yield. (b): Impact of the hydrogen coverage of the tungsten (110) crystal on the proton ESD yield. Initial proton desorption rate is maximal at saturation (hydrogen coverage $\theta = 1$) and strongly decreases for lower values of θ. Both plots are taken from [ZWG93].

2.2.3. Proton desorption

Upon hydrogen adsorption, bombarding the tungsten crystal with low-energy electrons can lead to proton desorption. This yield depends on to the adsorption temperature and on θ, as stated above, but also on the electron flux hitting the surface. Furthermore a threshold effect exists: the minimum energy required for desorption to occur depends on the system and the desorbed state (neutral or ionic).

In the case of tungsten (110) a threshold energy for incident electrons of approximately 15 eV is required to induce proton desorption and an electron energy of more than around 40 eV allows for a maximum proton desorption efficiency (i.e., the number of desorbed proton per incident electron), as shown in Figure 2.4.

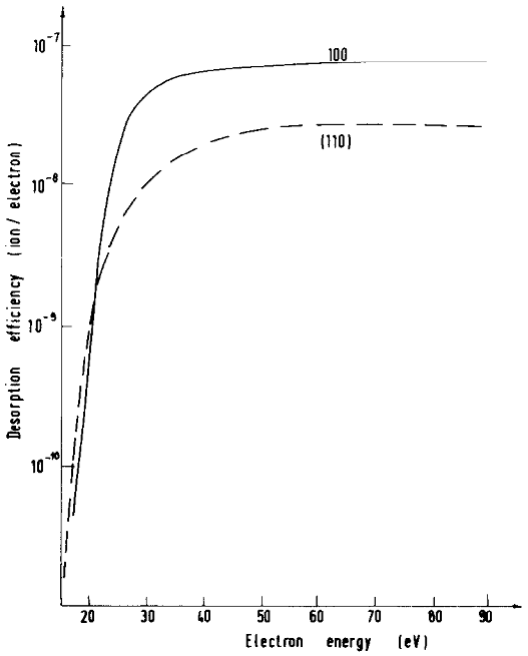

Figure 2.4. Threshold in the proton ESD for hydrogen adsorbed on tungsten (100) and tungsten (110). Proton desorption becomes possible around 15 eV and the desorption efficiency reaches a plateau above an electron incident energy of approximately 40 eV. Figure taken from [SW77].

2.3. Expected output properties

Under a constant electron flux the proton desorption rate of the H-W(110) system follows an exponential decay as shown in Figure 2.5. The proton desorption rate can be expressed as [ZWG93]:

$$H^+(t) = H^+(0)\exp^{(-i_e\sigma_t t)}, \tag{2.6}$$

with $H^+(t)$ the proton desorption rate at a defined time t in protons/sec, $H^+(0)$ the initial yield, i_e the electron current density in $e\text{cm}^{-2}\text{s}^{-1}$ and $\sigma_t \sim 5\times10^{-18}$ cm^2 the proton desorption cross-section. Assuming a saturation coverage of hydrogen on tungsten (110), the number of desorbed protons per incident low-energy electron is $i_p/i_e = 0.8 \times 10^{-7}$ [ZWG93]. As a result an electron current density of 80 nA/cm^2 is enough to initially produce around 10^4 protons/sec from a 0.25 cm^2 surface. Using Equation (2.6) with this electron current density leads to a desorbed proton rate of 77% of the initial yield after one day of continuous desorption, which can easily be compensated by adjusting the low-energy electron bombardment flux.

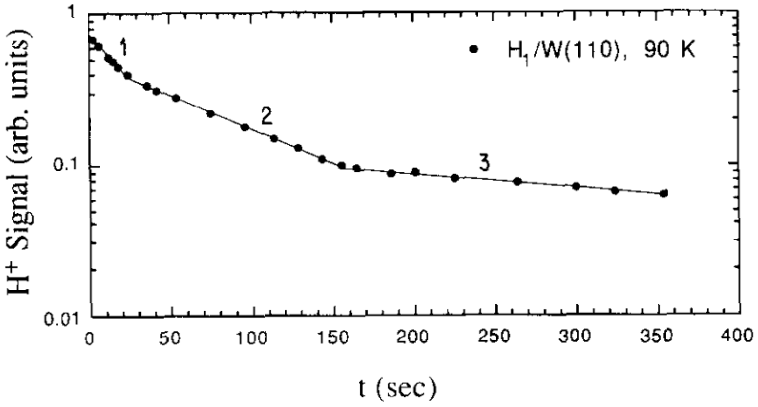

Figure 2.5. Proton desorption rate for hydrogen adsorbed at 90 K on tungsten (110). The three parts of the plot were individually fitted using Equation (2.6). Plot taken from [ZWG93].

Ions issued from ESD exhibit an energy of a few eV and an energy spread which is related to the adsorbate-substrate bond characteristics. In the case of proton ESD of H-W(110), the energy spread is of the order of a few eV, as shown in Figure 2.6a. The angular spread of desorbed ions from monoatomic adsorbate is well defined (around 20° FWHM) and exhibit a Gaussian profile, centered on the normal of the surface, as shown in Figure 2.6b. This distribution is sligthly affected by the system temperature, with narrower angular spread at lower temperature.

Even though neutral desorption is the dominant output of ESD (ionic desorption represents around one percent of the total desorption), the low cross-section of the process (and therefore desorption intensity) leads to a negligible or null UHV deterioration [ZWG93]. Assuming the goal intensity of the CALIPSO source of around 10^4 protons/sec and the typical experimental conditions of the *a*SPECTino spectrometer, the neutral desorption of the H-W(110) system should not impact significantly the vacuum quality of *a*SPECTino or similar apparatus, as detailed in Section 6.1.3.1.

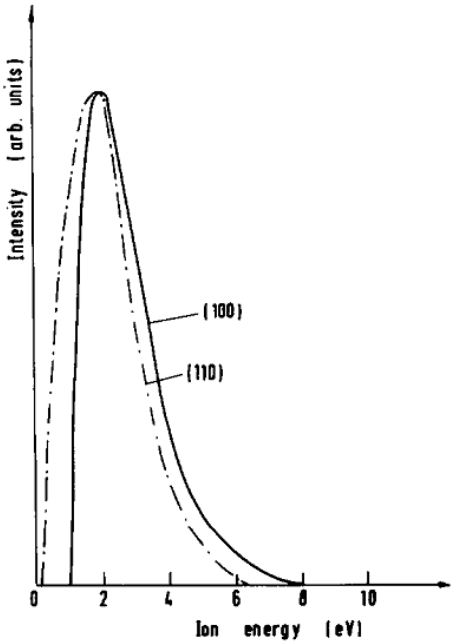

(a)

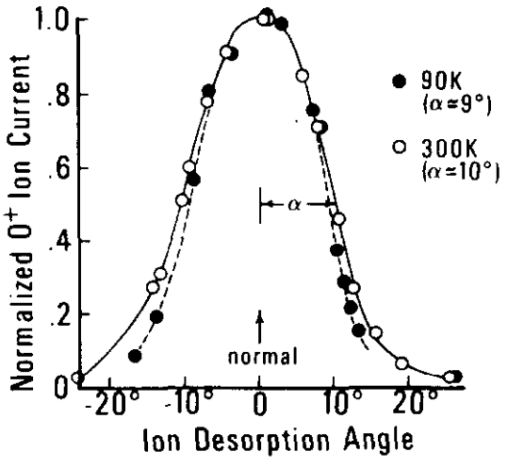

(b)

Figure 2.6. (a): Energy spread of protons desorbed from tungsten (100) and tungsten (110) crystal surfaces. In both cases the FWHM is around 3 eV. Plot taken from [SW77]. (b): Temperature dependent angular spread for Oxygen ions desorbed from tungsten (110). Figure taken from [Mad80].

Conclusion

The Electron-Stimulated Desorption process, and specifically the system hydrogen onto W(110), have been introduced. As shown in this chapter such a system can be used to build a low-energy and low-intensity proton source with little to none vacuum degradation in the UHV range. Furthermore the required treatments of the tungsten crystal are similar to the case of a low-energy positron source, as detailed in Chapter 3.

Chapter 3

Positrons in matter

> It is hard to describe the exact route to scientific achievement, but a good scientist doesn't get lost as he travels it.
>
> *(Isaac Asimov)*

Contents

3.1. Properties and creation of positrons 22
3.2. Positron interactions in a metal 23
3.2.1. Positron backscattering and diffraction 23
3.2.2. Thermalization and diffusion 25
3.3. Re-emission of moderated positrons 27
3.3.1. Work function 28
3.3.2. Re-emission efficiency 29
3.3.3. Typical output properties 31

In 1928 Paul Dirac[1] manages to combine special relativity and quantum mechanics in a context where matter is supposedly only made of electrons and protons [Dir28]. The resulting Dirac equation, developed to describe the behavior of relativistic electrons bound to a nuclei, had much deeper implications than Dirac first imagined. One of those is the theoretical prediction of antimatter: after refraining himself for some time [Dir78], Dirac affirms in 1931 that a new and undiscovered particle with the same mass but the opposite charge as an electron should exist [Dir31]. A year later Carl Anderson proves the existence of this anti-particle, named positron, by looking at high-energy cosmic rays hitting a lead plate with a cloud chamber [And33], granting him the Nobel Prize in Physics in 1936. Other anti-particles, also predicted by the Dirac equation, were discovered afterward: the anti-proton in 1955 [CSWY55] and the anti-neutron

[1] The British theoretical physicist Paul Adrien Maurice Dirac was born on 8th August 1902 and died on 20th October 1984. In 1933 he shared a Nobel Prize in Physics with Erwin Schrödinger "for the discovery of new productive forms of atomic theory".

in 1956 [CLPW56], both at the Bevatron accelerator at the Lawrence Berkeley National Laboratory, USA.

Due to their anti-matter nature and positive charge, positrons are very sensitive to defects in matter and can interact in many ways with the surface of a solid, making them a great tool for surface science. However it was only until the 1970's, where intense mono-energetic positron beams could be created, that using positrons to probe condensed matter really became popular. Through the years techniques progressed a lot and low-energy positron beams became more intense. The positron part of the CALIPSO source is based on the same concepts that are used for the creation of such beams.

This chapter will introduce the relevant positron physics and then focus on the process used to create a mono-chromatic beam of low-energy positrons.

3.1. Properties and creation of positrons

The CPT theorem[2] implies that the mass, lifetime, gyromagnetic ratio and charge amplitude of the positron are the same as for the electron, with the sign of the charge being opposite [CH05]. The positron is therefore a lepton whose properties are shown in Table 3.1.

Table 3.1. Fundamental properties of positrons [P+16].

e^+ property	Value
Rest mass m_{e+}	0.510 998 9461(31) MeV/c^2
$(m_{e+} - m_{e-})/m_{average}$	$< 8 \times 10^{-9}$
Charge q_{e+}	1.602 176 6208(98)$\times 10^{-19}$ C
$\lvert q_{e+} + q_{e-} \rvert / e$	$< 4 \times 10^{-8}$
Spin	1/2 $\hbar$
Mean life (in vacuum)	$\tau > 6.6 \times 10^{28}$ yr (CL = 90%)

Positrons can be created through:

- **Pair production:** given an energy above the process threshold of $2m_e \approx 1.022$ MeV and in the presence of an electric field (e.g., proximity with a nucleus), a photon can be converted into an electron-positron pair: $\gamma \rightarrow e^- e^+$. The nucleus proximity is required in order to conserve energy and momentum, meaning a single high-energy photon cannot create an electron-positron pair in vacuum, but two high-energy photons can. This process is used for example at the Lawrence Livermore National Laboratory to create a relativistic positron beam using high-intensity lasers hitting a Tantalum target [Ca16].

[2] This theorem states that laws of nature are invariant under the conjoined effects of charge conjugation (C), parity (P) and time reversal (T). In contrast to the individual near-symmetries C, P and T, no violation of CPT has been found.

- **Beta decay:** weak force can also create positrons through radioactive β^+ decay where a proton is converted into a neutron, a positron and an electron-neutrino, such as: $^{22}\mathrm{Na} \longrightarrow {}^{21}\mathrm{Ne} + \mathrm{e}^+ + \nu_\mathrm{e}$. Common β^+ radioactive isotopes as well as their properties are listed in Table 3.2.

Table 3.2. List of typical e^+ radioactive sources [Bas15, NGS10, Sin07]. The maximum energy corresponds to the end of the spectrum of the main positron emitting branch and not the overall maximum possible energy.

Isotope	$\beta+$ Branching ratio (%)	Half-life	Maximum energy (keV)
^{22}Na	90.3	2.6 yr	546
^{58}Co	14.9	70.9 d	475
^{64}Cu	17.6	12.7 h	653

Cosmic rays contain a small fraction of positrons that are created from different processes, either directly at astrophysical sources (such as supernova remnants) or indirectly by interactions of cosmic rays with interstellar gas. It is interesting to note that in 2013 the AMS experiment measured a higher than expected positron rate in the high-energy range (above 10 GeV) of cosmic rays, which can possibly be attributed to the existence of dark matter [A+13].

3.2. Positron interactions in a metal

Positron interactions in a solid differ from those of electrons in many ways. It is mainly due to the charge difference but also because a positron is the only one of its kind in a solid: contrary to electrons, there is no positron sea to interact with. Figure 3.1 summarizes the typical interactions and time scales when a positron beam hits a solid. The following sections will only introduce the positron physics relevant to this work, which concerns a positron beam ($E \leq 0.5$ MeV) hitting a metal. A more complete description can be found in [SL88], [PN94] or [CH05].

3.2.1. Positron backscattering and diffraction

A part of a positron beam hitting a surface is reflected. This backscattering depends, for a semi-infinite solid, on the incident positron energy and the solid atomic number Z, as shown in Figure 3.2. Backscattering values of up to 40% can be achieved for high-Z materials and positrons with 15 keV$\leq E \leq 1$ MeV.

Similarly to electrons, positrons can diffract from the atoms of the material. Since positrons and electrons have the same mass their diffraction beam angle, for similar incident beam characteristics, are the same but because of the charge difference the intensities of the diffraction pattern differ. This is a consequence of the absence of other positrons in the solid to interact with and the repulsive Coulomb interaction between positron and nuclei.

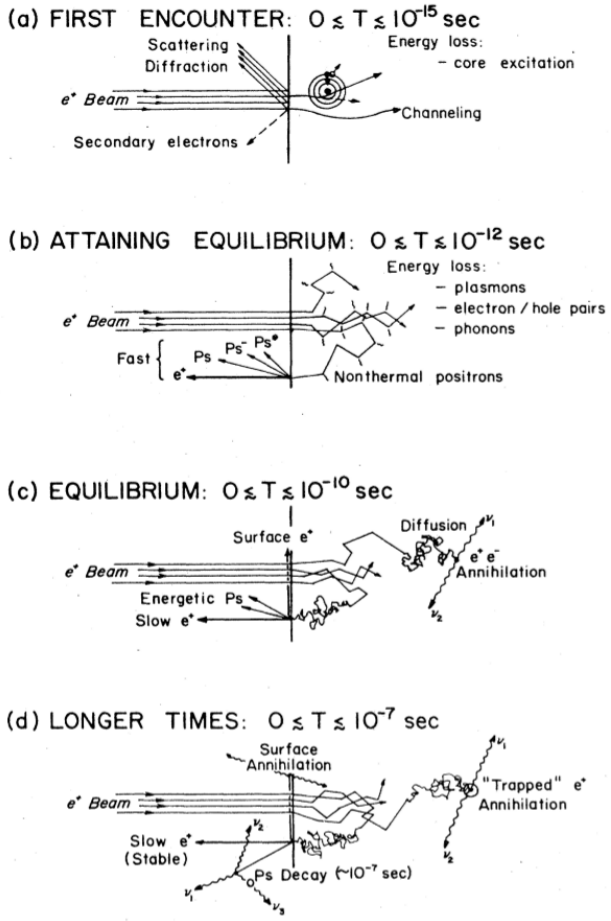

Figure 3.1. Positron beam ($E \leq 100$ keV) interactions with a solid, organized in four time frames. The following sections detail these processes. Scheme taken from [SL88].

Even though positrons do annihilate with electrons, the annihilation cross section is five to six orders of magnitude smaller than that of scattering [JR76]. The time scale for positron scattering or diffraction is around 10^{-15} s.

Several methods are using diffraction of either electrons or positrons to probe the surface of samples. For instance Low-Energy Electron Diffraction (LEED) uses a beam of low-energy electrons (around 10 to 600 eV) to determine the surface structure of mono-crystals. This technique, born in 1927, saw its positron counterpart, Low-Energy Positron Diffraction (LEPD), emerging in 1979 when more intense low-energy positron beams became available. Those two techniques are very complementary and the improvements on positron beam brightness (see Section 3.3.3) over the last decades made it a powerful tool for surface studies [CDM90].

Similarly Reflection High-Energy Electron Diffraction (RHEED), which is based on high-energy electrons (between 10 and 20 keV) small angle diffraction, is now

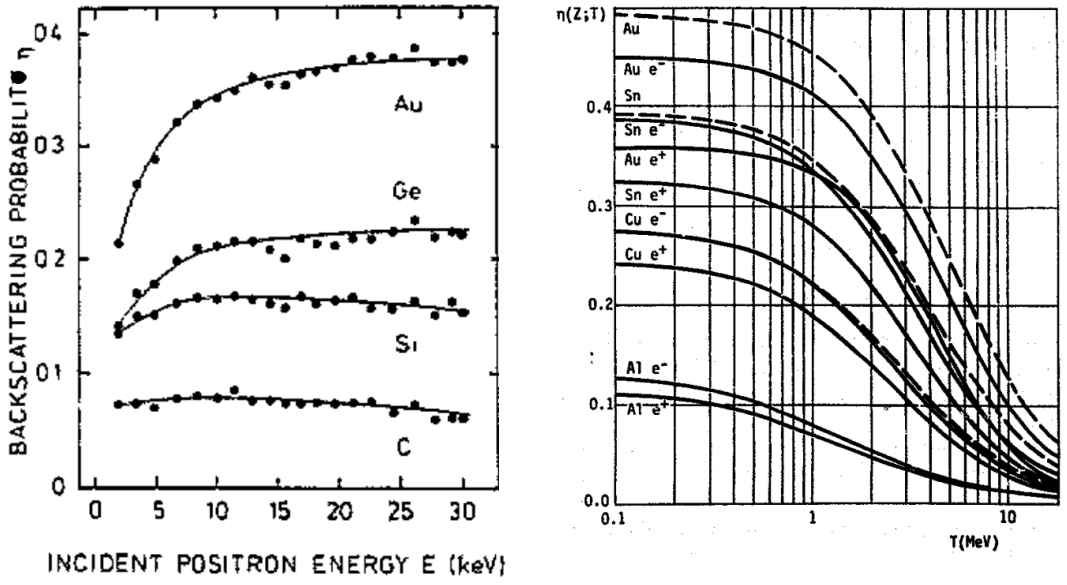

(a) (b)

Figure 3.2. Fits of the measured backscattering probability as a function of positron energy for several atomic numbers Z in the low-energy range (a) and above (b). Plot (b) also shows the fits of the measured backscattering probabilities for electrons as well as the model described in [KTV74]. Plots taken from [MPMH92, KTV74].

joined by Reflection High-Energy Positron Diffraction (RHEPD) [FMM+13].

3.2.2. Thermalization and diffusion

Very energetic positrons, in the range of MeV, mainly lose energy in a solid through Bremsstrahlung. This process is less efficient for positrons than it is for electrons because of their opposite response to the screened positive nuclear charge. At intermediate energies ($E \leq 100$ keV) inelastic scattering by excitation of core and valence electrons dominates, down to positron energies of a few tens of eV where plasmon excitations and subsequently electron-hole excitations are prevailing in metals. Approaching thermal energies (a few tenths of an eV) positrons thermalize through phonon scattering [PC70]. The timescale of this process, a few ps, is much smaller than the typical positron lifetime in a solid, which is around 10^{-10} s.

The implantation distribution represents the depth at which positrons are stopped (i.e., thermalized) in the solid. The so called Makhovian profile can be expressed as [Mak60]:

$$P(z) = \frac{m z^{m-1}}{z_0^m} \exp\left(-\left(\frac{z}{z_0}\right)^m\right), \tag{3.1}$$

with z the implantation depth and m a dimensionless parameter that depends on

the material called the *shape* parameter[3]. z_0 is defined as:

$$z_0 = \frac{A}{\rho \cdot \Gamma\left(1 + 1/m\right)} E^n, \tag{3.2}$$

with A and n material dependent parameters, ρ the density of the implanted material in g/cm^3, Γ the gamma function and E the positron initial energy in keV. In the case of positron implantation, typical values for those parameters are $m \approx 1.9$, $A \sim 400\rho$Å/keV^n and $n \approx 1.6$ [SL88]. Examples of calculated Makhovian profiles for positron implantation in tungsten are shown in Figure 3.3: with increasing energy the implantation distribution becomes broader and the mean implantation depth is further away from the surface.

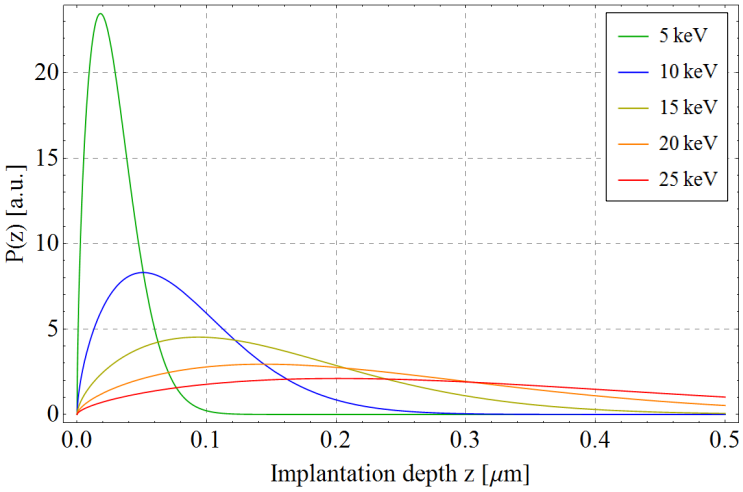

Figure 3.3. Calculated Makhovian profiles in tungsten for positrons with an energy ranging from 5 keV to 25 keV using Equations (D.2) and D.3. Parameter values $\rho = 19.3$ g/cm^3, $m = 1.621$, $n = 1.498$ and $A = 5.06$ μg cm^{-2} keV^{-n} are taken from [DH08].

Once thermalized, positrons diffuse through the metal by quasi-elastic phonon scattering. The diffusion length L_+ can be defined as:

$$L_+ = \sqrt{\frac{D_+}{\lambda_b + \kappa}}, \tag{3.3}$$

with D_+ the positron diffusion coefficient usually given in cm^2·s^{-1} and κ the defect trapping rate in s^{-1}. The annihilation rate in the defect-free lattice λ_b is defined as:

$$\lambda_b = \frac{1}{\tau_b}, \tag{3.4}$$

with τ_b the bulk lifetime in s. In defect-free metals the typical diffusion constant D_+ is of the order of 1 cm^2·s^{-1} at 300 K and the diffusion length L_+ is around 1000 Å [SL88].

[3]Depending on the value of m the profile can be an exponential ($m = 1$) or a Gaussian ($m = 2$) derivative.

Because of their positive charge low-energy positrons are very likely to be trapped in the lower potential region induced by a defect (an ion core missing in the lattice), inevitably leading to an annihilation with an electron. A defect density which is too high therefore reduces drastically the probability for a positron to diffuse to the solid surface. A positron can stay trapped for $\sim 3 \times 10^{-10}$ s and annihilates as soon as an electron is close enough: the annihilation process itself is very fast (around 10^{-21} s [Sch85]). There are many possible mechanisms for positron-electron annihilation, from the radiationless process emitting an electron to a one, two, three or even more gamma-rays emission process [CH05]. However the 2-γ emission, shown in Figure 3.4, is the most probable, the other processes being highly suppressed.

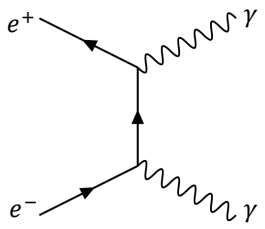

Figure 3.4. Feynman diagram of the lowest order contribution to positron-electron annihilation into two photons.

A positron which reaches the metal surface can bind with an electron to form a positronium (noted Ps). Positronium is a hydrogen-like state composed of one electron and one positron with roughly halved energy levels of those of the hydrogen atom. The singlet state, which corresponds to anti-parallel spins $S = 0$, is called para-positronium (p-Ps) whereas the triplet state ($S = 1$) is called ortho-positronium (o-Ps). p-Ps predominantly decays into two photons with a lifetime $\tau_{\mathrm{p-Ps}} = 125$ ps [CMY99]. o-Ps has a lifetime in vacuum $\tau_{\mathrm{o-Ps}} = 142.05$ ns and predominantly decays into three photons [B$^+$07]. However o-Ps undergo a pick-off process in matter where the o-Ps electron is replaced with an electron of opposite spin, converting the o-Ps into a p-Ps and lowering the o-Ps effective lifetime in matter down to 125 ps $\leq \tau_{\mathrm{o-Ps_{eff}}} \leq 142$ ns. The Ps annihilation spectra, shown in Figure 3.5, is highly dominated by 2-γ decay due to the pick-off process and the strong 3-γ decay suppression [OP49].

3.3. Re-emission of moderated positrons

Under certain circumstances positrons can be re-emitted from a material, called moderator, with a low and well-defined energy and a small angular spread. This process is specific to positrons and allows to create mono-chromatic, bright and low-energy positron beams: the positron part of CALIPSO is designed around it.

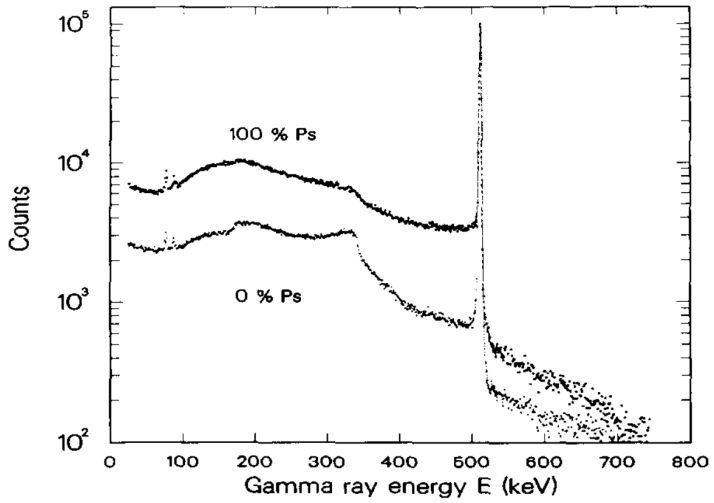

Figure 3.5. Annihilation spectra measured with a Ge detector for 0% and 100% Ps atom fraction. By varying the energy of a moderated positron beam hitting a surface, one can vary the fraction of positrons that escape the surface as PS atom. In this case the incident energies were 15 keV (0% Ps) and 40 eV (100% Ps). Plot taken from [L+86].

3.3.1. Work function

In order to explain this process the work function of a material will be introduced first. The work function is the minimum energy required to extract a particle from the bulk of a material into the vacuum (more than 10 nm from the surface) [Kit04]. This surface property is defined as:

$$\phi_{\mp} = \pm D - \mu_{\mp}, \tag{3.5}$$

with $\phi_{\mp}$ the electron or positron work function, D the dipole surface barrier value and $\mu_{\mp}$ the electron or positron chemical potential. It is very common to find in literature the term *work function* alone, without any indication about the concerned particle. In such cases it is usually referring to the electron work function whereas in this work it shall refer to the positron work function. Figure 3.6 shows the potentials for electrons and positrons near the solid-vacuum interface and the resulting work function. If D is high enough it may result in a negative positron work function: if a low-energy positron diffuses close to the solid-vacuum interface, it will be re-emitted from the solid into the vacuum.

A direct consequence of the definition of the work function is its dependency on the surface properties. The nuclei density at the solid-vacuum interface, which is related to the crystallographic orientation of the solid, is included in the D term. The dipole surface barrier value is also shifted by the surface contamination: nature and density of the adsorbate will impact the work function. The temperature of the solid mainly affects the crystal density and thermal vibrations of the atoms, resulting in a complex dependency of the work function [Kie86, IK01], as already shown in Figure 1.4.

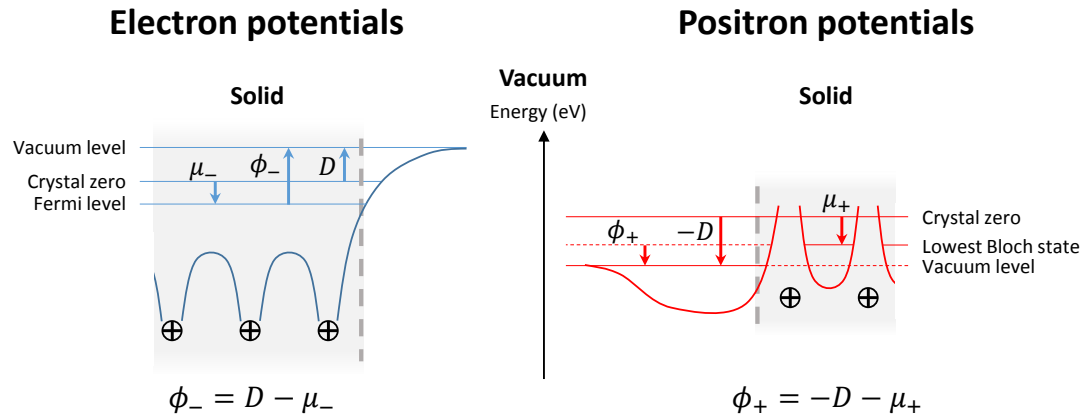

Figure 3.6. Work function of a metallic surface for e^+ and e^-. The electrochemical potential (or Fermi level) μ arises from the solid's nuclei and electron density whereas the dipole surface barrier D is the result of the electron sea overflowing into the vacuum. This barrier tends to attract electrons into the solid (therefore increasing the e^- work function) and, because of their positive charge, to repulse positrons from the solid (decreasing the e^+ work function). Respective levels are not to scale and neither is the global position of the electron potentials compared to the positron ones. This figure was inspired from [oM17].

Values of electron and positron work function for typical positron moderators are listed in Table 3.3. Assuming a clean, polished and well defined mono-crystal as the moderator, the positron work function is homogeneous and the resulting electric field is normal to the surface of the moderator. As the work function value is much higher than the typical kinetic energy of a thermalized positron in a solid at 300 K or less, which is about 25 meV, the angular distribution of re-emitted positrons is narrow, as shown in Section 3.3.3.

3.3.2. Re-emission efficiency

As seen in Section 3.2 positrons have a high chance of leaving a solid without being thermalized or being trapped in a defect and annihilated. In order to quantify the probability of a positron to be re-emitted as a moderated positron by the work function, we define the efficiency as:

$$\epsilon = \frac{N_{\text{reem}}}{N_{\text{inc}}} \tag{3.6}$$

with N_{reem} the number of re-emitted moderated positrons and N_{inc} the number of incident positrons hitting the moderator. The efficiency is sometimes defined by using the number of positrons emitted by the primary source for N_{inc}: in this work only the former definition is used. A direct consequence of this rather general definition is the high number of efficiency dependencies, such as on:

- **The e^+ primary source:** the nature of the positron source affects di-

Table 3.3. Values of electron and positron work function for different materials and crystallographic orientations [HSS02, P+08, Hay09]. Values are for work functions at room temperature (300 K).

Element	Orientation	ϕ_- (eV)	ϕ_+ (eV)
Pt	Polycrystalline	5.64	-2.2 (2)
Ta	Polycrystalline	4.25	-1.6 (6)
W	(100), not treated	4.63	-2.5 (2)
W	(100), annealed		-3.00 (15)
W	(110)	5.22	2.9

rectly the efficiency: using the pair production process to create the primary positrons often leads to a smaller efficiency than with a radioactive isotope due to the higher energy of primary positrons [GH06]. Furthermore, using an already moderated positron beam accelerated to a few keV leads to a very high efficiency of about 20% [FGL85].

- **The geometry:** figure 3.7 shows a non-exhaustive overview of different source and moderator geometries. Depending on the requirements of the setup different geometries can be favored to maximize the efficiency.

- **The moderator material and quality:** as seen in Section 3.2.2 the positron diffusion length L_+ is specific to the sample. A higher value implies a higher chance for a moderated positron to diffuse to the surface and to be re-emitted. Both the surface cleanness and the defect density of a moderator impact the efficiency: the smaller the defect density and the cleaner the surface, the higher the efficiency. Moreover the moderator surface contamination with adsorbates leads to a shift in the work function (in both the local amplitude and direction of the resulting electric field) which depends on the contamination coverage. Both problems are efficiently treated through moderator annealing and adapted cleaning procedures which require heating the crystal to high-temperatures (see Section 7.1.2). Table 3.4 shows a list of typical positron moderators with their diffusion length and efficiency.

Even though they do not have a negative positron work function, rare gas solids are also used to create low-energy positron beams (e.g., [GVW14]). Contrary to metals those solids do not have free electrons close to their surface, resulting in a much smaller surface barrier potential. However they have a particularly high positron diffusion length (see Table 3.4) which results in a high probability for an epithermal positron to diffuse close to the surface and overcome the positive positron work function [GM86]. Rare gas solids can achieve an efficiency of the level at the% but with a broad energy distribution of about 1 eV FWHM [MPSY08].

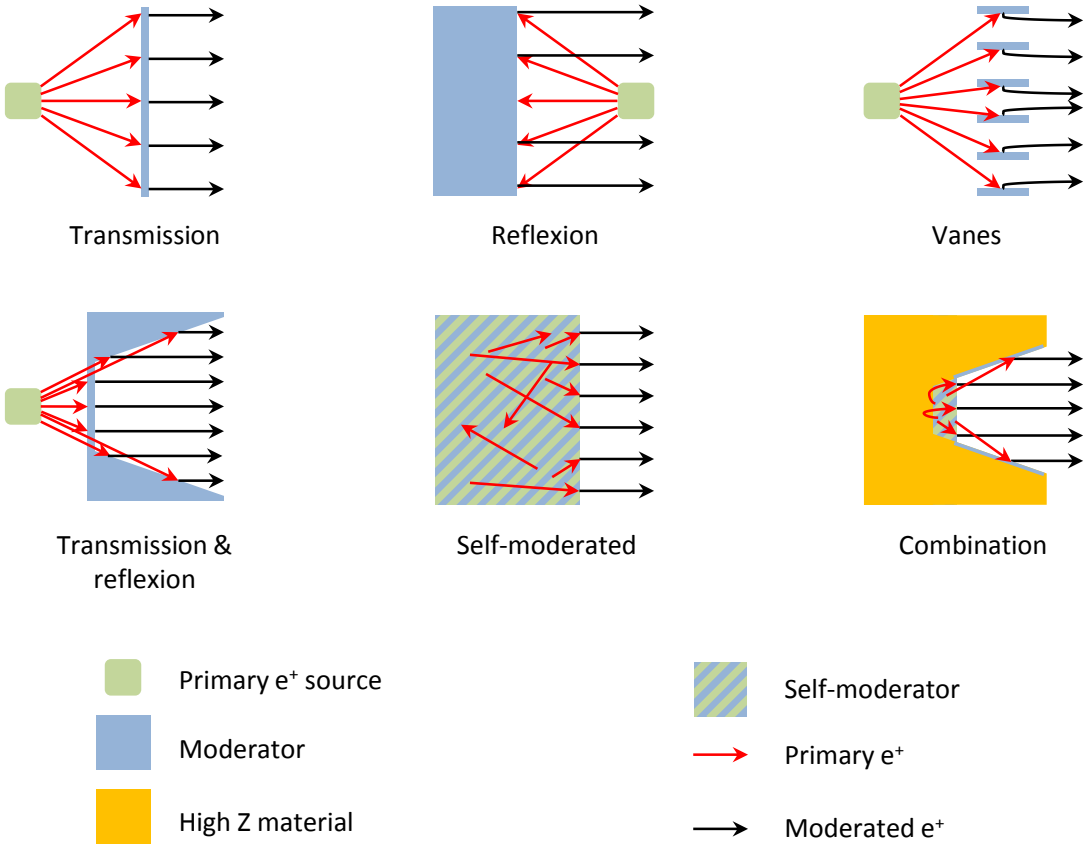

Figure 3.7. Examples of positron source and moderator geometries. Typical setups are: transmission using a thin moderator foil (few μm), reflexion usually coupled with a point-like source or self-moderated sources, like ^{64}Cu, for materials that can be both the positron source and moderator. Many other geometries are possible, such as using a high-Z material to increase positron back-scattering onto the moderator. Scheme inspired from [SL88].

3.3.3. Typical output properties

In the case of clean metallic single-crystal moderators the energy spread of re-emitted moderated positrons for a sample temperature $T_{\text{samp}} = 300$ K is around 75 meV FWHM [FLG86]. This value is the consequence of thermal broadening only of the re-emitted positrons: cooling down the moderator strongly reduces the beam energy spread as seen in Figure 3.8a. Positrons which are not completely thermalized and do escape the moderator contribute to the broadening of the re-emitted positron energy peak. The effect of epithermal positron tailing is more important at a low moderator temperature as the thermalization process lasts longer and more epithermal positrons can escape [FLG86]. An effective temperature T_{eff}, ranging from 1 to around $4\times T_{\text{samp}}$, is usually used to compensate for this effect when fitting the re-emitted positron energy spread [GMCB85].

In addition the narrow angular distribution of re-emitted positrons can be

Table 3.4. Typical efficiency of usual positron moderators [WCW+07, VLSE83, KCS+90, HA87, KRBT+05]. The diffusion length is given for defect-free materials. The efficiency is dependent on many parameters and values listed in this table may vary depending on experimental conditions.

Moderator	Diffusion length [Å]	Typical efficiency
Ni polycrystalline	/	$\sim 2 \times 10^{-4}$
Ni (100)	1165	$\sim 7 \times 10^{-4}$
W polycrystalline	/	$\sim 2 \times 10^{-4}$
W (110)	1350	$\sim 3.2 \times 10^{-3}$
Ne	~ 10000	$\sim 2 \times 10^{-2}$

estimated as follows:

$$\theta_{1/2} = \sqrt{\frac{k_B T_{\text{eff}}}{\phi_+}}, \tag{3.7}$$

with $\theta_{1/2}$ the most probable half-angle of the re-emitted positron beam angular distribution, $k_B = 8.6173324 \times 10^{-5}$ eV/K the Boltzmann constant and T_{eff} and ϕ_+ respectively the moderator effective temperature and work function. In a similar manner as detailed above, the use of an effective temperature is required in order for the predictions to fit the data at low-temperature or very low positron incident energy, but is consistent with thermal broadening alone models at higher temperatures [SSG+13]. This was confirmed experimentally for W(110) at room temperature: the calculated value of the FWHM of the angular distribution of re-emitted positron $\theta_{\text{FWHM}} = 2 \times \theta_{1/2} = 10.8°$ is consistent with the value measured experimentally in [FLG86], as seen in Figure 3.8b.

The brightness of a beam represents its capacity to be physically small and also to have a low energy and angle spread. It is defined by:

$$B = \frac{I}{\theta^2 d^2 E}, \tag{3.8}$$

with I the intensity of the beam (particles/s), θ its angular divergence, d its diameter and E the energy of the particle. Moderated positron re-emission is non-conservative and therefore not concerned by Liouville's theorem[4]: a beam of moderated positrons can be focused, once or more, on a moderator to produce a brighter beam [FGL85]. This process is called remoderation.

Conclusion

The positron, the anti-electron particle, has been introduced as well as its interactions in a solid with a focus on the unique possibility for positrons to create a

[4] Liouville's theorem states that the phase space volume of a beam remains constant under conservative forces, such as electromagnetic fields.

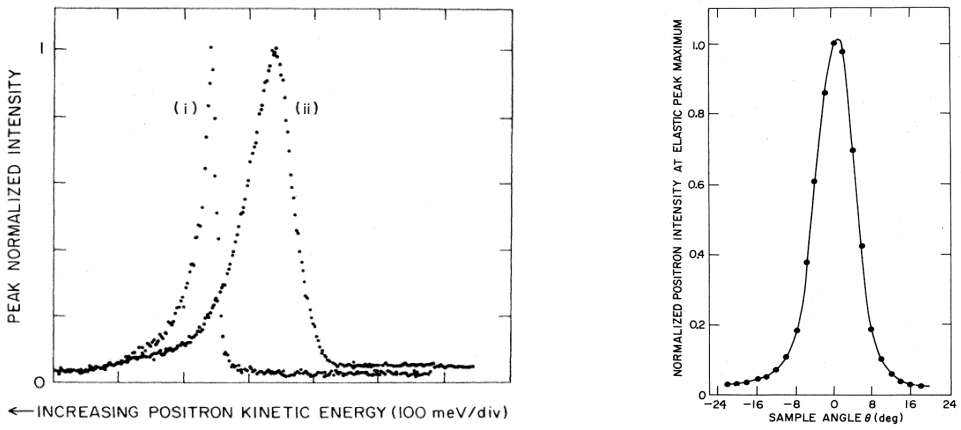

(a) (b)

Figure 3.8. (a): Normalized energy distribution of re-emitted positrons from Ni(100) at 300 K (ii) and 23 K (i) with FWHM of respectively 80 meV and 24 meV. (b): Angular distribution of positrons re-emitted from a W(110) crystal at room temperature. The FWHM of the peak is $\theta_{\mathrm{FWHM}} = 10(1)^{\circ}$. Both figures are taken from [FLG86]

well defined beam. The CALIPSO source is designed around the use of a material with a negative positron work function, a W(110) crystal, coupled with a β^+ radioactive source to create a beam of low-energy positrons with a narrow energy and angular spread.

Chapter 4

Geant4 simulations

> You can prove anything you want by coldly logical reason—if you pick the proper postulates.
>
> *(Isaac Asimov, I, Robot)*

Contents

4.1. Structure of the Geant4 simulations 36
4.1.1. Generation of primary events 38
4.1.2. Definition of the system geometry 39
4.1.3. Simulation output 40
4.2. Integration of Electro-Magnetic fields 41
4.2.1. Structured vs un-structured grids 41
4.2.2. Field computation 42
4.2.3. Field interpolation for structured grids 44
4.2.4. Un-structured grids 45
4.3. Moderated positron re-emission process 51
4.3.1. Estimation of the process 52
4.3.2. Implementation in Geant4 52
4.4. Data analysis tools 53
4.4.1. ROOT 53
4.4.2. Data analysis program 54

The creation of the *a*SPECTino spectrometer and the CALIPSO source required many simulations to check their design's viability and to optimize the setups. It is a complicated system to simulate as it is composed of a complex magnetic field, electrostatic field and geometry. For these reasons the simulations were performed using a simulation code, Geant4, which handles the particle tracking and interactions, but also using several other tools to deal, for example, with the electro-magnetic field calculation. The general structure for the simulations is described in Figure 4.1.

This chapter will briefly introduce the Geant4 simulation tool and describe the important features that were used or added. A focus will be made on the elec-

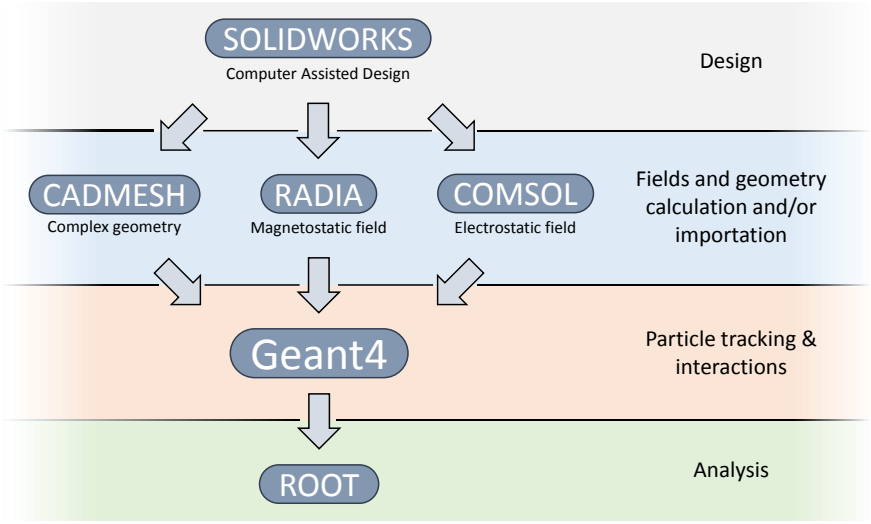

Figure 4.1. Global structure of the simulations. First the system is designed under SOLIDWORKS, a Computer Assisted Design software. Resulting information and geometry files are then used to compute electromagnetic fields using RADIA and COMSOL (see Section 4.2.2) and to define the simulation geometry using CADMESH (see Section 4.1.2). The particle tracking and all the interactions are computed by Geant4 which uses the geometry and electromagnetic fields issued from the previously quoted software. Simulations data is then treated using ROOT libraries (see section 4.4.1).

tromagnetic fields calculation using the external software RADIA and COMSOL and their integration into Geant4 using the Celltree structure (see Section 4.2). All the simulation's results will then be directly introduced in Chapters 5 to 7 where they are relevant.

4.1. Structure of the Geant4 simulations

Geant4, which stands for GEometry ANd Tracking, is a free C++ object-oriented code that uses Monte Carlo[1] methods to simulate the tracking of particles and their interactions through matter [A+03]. The GEANT series of simulation code started in the 70's at CERN and the initial release of Geant4 is from 1998. I used different versions of Geant4: from version 9.6 to version 10.2-patch02, released the 17th June 2016. All those simulations were developed as a mono-threaded code because Geant4 offers multi-threading possibilities only since version 10.0. There were no major reasons to update the code accordingly as no clusters or highly-threaded workstations were accessible: those simulations were performed

[1]Monte Carlo methods use random numbers and a large data sampling to determine the outcome of a problem. A very simple example is to roll a n-faces dice. At high statistics, if the dice is not biased, each face should have appeared as frequently as the others and matches their $1/n$ probability to appear.

on a standard industrial computer equipped with an Intel i5-3550S (4-cores at 3.0 GHz each) processor and 16 Gb of RAM.

The code of Geant4 is organized in several classes that can be adapted to the needs of the simulation. For instance, the user can define the complete geometry of the system in the *DetectorConstruction* class or define what should be done at each step of a particle's track in the *SteppingAction* class. Figure 4.2 shows the structure I used in the frame of this work.

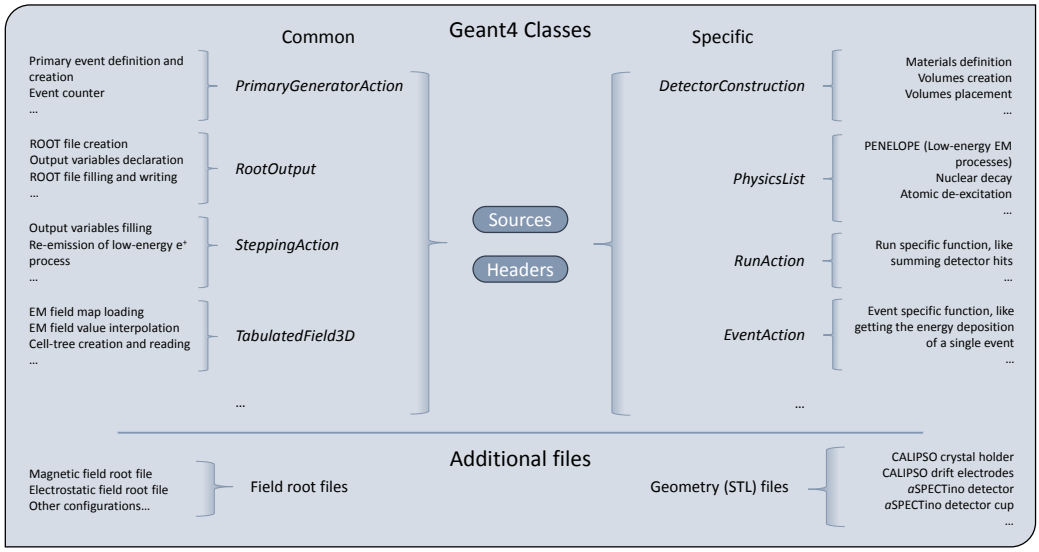

Figure 4.2. Scheme of the file structure used for the Geant4 simulations. Several classes are common for all the simulations, like the output ROOT file or EM fields handling. Others are specific to each type of simulation, like the geometry: a simulation focused on the *a*SPECTino detector and one focused on the CALIPSO source extraction field will not use the same geometry. There are also some additional files, like the ROOT files containing the EM fields maps (see Section 4.2).

Because of the low-energy component of the particles we are interested in, the PENELOPE physics list was used. This package contains precise electromagnetic (EM) models in the low-energy region (from 1 GeV down to 100 eV) for gammas, electrons and positrons. Radioactive decays are treated empirically using the ENSDF[2] database by the *RadioactiveDecay* class. In this work, it was used to evaluate the radiation level of the ^{22}Na source of CALIPSO.

When a particle is evolving inside an EM field, its trajectory is propagated using a stepper. The user can define and modify the stepper itself but also its parameters, such as its precision, as shown in Figure 4.3. In this work the robust 4^{th} order Runge-Kutta[3] stepper was used.

[2]The Evaluated Nuclear Structure Data File is a freely accessible list of nuclear properties derived from measurements. More information can be found in [Tul96].

[3]It is an iterative method to approximate differential equations solutions that was formulated in 1901 by two mathematicians: Carl Runge and Martin Wilhelm Kutta.

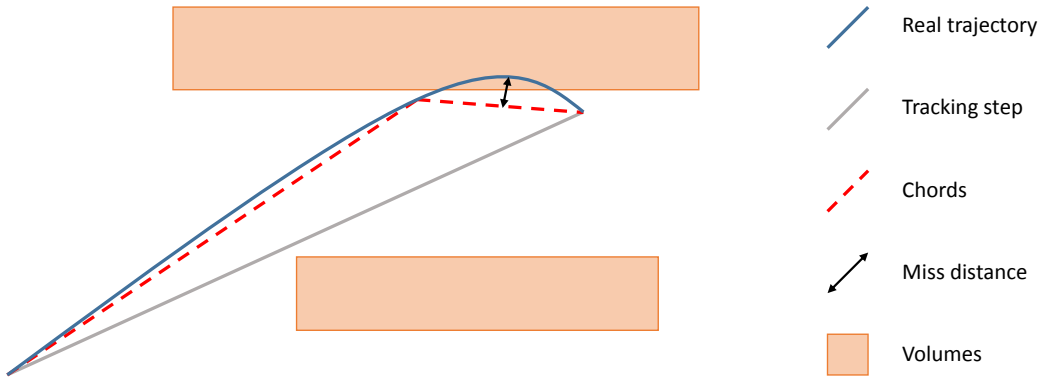

Figure 4.3. The stepper precision is handled through several parameters, like the *miss distance*. Real trajectories are approximated by linear segments, chords, to check for volume hits. The precision of this approximation is defined by the sagitta between the real trajectory and the chord: the *miss distance*. The resulting tracking step can be the resultant of several chords, as a step is defined only when something is happening to the track, like an interaction or a volume hit. This scheme is directly inspired from the Geant4 online documentation [Col16].

4.1.1. Generation of primary events

A primary event includes the initial track created by the user and all the resulting secondary tracks. In a mono-threaded scenario, primary events are treated one after the other. The user can define all the characteristics of the primary events, such as the position, the energy, the momentum or the particle type. Those initial properties can be discrete, randomly generated from a distribution or a process (e.g., the ^{22}Na β^+ decay).

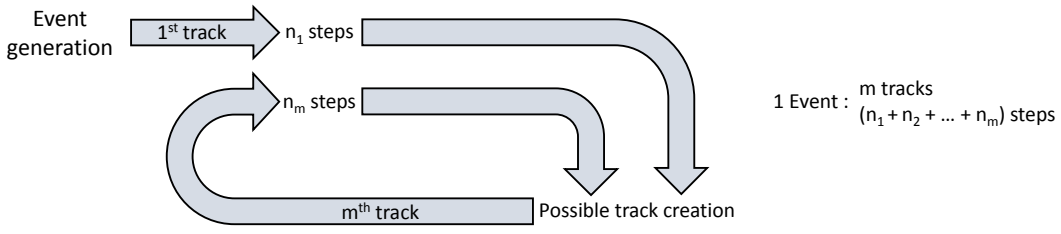

Figure 4.4. Basic scheme of Geant4 handling of events and tracks. A primary event, generated through the *PrimaryGeneratorAction* class, will interact with its environment along each of its step and may create new tracks, who can also generate new tracks themselves. Each track has a parent and several tracks can have the same parent.

Each primary event evolves inside the geometry of the simulation and can

interact with its surroundings. Depending on the energy cuts set by the user, this can result in new tracks that are piled-up in a stack until the primary event is fully treated. When an energy cut, a physical process or even an arbitrary condition set by the user kills a track, the top one on the stack is treated: this is the rule of the "*last in first out*". The simulation of a single primary event can then result in one or more tracks, as shown in Figure 4.4.

4.1.2. Definition of the system geometry

The CADMESH [PCTL12] package was used to easily import complex geometries designed within SolidWorks into Geant4. This library uses an STL[4] file as an input and then the Geant4 *TesselatedSolid* class to create the corresponding object into the simulation. The triangle mesh inherited from the STL file structure allows for complex geometries to be approximated more or less precisely, depending on the selected accuracy of the exportation process. In order not to slow down simulation, the system geometry should be precise and well defined only at the relevant places. As a result simplified versions of the SolidWorks designs were used for both the Geant4 simulations and the electric field map computation (see Section 4.2.2), as shown in Figure 4.5.

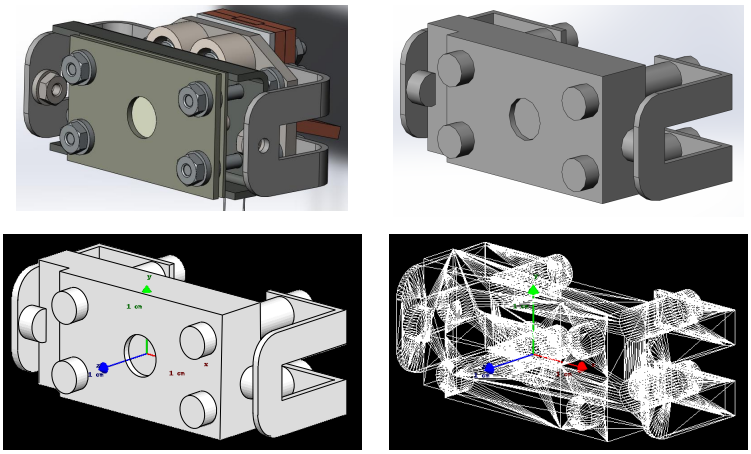

Figure 4.5. Example of geometry simplification and importation from SolidWorks into Geant4. An assembly, here the crystal holder of CALIPSO, is designed in details under SolidWorks (top left) and then converted into a simpler and single object, still under SolidWorks (top right). After exportation into the STL file format it is imported, through CADMESH, into Geant4 as a tessellated volume. An OpenGL visualization tool can then be used to look at the geometry used by Geant4: here in the *surface* mode (bottom left) and the *wireframe* mode (bottom right).

[4]This acronym stands for STereoLithography and originates from the company 3D Systems, whose former president invented stereo-lithography. It became a very widespread file format for 3D printing and exporting geometries using a raw un-structured triangle mesh.

4.1.3. Simulation output

As Geant4 was employed to define and optimize the design of the *a*SPECTino spectrometer and the CALIPSO source, the simulation's content was evolving a lot. I therefore decided to get output files with as much information as possible and to develop an independent tool to analyze the data post-simulation (see Section 4.4.2). Such a setup provides a lot of flexibility on what can be looked at but at the price of bigger output files and slower simulations and analysis. For runs dedicated to specific studies, the possibility of lighter output files was kept by cutting some variables through the use of options in the code, as shown in Figure 4.6.

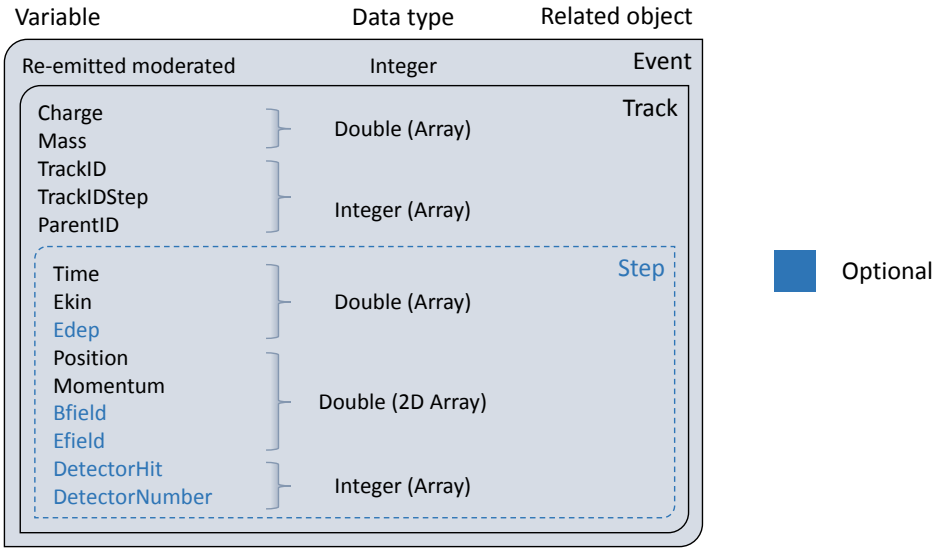

Figure 4.6. Structure of the output variables of the simulation. Each variable has a defined data type and is evaluated at different moments of the simulation: at the beginning of an event, at the beginning of a new track or at each step. For lighter runs, it is possible to remove some variables from the output (in blue) and/or to only save the first and last step of each track, instead of all of them.

The *Re-emitted moderated* variable differentiates positrons born from the re-emission process (see Section 4.3) and is defined for the whole event, allowing an easy selection of the photons coming from those re-emitted positrons in the post-analysis (see Section 4.4.2). Each track charge and mass is saved in the homonymous variable. *TrackID* and *TrackIDstep* refer respectively to the unique track reference number and to the step number where this track appeared, whereas *parentID* refers to the ID of its parent (non-existent for the first track of an event). *Time*, *Ekin*, *Position*, *Momentum*, *Bfield* and *Efield* correspond respectively to the absolute time of the step (with 0 being the first step of the event), the kinetic energy of the track, it's position, it's momentum and the value of the magnetic and electrostatic field at this step/position. *DetectorHit* tracks the step number

where a track hit a detector and *DetectorNumber* references which detector was hit, whereas *Edep* sums all the deposited energy while the particle is inside a detector.

4.2. Integration of Electro-Magnetic fields

Electro-Magnetic fields are innately implemented in Geant4 and one can easily set one or several uniform EM fields in the simulation geometry. However Geant4 cannot compute more complex EM fields.

One way to solve this is to use an external field calculator first and then import the field into Geant4. This is practical as one can pre-compute several setups and then use the wanted field map. Furthermore, once the field is loaded at the beginning of the simulation, only a small amount of computational power is required: the field interpolation from the surrounding nodes of the field map at the desired point. However the precision of the interpolation is dependent of two parameters: the interpolation method (the more precise the slower the simulation) and the field map resolution (the higher the bigger the field map). One can then be limited by computation time or memory size if the method is not adapted to the problem.

The other possibility is to compute the field at the desired point each time Geant4 needs to access it, which requires an EM field solver implementation into the Geant4 code. This method is very precise, as there is no interpolation anymore, and there is no need for a field map. Nevertheless, since the field has to be computed each time Geant4 calls for it, such a solution is extremely slow for complex systems.

4.2.1. Structured vs un-structured grids

Because of the complexity of the EM fields of the setup (especially in the CALIPSO source) and the better versatility of the first method, the use of the interpolation of pre-calculated field maps appeared as the best option. Using this solution offers two possibilities for the format of the field map: structured or un-structured grids.

Using a structured map offers several advantages: finding the cell where a point sits is very fast, a complex (but slow) interpolation can be performed without to much efforts and, to some extent, one can create an adaptive mapping through the use of different cell sizes for different regions of the map. However if the map is very inhomogeneous then it can become very complex and fastidious to deal with the different cell sizes, especially if one wants smooth transitions. Another defect with this method is related to the behavior of the field calculation and interpolation at the border of an object whose boundaries also define the boundary conditions for the field calculation (typically a metallic object for an electrostatic field calculation). As illustrated in Figure 4.7, structured grids are not at all well-suited in such cases.

Structured map are therefore more adapted to low-gradient fields where object boundaries are not impacting the field calculation. The coils of *a*SPECTino are

sitting outside the vacuum chamber and the magnetic field is relatively homogenous (see Section 5.2). As a result a regular structured grid is a solid choice to handle the magnetic field map of this setup.

On the other hand and as stated above, the electrostatic field is complex, highly inhomogeneous and needs to be known correctly at the border of objects (e.g., inside CALIPSO). An un-structured grid was therefore used for the electrostatic field mapping.

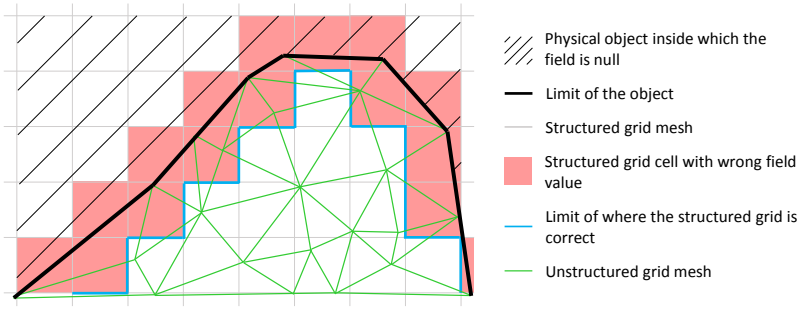

Figure 4.7. Comparison of a regular, structured grid with an un-structured grid at the peripheral of a complex object. We take the example of an electric field calculated with an FEM solver, with the object's edges defining the boundary conditions. Because the field value is zero inside the object, all the structured grid cells containing at least one node sitting inside the object are compromised, resulting in a wrong field interpolation. In such cases, like particle tracking close to the object's surfaces, using an un-structured grid is mandatory as it fits to the object's boundaries.

4.2.2. Field computation

The magnetic field calculations were performed using RADIA[5]. Coil sizes, positions and current densities were implemented and then the field computed at each node of a regular 3D grid: the mesh of the magnetic field map. The output for the whole setup (the inside of the aSPECTino spectrometer) is a grid of $160 \times 160 \times 2700$ mm^3 with each cell being $1 \times 1 \times 1$ mm^3, for a total of around 70 millions evaluated points. It takes about two days to perform the whole computation on a single thread of the computer described in the introduction of this chapter. The three magnetic field components of each point are stored in *.csv* files for a total of 4.56 Gb and then a home-made C++ program creates a ROOT file (see 3Section 4.4.1 for more details about ROOT) to efficiently store the field

[5]RADIA is a C++ code interfaced to Mathematica and developed at the ESRF, in Grenoble. It is a fast and precise magneto-static solver that uses boundary integral methods. A matrix describing mutual interactions between all the elements is built and then a relaxation procedure is performed. Field values and integrals are then computed by summing the contributions of each element and external sources [CEC98].

map, resulting in a 1.3 Gb file.

Electrostatic fields were computed using a Finite Element Method[6] software. The geometry of the setup was directly imported from SolidWorks into COMSOL Multiphysics[7]: the FEM solver used in this work.

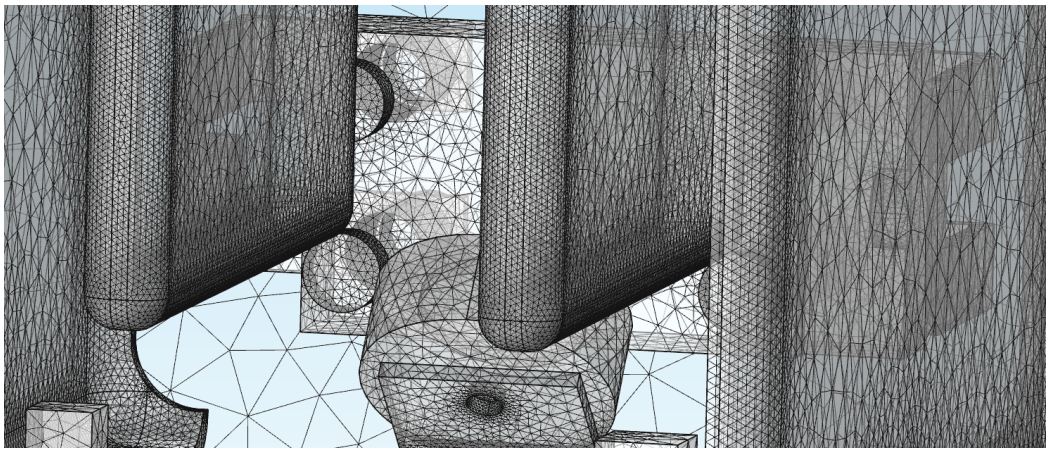

Figure 4.8. Example of an un-structured mesh mapping from COMSOL showing some parts of the CALIPSO source: the drift electrodes (at the front left and center), the ^{22}Na source capsule (bottom) and the crystal holder (back). In this picture only the tetrahedron faces defining the boundary conditions of the simulation are shown. The complete related 3D mesh is also generated but not displayed directly in the software for visibility reasons. In this case, no volumes are created inside the different parts of the system, only the "vacuum" is considered as a volume and is mapped. Such a geometry can therefore have several empty regions, and only the relevant space is treated.

The highly-adaptive 3D tetrahedron[8] mesh is created by COMSOL and the user can further change the global mesh resolution, set the maximum size of an element and so on. The software, and any mesher in general, will create a mesh that will fit any curvature and angle within the desired resolution, as illustrated in Figure 4.8. Once the field is calculated, the data is exported in a text file and, similarly to the structured grid, a home-made C++ program converts it into a ROOT file. One element (a tetrahedron) is described by four node numbers, and each node is characterized by coordinates, field values (one for each axis) and a number. The un-structured grid treatment is detailed in Section 4.2.4.

[6]The Finite Element Method, or FEM, is used to build approximation of partial differential equations in order to solve them using numerical methods. The higher the discretization, the better the precision of the result will be, at the price of memory and computing time.

[7]COMSOL is a powerful commercial FEM solver equipped with a user-friendly Graphical User Interface (GUI).

[8]Also known as "triangular pyramid", tetrahedrons are polyhedrons made of four vertices//nodes and four triangular faces. They are widely used as elementary volume to create complex 3D objects.

4.2.3. Field interpolation for structured grids

At the beginning of a simulation, if a magnetic field map is used, the structured map is read from the desired ROOT file and loaded in the RAM of the computer. Each time Geant4 requires an access to it, a routine computes the interpolated field value following the algorithm described in Figure 4.9 and using the linear interpolation described in Figure 4.10.

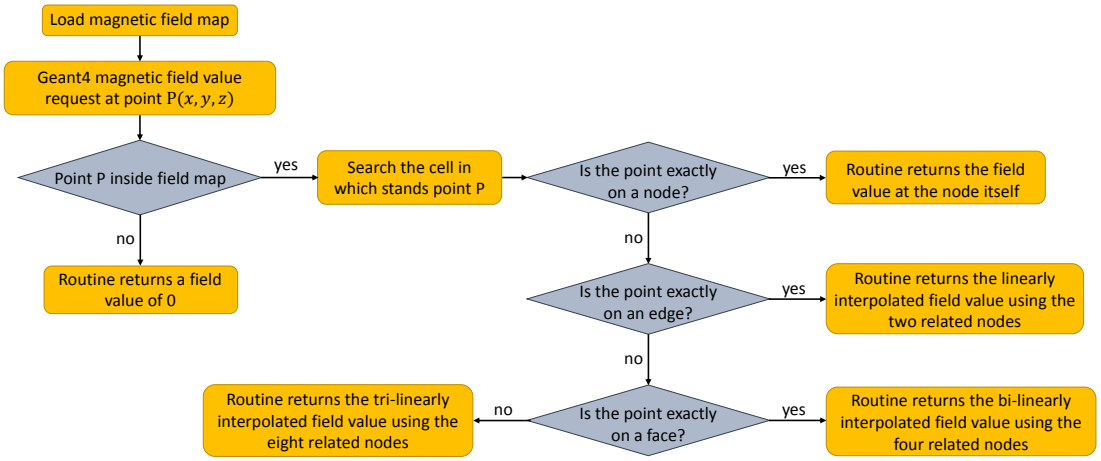

Figure 4.9. Flowchart of the magnetic field map interpolation routine. Coordinates of a point are used as an input and the routine searches where this point stands compared to the regular structured grid. Most likely the point is not exactly at a node's position and a linear interpolation is performed: purely linear (1D) if the point sits on an edge of a cell, bi-linear (2D) if it sits on a face of a cell and tri-linear (3D) otherwise.

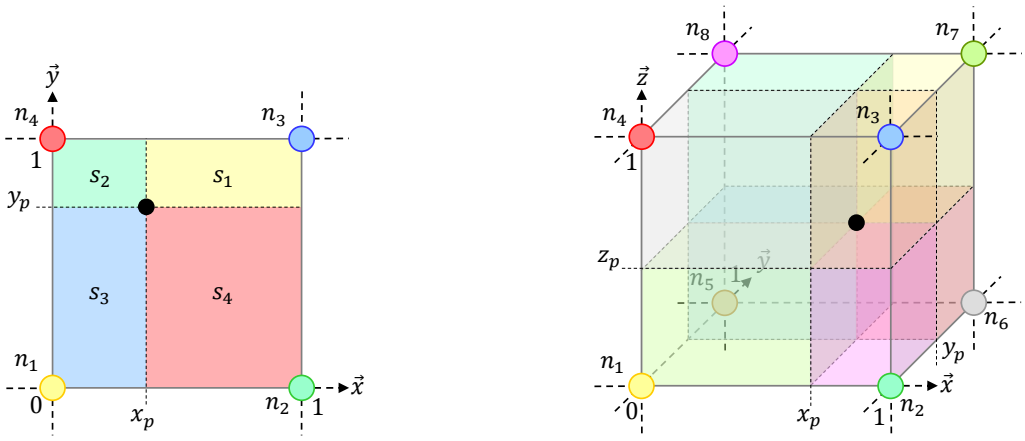

Figure 4.10. Scheme of bi-linear (left) and tri-linear (right) interpolation in structured grids. A particle (black point) stands in a normalized cell of a structured grid: either a square (2D) or a cube (3D). The linearly interpolated value of the field at the particle's position is the sum, over all the cell's nodes, of the product of the field value at the node and the surface (2D) or volume (3D) opposite to this node in the cell. This scheme is inspired from [Wik17b]

4.2.4. Un-structured grids

Because of their nature, finding in which cell a given point is belonging to is a big problem when using un-structured grids. Such setups are widely used in Computer-Generated Imagery (CGI) and FEM solvers, and many efforts were made to develop fast and robust algorithms for this task. The general process is to create a data structure called tree, built from the map, that contains a node hierarchy. Even though there are a many different tree structures the building process is usually as follows:

- The root node, which contains the list of all the cells of the map, is split (the splitting method depends on the tree structure).
- The list of cells is transferred from the root node to the relevant child nodes. The root node now only contains the split information (e.g., a plane).
- The split is performed again on each child node in the same way it was done for the root node. A node that is not split is called a leaf and the depth d of a leaf means that d splits were performed to reach it.
- This process goes on for each node until a condition defined by the tree structure is met (e.g., when a defined tree depth is reached or when each leaf contains less than n cells).

Once the tree is built, it is composed of nodes, which contain their split information, and leaves, which contain the list of cells resulting of the splits. In

order to get a better understanding of such structures, Octrees and Kd-trees are introduced as examples. Quadtrees, the two-dimensional version of Octrees, were one of the first options used [Mor66]. In the case of octrees the space is divided in eight children each time a split is performed. This results in all the three dimensions being split at the same time. Kd-tree, another famous structure, stands for k-dimensional tree [Ben75]. Kd-tree splits are performed in one dimension at a time only, and not necessarily in the median plane of the volume to split. Quadtree and Kd-tree structures are shown in Figures 4.11 and 4.12. For both solutions the cell is duplicated in both node children if the split axis goes through a cell, resulting in a bigger tree and consequently worse performances, as detailed in Figure 4.13.

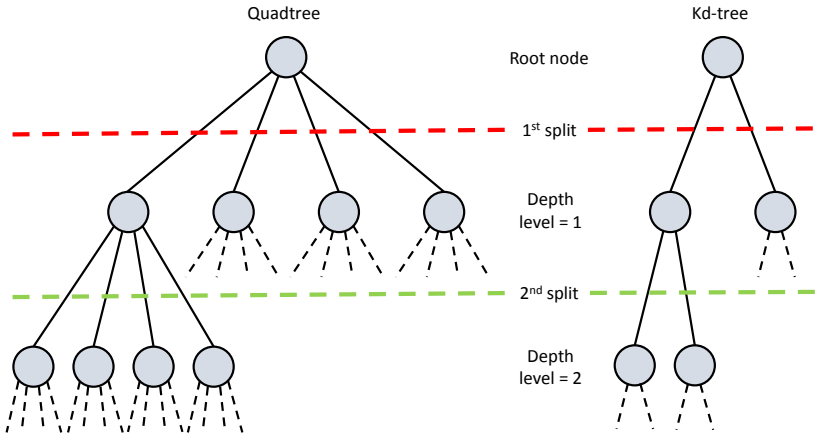

Figure 4.11. Quadtree (left) and Kd-tree (right) structures. For Quadtree each split creates four new nodes whereas for Kd-tree it is only two. The root node contains the 1st split information, nodes at a depth level $d = 1$ the 2nd split information and so on.

When a *FindCell* request is sent, the tree is traversed to find the correct cell where the point sits in. This operation is performed by comparing the point coordinates to the root node split, traversing the correct child node (the one that contains the point) and repeating this traversal until a leaf is reached. All the cells of this leaf are then tested until a match is found (the point sits in this cell) or not (the point is not contained in any cell).

While looking for cell location methods in un-structured grids, a fast, robust and efficient data structure introduced in 2010 was found: the Celltree [GJ10]. It was therefore used and it is briefly described below.

4.2.4.1. Celltree structure

Celltrees are similar to the usual data structures previously introduced as they split the map volume recursively while storing the list of cells in the leaves of the tree. Their particularity resides in a bounding interval hierarchy: splits are forming a disjoint partition of cells. As described in Figure 4.14, splits are deter-

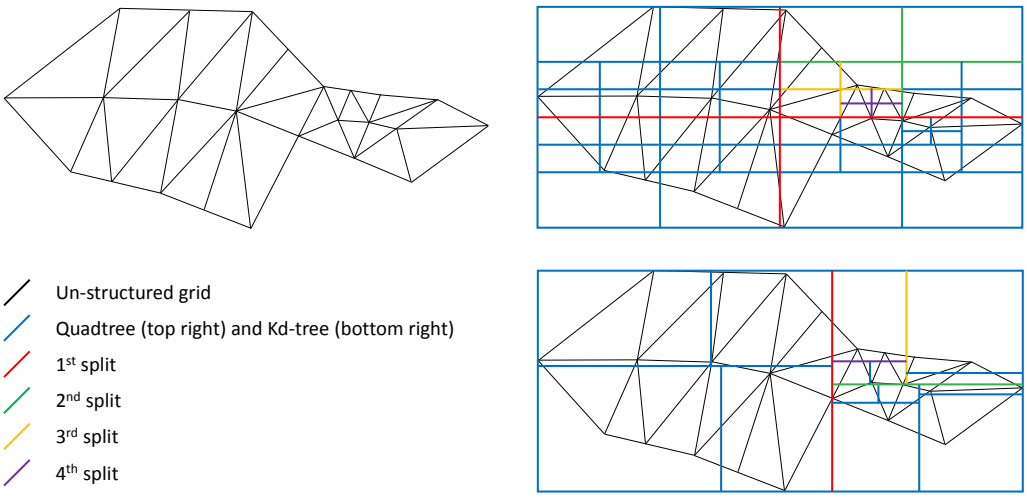

Figure 4.12. Scheme of an arbitrary un-structured 2D grid (top left), a Quadtree (top right) and a Kd-tree (bottom right). Both trees with their typical splits are applied to the same un-structured grid and the first four splits of each tree are colored. The leaves of the tree are not necessarily all at the same depth and a different number of traversals may be required to reach different cells.

mined using buckets which are filled with centers of cell bounding boxes[9]. The best split plane (or axis in 2D) is the one minimizing, for all dimensions, the cost C:

$$C = L^d_{max} \cdot N_L + R^d_{min} \cdot N_R, \tag{4.1}$$

with $d = 0, 1, 2$ the split dimension, L^d_{max} and R^d_{min} are the relative position of respectively the maximum bounding plane of the left list and the minimum bounding plane of the right list compared to the complete bounding box size along the split dimension of the list of cells to split and N_L and N_R the number of indices stored respectively in the left and right lists. The number of buckets used to determine the best split is set to five. Splitting goes on until leaves are composed of less than eight cells (both optimal bucket number and leaf size were determined empirically [GJ10]).

A direct consequence of this structure is that the cell duplication problem no-longer exists, but if a point sits inside the two split planes then both children must be traversed. In this case the subtree whose bounding plane (either L^d_{max} or R^d_{min}) is farther away from the point is traversed first and the other one is put at the top of a stack. Once a leaf is reached every cell is tested for the point inclusion. If the point is not contained in the first subtree, the node sitting at the top of the stack is treated.

[9]Bounding boxes refer to axis-aligned minimum bounding boxes (AABB). It is the smallest box in which all the points of the element (here a tetrahedron) are included, with the edges of the box being parallel to the coordinate axes.

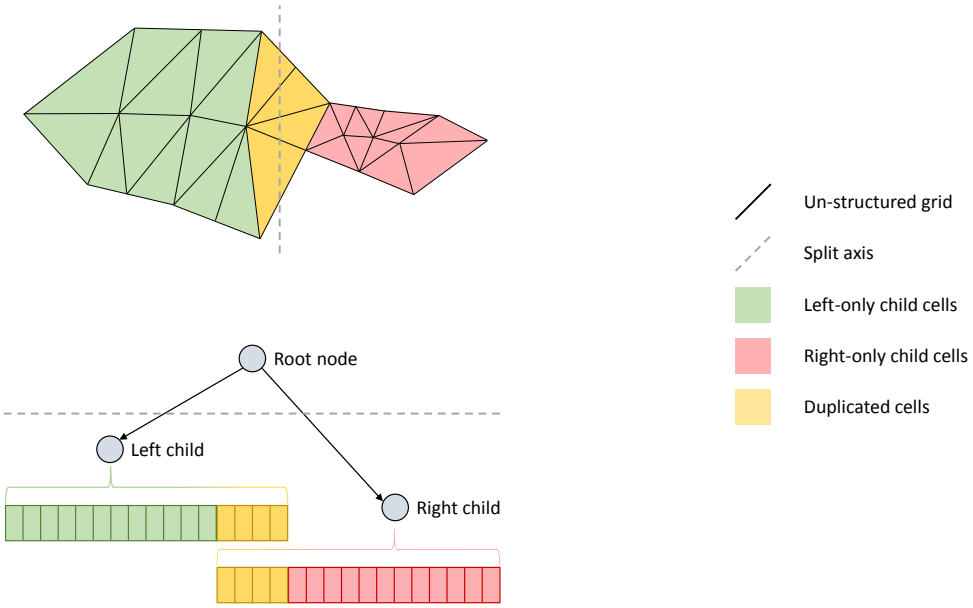

Figure 4.13. Cell duplication problem in trees with joint partition splitting. In data structures like Octrees or Kd-trees, the split usually goes through a lot of cells which have to be stored in all concerned children. This leads to trees with a total number of cells much higher than the initial data to treat.

4.2.4.2. Point inclusion test

The inclusion of a point in a tetrahedron is tested by comparing signed volumes. A tetrahedron T defined by four vertices $V_i(x_i, y_i, z_i)$ has a signed volume denoted $[V_1V_2V_3V_4]$ and defined by:

$$[V_1V_2V_3V_4] = \frac{1}{6}\begin{vmatrix} x_1 & y_1 & z_1 & 1 \\ x_2 & y_2 & z_2 & 1 \\ x_3 & y_3 & z_3 & 1 \\ x_4 & y_4 & z_4 & 1 \end{vmatrix}. \tag{4.2}$$

T includes a point $P(x, y, z)$ if $[V_1V_2V_3V_4]$ has the same sign as each of the four signed volumes $[PV_2V_3V_4]$, $[V_1PV_3V_4]$, $[V_1V_2PV_4]$ and $[V_1V_2V_3P]$ of the four tetrahedrons formed by P and the four vertices of T [FT97]. The absolute value of the volume is not required to perform the point inclusion and the scaling factor $\frac{1}{6}$ can therefore be ignored. In the end those five determinants are computed:

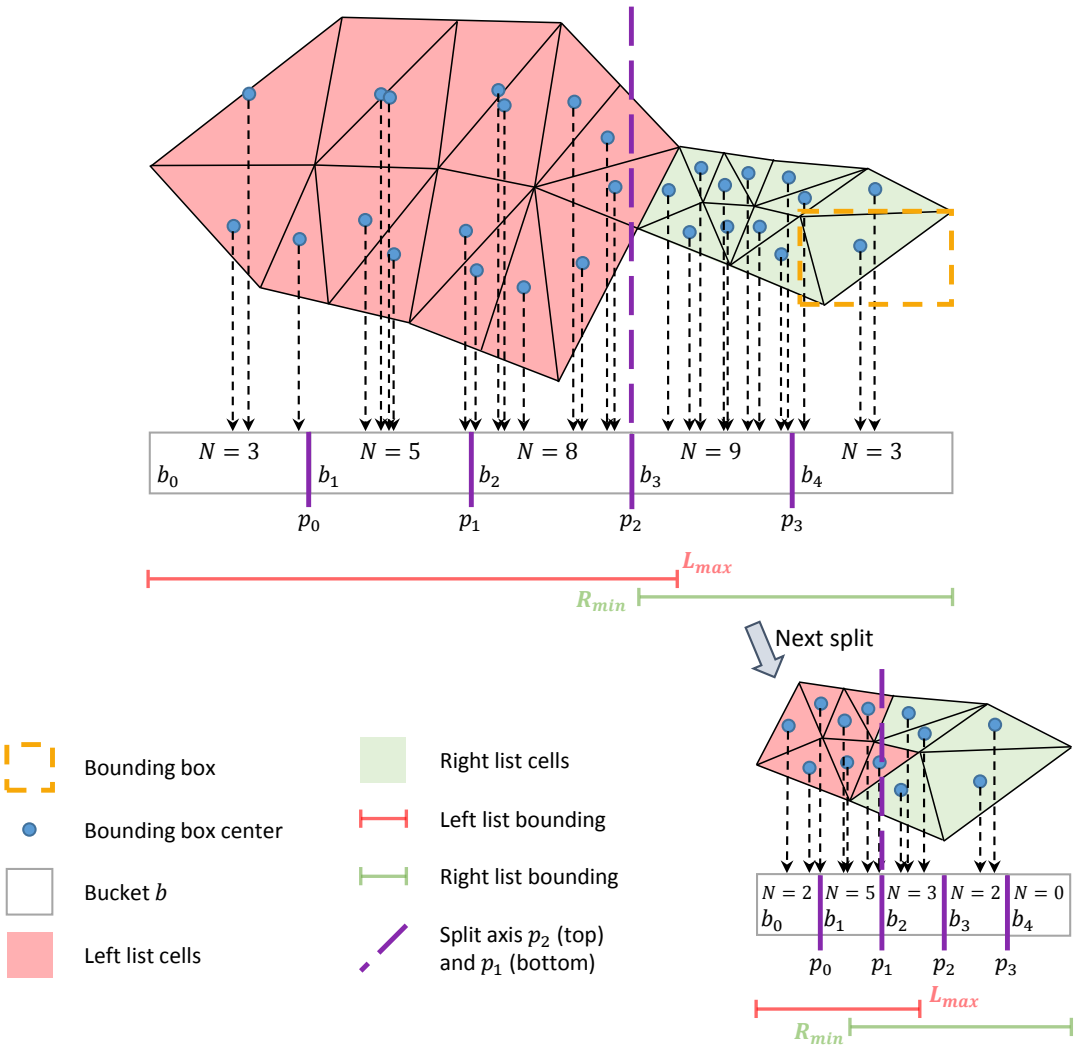

Figure 4.14. Description of the Celltree structure using an arbitrary unstructured grid. Centers of the bounding box of each cell are sorted into buckets and the cost C (see equation (4.1)) is minimized. In this example C is minimal at the root node for the splitting axis p_2. The resulting left and right lists are then defined and another split on the right list is performed as an example. This time C is minimal for p_1. Each time a split is performed, both L^d_{max} and R^d_{min} are stored. It is important to note that for the simplicity of the scheme the vertical dimension was not tested, but should have been. This scheme is inspired from [GJ10]

$$D_0 = \begin{vmatrix} x_1 & y_1 & z_1 & 1 \\ x_2 & y_2 & z_2 & 1 \\ x_3 & y_3 & z_3 & 1 \\ x_4 & y_4 & z_4 & 1 \end{vmatrix}, \qquad D_1 = \begin{vmatrix} x & y & z & 1 \\ x_2 & y_2 & z_2 & 1 \\ x_3 & y_3 & z_3 & 1 \\ x_4 & y_4 & z_4 & 1 \end{vmatrix},$$

$$D_2 = \begin{vmatrix} x_1 & y_1 & z_1 & 1 \\ x & y & z & 1 \\ x_3 & y_3 & z_3 & 1 \\ x_4 & y_4 & z_4 & 1 \end{vmatrix}, \qquad D_3 = \begin{vmatrix} x_1 & y_1 & z_1 & 1 \\ x_2 & y_2 & z_2 & 1 \\ x & y & z & 1 \\ x_4 & y_4 & z_4 & 1 \end{vmatrix},$$

$$D_4 = \begin{vmatrix} x_1 & y_1 & z_1 & 1 \\ x_2 & y_2 & z_2 & 1 \\ x_3 & y_3 & z_3 & 1 \\ x & y & z & 1 \end{vmatrix}. \tag{4.3}$$

The sign of D_1, D_2, D_3 and D_4 are then compared to the sign of D_0 and the point inclusion routine returns either the *CellNumber* in case of a match (all the signs are the same) or a *0* otherwise. In case of a match, the computed determinants are also used for the field interpolation inside the tetrahedron, as detailed in Section 4.2.4.3.

4.2.4.3. Field interpolation for un-structured grids

In the case of un-structured grids, a similar linear interpolation as in Section 4.2.3 was used. As described in Figure 4.15, the interpolated value of the field at point P is the sum of each node field value times the opposite normalized area (2D) or volume (3D). As seen in Section 4.2.4.2, those values are already computed (at a factor six close) when dealing with point inclusion. Furthermore only the ratio of each sub-tetrahedron formed by the point P and three nodes of the cell over the full cell volume is required, canceling the missing factor $\frac{1}{6}$. Those ratios $\frac{D_i}{D_0}$ are also called the barycentric coordinates. In the end the interpolated field value can be calculated using the already known determinants detailed in Equation (4.3):

$$E_P = \sum_{i=1}^{4} E_{n_i} \cdot \frac{D_i}{D_0}, \tag{4.4}$$

with E_P the interpolated field value at point P, E_{n_i} the electrostatic field value at the node i and D_0 and D_i the determinants detailed in equation (4.3).

4.2.4.4. Implementation in Geant4

Thanks to its very high performance, the Celltree structure was introduced in several viewer software and graphics libraries. As a result, one can find the

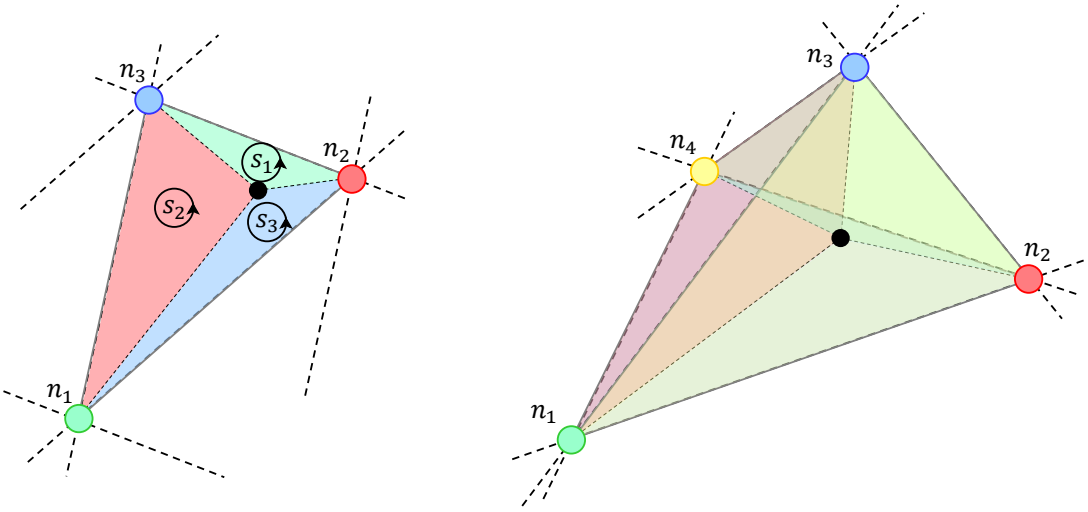

Figure 4.15. Scheme of bi-linear (left) and tri-linear (right) interpolation for triangular (2D) and tetrahedronic (3D) cells in un-structured grids. As in Figure 4.10 the black dot represents the particle in the cell. The point inclusion method described in Section 4.2.4.2 pre-calculates the sub-volumes of the cell represented by colored tetrahedrons.

Celltree implementation in the VTK library[10]. The relevant part of the code were extracted and the Celltree structure introduced inside the *TabulatedField3D* class. This part of the code includes the structure of the Celltree, its building and the tree traversal. The point inclusion test and the field interpolation method were not part of this package and the methods described respectively in Sections 4.2.4.2 and 4.2.4.3 were used.

When running a simulation, Geant4 first loads the electrostatic field map, builds the corresponding Celltree and then uses it every-time an electrostatic field request is sent. Once the cell for the requested point is found an interpolation routine is performed to get the field value from the four vertices of the tetrahedron.

4.3. Moderated positron re-emission process

In order to design and optimize the CALIPSO positron source it was useful to add the moderated positron re-emission process into the simulations, as it is not innately implemented in Geant4 (work functions themselves are not integrated). As seen in Chapter 3 the efficiency of this process is closely related to the quality of the moderator crystal: the less the defects the higher the efficiency. Parameters such as the surface quality of the moderator or its defect density cannot be considered explicitly in the simulations. A possible solution is to take a statistical approach and to use parameters that will fit the typical efficiency measured exper-

[10]Visualization ToolKit is a C++ class library and an "open-source, freely available software system for 3D computer graphics, image processing, and visualization" (see http://www.vtk.org/). It was created in 1993 by three researchers of General Electric, on their own time.

imentally. The process can then be included with the correct order of magnitude and behavior.

4.3.1. Estimation of the process

Positron interactions are well described down to 100 eV when using the PENELOPE physics list [I+11]. Once a positron reaches this low-energy limit it deposits, by default, all its left energy at a step, independently of the material, and briefly diffuses before being annihilated. The diffusion length is linked to the moderator crystal quality, which is not implemented in the material properties in Geant4. As a result the typical diffusion of moderated positrons in Geant4 will not match the experimental values in the case of an annealed mono-crystal. In a reflection geometry the possibility for a moderated positron to diffuse back to the surface depends, for a defined crystal quality, on the distance between the position where the positron stopped and the surface. This can be modeled by the following 1D equation [KL09]:

$$f = e^{-a/L_{+\text{red.}}}, \tag{4.5}$$

where f is the fraction of positrons stopped at depth a that will diffuse back to the moderator surface and $L_{+\text{red.}}$ the diffusion length. As seen in Section 3.3.2 typical diffusion length values for metals are ~ 1000 Å. Using the 1D approximation expressed above requires to use a reduced value for the diffusion length in order for Equation (D.6) to be consistent with experimental measurements of the efficiency [W+15]. A value of $L_{+\text{red.}} \approx 17$ nm can be derived from [KL09, W+15].

4.3.2. Implementation in Geant4

Inside Geant4 the process was implemented in two parts. First a routine was added in the *SteppingAction* class to test the probability that a stopped positron diffuses back to the moderator surface, as described in Figure 4.16. If the positron passes the test, its track is stopped and killed (but still saved) and a new one is created at the moderator surface with the properties of a re-emitted moderated positron in the *PrimaryGeneratorAction* class. This artificially created positron is tagged as *Re-emittedModerated* in the output of the simulation (see Figure 4.6).

In the case of a positron moderator surface normal to the z-axis of the simulation reference frame, the non-relativistic kinetic energy components of the re-emitted moderated positrons follow a Maxwell-Boltzmann distribution:

$$E_i = \frac{\mathcal{N}(0,1) \cdot k_B T^*}{2}, \quad i \in \{x, y\}, \tag{4.6}$$

$$E_z = \frac{\mathcal{N}(0,1) \cdot k_B T^*}{2} - \phi_+, \tag{4.7}$$

with E_i the positron kinetic energy component along the i axis in eV, $\mathcal{N}(0,1)$ a Gaussian random number with a mean value of 0 and a variance of 1, T^* the effective temperature in Kelvin, k_B=8.6173324 $\times 10^{-5}$ eV/Kelvin the Boltzmann

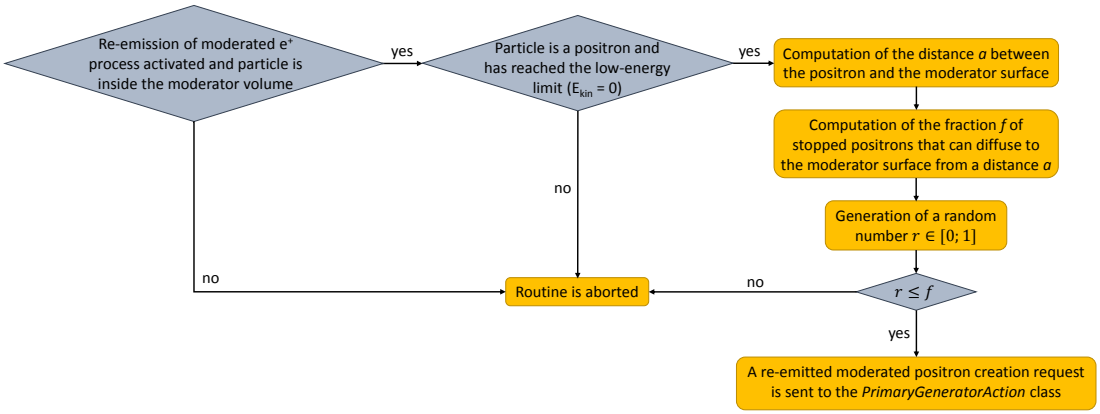

Figure 4.16. Flowchart of the test for moderated positron re-emission in Geant4. This test is performed at each step of any track. This test can only occur in the moderator volume defined by the user. In order to specifically look at the behavior of low-energy positrons, the test can be biased to allow every thermalized positron to diffuse back to the moderator surface by always passing the $r \leq f$ test.

constant and ϕ_+ the work function value of the moderator in eV. As the moderator positron work function is negative the contribution of $-\phi_+$ to the kinetic energy along the z-axis is positive. As described in Section 3.2.2 the effective temperature T^* is between 1 to 4 times higher than the moderator temperature T, depending on the system and the real temperature lattice. In the simulations this factor is set to $T^* = 1.7 \times T$ in order to fit with the available experimental data, resulting in a FWHM of the energy spread of 75 meV and 25 meV at respectively 300 K and 77 K.

4.4. Data analysis tools

Data coming from both the Geant4 simulations and the aSPECTino detector need to be treated and analyzed. A similar approach was used for both data-sets with the use of ROOT libraries and specifically developed programs based on these libraries.

4.4.1. ROOT

ROOT is a free C++ framework developed at CERN since 1994. Even-though it is designed for particle physics data analysis this library can be used for any data treatment. During this work the latest version I've been using was ROOT v5.34/19, released the 9$^{\text{th}}$ July 2014. ROOT provides a lot of different features, such as [A+09]:

- data visualization (up to 3D histograms, graphs etc.)
- curve fitting using iterative methods (such as MINUIT)
- standard statistic tools and mathematical functions

- efficient data storage and access
- graphical user interface (GUI) possibilities
- a command line interpreter

ROOT files are indicated by a *.root* extension and are a very efficient way to store and access the data. This file type uses a compressed binary format that is machine-independent and can deal with huge amount of information [CER17a]. Data can be organized in a tree structured in branches and leaves. Each branch can contain any kind of object (integer, float, vector, histogram etc.), those variables are called leaves.

When accessing an entry of the tree (e.g., a particle) one can access to each variable of this entry. If we define the tree with two branches, like a 3D vector *position* and a double *energy*, accessing an entry will give a direct access to both corresponding variables.

A strong feature of the ROOT library is the possibility to develop programs with a graphical user interface, all in C++. Typical graphical interface objects are integrated, such as buttons, menus, text and number inputs/outputs, plots etc. It is possible to link actions and functions to any kind of input and signal (e.g., a change in an input value).

4.4.2. Data analysis program

Thanks to the GUI packages included in ROOT I decided to develop a program that would ease on-the-fly analysis of the data from both the Geant4 simulations and the *a*SPECTino spectrometer itself. The goal of this software is to perform fast, easy and powerful analysis, even for someone not familiar with C++ or ROOT. Because the variables of the output files from the simulations and the *a*SPECTino detector are different, there are two versions of the software. Since the structure of the two codes is the same, these two programs will not be differentiated in the following section.

The program was first developed in 2013 and then upgraded regularly based on the project progress and needs. The way the code is built makes it easy to add features once the frame of the program is created. For instance, if one wants to look at the correlation between two variables, it is almost as fast to implement this in the software as to create a fresh macro without any interface. As a result the program offers more possibilities each time a new kind of analysis is required.

A screenshot of this program is shown in Figure 4.17 and more details of the program interface and its possibilities are shown in Appendix A.

Conclusion

The development and optimization of *a*SPECTino and CALIPSO require specific simulations. The structure and tools used or developed for those simulations were detailed in this chapter. The results issued from those simulations are presented in the following chapters which introduce the concept, development and characterization of the *a*SPECTino spectrometer and the CALIPSO source.

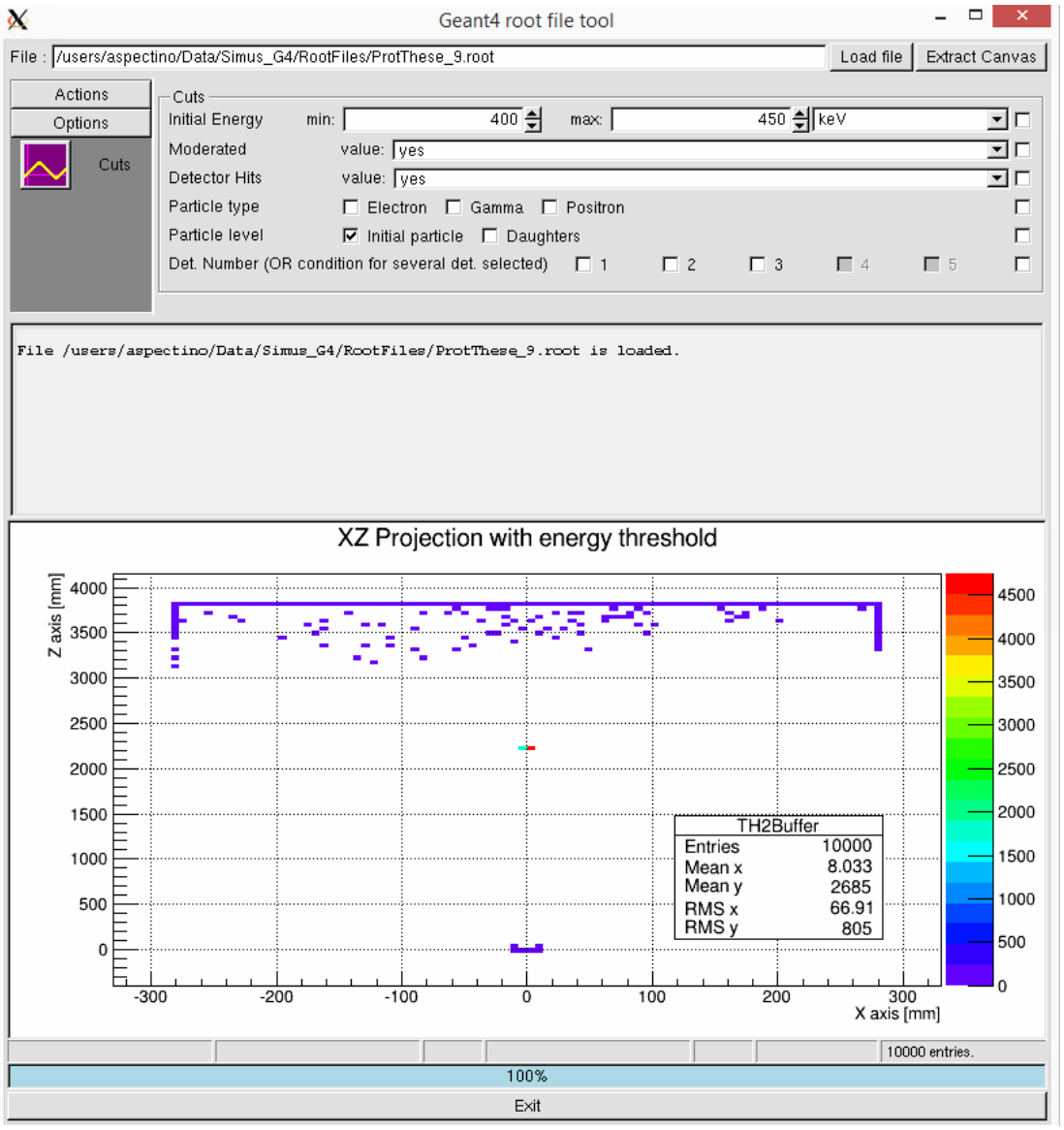

Figure 4.17. Screenshot of the data analysis tool developed to analyze the simulated data issued from Geant4 and the data issued from the detector of *a*SPECTino.

Chapter 5

The *a*SPECTino spectrometer

> Scientific apparatus offers a window to knowledge, but as they grow more elaborate, scientists spend ever more time washing the windows.
>
> *(Isaac Asimov)*

Contents

5.1. MAC-E filter concept 58
5.1.1. Particle transport in EM fields 59
5.1.2. Transmission function 62
5.2. Design and characteristics of the spectrometer 64
5.2.1. Vacuum chamber 64
5.2.2. Magnetic field 67
5.2.3. Electrostatic field 71
5.3. Detection system 72
5.3.1. Data acquisition system 74
5.3.2. Detector calibration 76

In order to develop and optimize the CALIPSO source, a test setup was required. The *a*SPECT spectrometer (see [ZBvdG+00, GBB+04] for detailed information on this apparatus) was initially supposed to serve for this purpose but it was moved to the Johannes Gutenberg-Universität in Mainz, Germany, and made unavailable at the very beginning of this project. As a result a complete new setup had to be designed and built, with the following requirements:

- **Detection of low-energy charged particles:** since this apparatus is a test setup for a low-energy calibration source of positively charged particles, it should be able to detect them.
- **Possibility to validate the source performance:** the central purpose of the positron source is to compare electrostatic potentials of electrodes,

as detailed in Section 1.1. The spectrometer shall allow to demonstrate this application and to measure the achievable resolution.

- **Similar experimental conditions as in proton spectroscopy experiments:** the CALIPSO source aims to characterize proton spectroscopy experiments and should therefore be able to operate in related experimental conditions. The test setup should have similar operating conditions, if possible. In our case typical proton spectroscopy experiments use a high magnetic field of several Teslas to confine protons in a High or Ultra-High Vacuum[1] (UHV) vessel. The use of supra-conducting coils, required to reach a high permanent magnetic field in a big volume, was both out of budget and schedule for this project. The choice was made to build an Ultra-High Vacuum vessel and to use a much lower magnetic field that could be created using resistive coils. This choice allows to completely confine low-energy positrons and to guide low-energy protons ($E_\mathrm{k} \leq 1$ keV) with a low radial momentum component (i.e., emitted almost parallel to the magnetic field lines).

- **High modularity:** it is important for this test setup to be easily tunable and to have many possible inputs/outputs so it can be well-adapted to the original design of the source but also to the possible extensions or modifications brought to it. Furthermore it should be easy to operate, like having the possibility to easily change the detector or intervene on the source itself with little downtime.

- **Low cost:** the initial project only included vacuum components and magnetic fields for simple tests and to couple an external proton source to *a*SPECT, but not a stand-alone spectrometer. An effort had to be made to keep the costs of the apparatus low in order to stay in budget.

A MAC-E filter spectrometer appeared to be the best choice as it allows to precisely select low-energy charged particles and, to some extent, to study their momentum, enabling a precise characterization of the calibration source. It is also a system that both my supervisor and I had experience with through our work in the *a*SPECT collaboration.

Consequently this concept was selected and the test setup was given the name *a*SPECTino[2]. This chapter describes its design and characteristics by first introducing the physical concepts used in the spectrometer and then describing the spectrometer itself as well as its detection system.

5.1. MAC-E filter concept

Through the clever use of electromagnetic fields, MAC-E filters can select low-energy charged particles with a sharp transmission function [BPT80]. They are

[1] Ultra High Vacuum defines pressures in the range of 10^{-7} mbar to 10^{-12} mbar. This corresponds to a density of respectively 2.65×10^9 to 2.65×10^4 molecules per cm^3.

[2] *a*SPECTino refers to "the little *a*SPECT" as its design is inspired by the retardation spectrometer *a*SPECT.

notably used to directly measure the electron-antineutrino rest mass in experiments such as KATRIN [Wei02] (so far only upper limits have been found [P+16]) and to determine the coefficient a describing the correlation between the electron and the antineutrino, such as in aSPECT [ZBvdG+00].

A negative magnetic gradient transfers the particles' kinetic energy into their longitudinal component (i.e., parallel to the magnetic field) and then a potential barrier, named the Analyzing Plane (AP), selects them: only particles with a high-enough longitudinal kinetic energy will pass through the filter. Particles are then focused with a strong magnetic field onto a detector set at high voltage so that the particles can be detected and overcome the strong magnetic field gradient. As only the selected particles are counted with the detector, the integrated spectrum can be measured by changing the selection potential.

In the aSPECTino spectrometer the calibration source is located in the source cross (see Figure 5.1) with a magnetic field of around 16 mT. Created low-energy particles, either positrons or protons, are then magnetically guided into the AP which is a low magnetic field region of 3.5 mT. A cylindrical electrode can be installed at the AP to create a selection potential. Particles that have passed through the AP are then accelerated by the detector High-Voltage (HV) potential which can be set down to -30 kV. They are then detected using a solid-state detector and the resulting signal is amplified and digitized by the acquisition system of the spectrometer. A complete description of aSPECTino can be found in Sections 5.2 and 5.3.

5.1.1. Particle transport in EM fields

The motion of charged particles in EM fields, and specifically electrons, has been studied in depth and is described in many textbooks, such as [Jac98, Rei08]. Only the important and relevant results and equations are detailed in this section. Furthermore, as this section concerns only low-energy particles ($E_\mathrm{k} \leq 1$ keV), relativistic corrections are not necessary and only a classical description is used.

5.1.1.1. Charged particles motion in an EM field

A charged particle in an electromagnetic field is subject to the Lorentz force

$$\mathbf{F} = q(\mathbf{E} + \mathbf{v} \times \mathbf{B}), \tag{5.1}$$

with $\mathbf{E}$ and $\mathbf{B}$ respectively the electric and magnetic field seen by the particle, q the electric charge of the particle and $\mathbf{v}$ its instantaneous velocity. In the presence of only a uniform magnetic field aligned with the z-axis, a moving charged particle will gyrate along the magnetic field line with a Larmor radius defined as

$$r_\mathrm{g} = \frac{m v_\perp}{|q| B}, \tag{5.2}$$

with m the mass of the particle, q its electric charge, $v_\perp$ the velocity component perpendicular to the magnetic field and B the magnetic field strength. The velocity component $v_\perp$ is related to the velocity by:

$$v^2 = v_\perp^2 + v_\parallel^2, \tag{5.3}$$

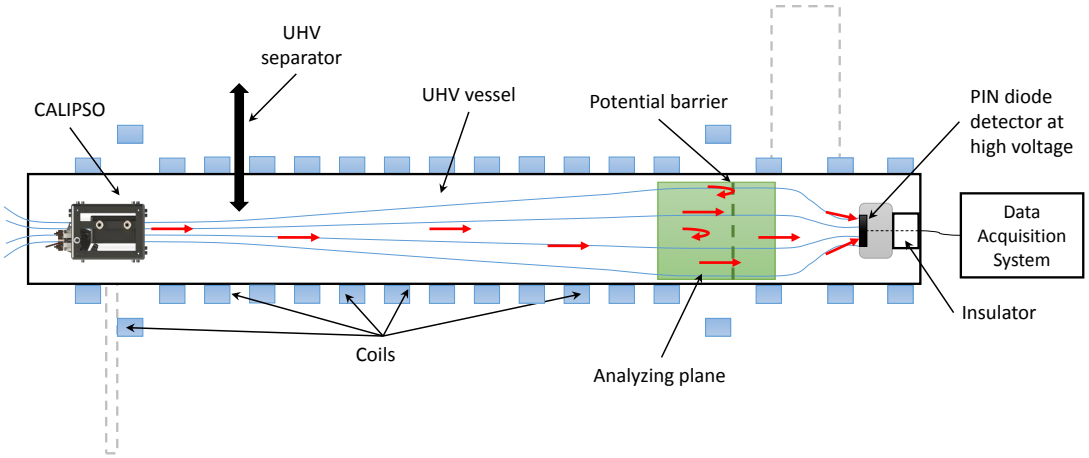

Figure 5.1. Design of the *a*SPECTino spectrometer. The UHV vessel can be separated in two volumes using the UHV separator. The CALIPSO source, located at the so called source cross, sits in a high magnetic field region (16 mT) and emits low-energy protons or positrons with an energy defined by its potential U_0. The charged particles are guided towards a low magnetic field region (3 mT) where the potential barrier of the Analyzing Plane will reflect those with an insufficient longitudinal kinetic energy. Transmitted particles are then focused by a strong magnetic field (16 mT) onto the detector which is at high voltage. This potential accelerates the charged particles to detectable energies and help them overcoming the magnetic mirror at the detector.

with $v_\parallel$ the velocity component parallel to the magnetic field. By defining θ as the angle of the particle momentum to the z-axis, one can decompose the particle's kinetic energy E_k into:

$$E_{\mathrm{k}\perp} = E_\mathrm{k} \sin^2\theta \quad \text{and} \tag{5.4}$$

$$E_{\mathrm{k}\parallel} = E_\mathrm{k} \cos^2\theta, \tag{5.5}$$

with $E_{\mathrm{k}\perp}$ and $E_{\mathrm{k}\parallel}$ respectively the perpendicular and longitudinal components of the particle's kinetic energy. Using Equations (5.3) and 5.4 one can re-write Equation (5.2) into:

$$r_\mathrm{g} = \frac{\sqrt{2mE_\mathrm{k}}|\sin\theta|}{|q|B}. \tag{5.6}$$

In the presence of both electric and magnetic uniform fields, Equation (5.1) leads to a helical movement of the particle with an additional drift. This behavior is usually used to induce a drift in the motion of a charged particle by having a uniform electric field transverse to the magnetic field, as shown in Figure 5.2. The drift is usually named $\mathbf{E} \times \mathbf{B}$ and its direction does not depend on the direction of the particle movement. Particles spending more time in the drift region are more deviated, meaning there is a momentum and energy dependency.

An $\mathbf{E} \times \mathbf{B}$ drift created by two electrodes is used in the CALIPSO source to extract low-energy positrons, as described in Section 6.1.2.2.

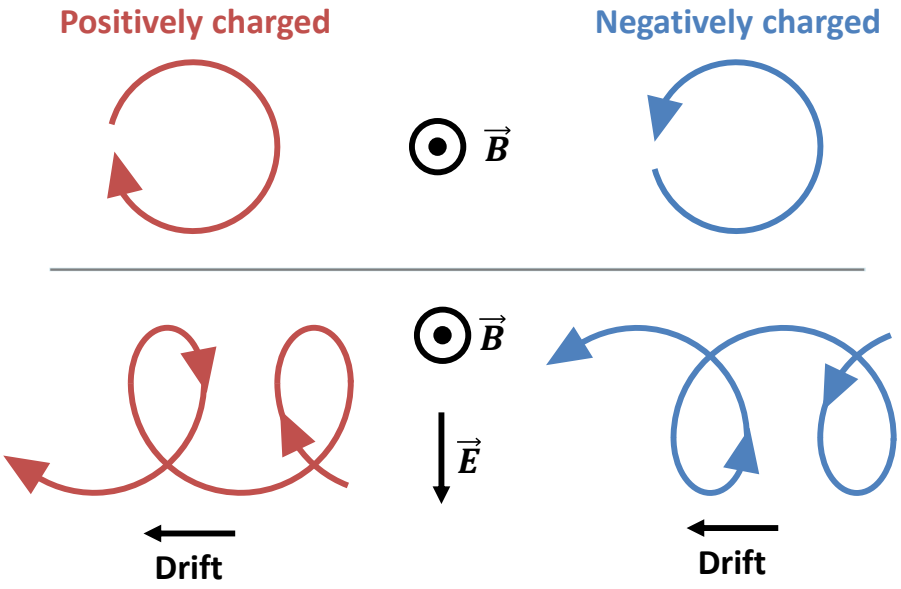

Figure 5.2. Scheme of positive and negative particles gyrating in a magnetic field only (respectively top left and top right) and the drifting motion induced by a transverse electric field (bottom left and right). The drift direction is the same for both charges and is only dependent of the electric field orientation compared to the magnetic field. Figure inspired from [Wik16].

5.1.1.2. Adiabatic invariants

The concept of adiabatic invariance arises from Hamiltonian systems with periodic motion. We define a Hamiltonian $H(q_i, p_i, t)$ with q_i and p_i respectively the generalized coordinates and the generalized momenta. With coordinates q_i being periodic, we can define the action integral J_i by [Rei08]:

$$J_i = \oint p_i dq_i. \tag{5.7}$$

If the system is evolving adiabatically (i.e., changes slowly over a period of q_i) then J_i is a constant of the motion. As a result each periodicity of the system implies an adiabatic invariant of the motion. In the case of an axially symmetric magnetic field with slow changes compared to a particle gyration (the periodicity associated with the symmetry), the magnetic moment

$$\mu = \frac{mv_\perp^2}{2B} = \text{const} \tag{5.8}$$

is an adiabatic invariant and therefore is constant. Equation (5.8) is equivalent to

$$\frac{p_\perp^2}{B} = \text{const.} \tag{5.9}$$

5.1.1.3. Magnetic mirror effect

In the case of adiabatic motion, Equation (5.9) implies that a particle experiencing a longitudinal magnetic field gradient will have its perpendicular momentum correspondingly modified, with $p_\perp(z) \propto \sqrt{B(z)}$. For instance by using Equations (5.3) and 5.9 we obtain:

$$v_\parallel^2(z) = v^2 - \frac{v_{\perp,0}^2}{B_0} \cdot B(z), \tag{5.10}$$

with $v_{\perp,0}$ and B_0 respectively the perpendicular velocity component and magnetic field at the charged particle emission point (i.e., when the particle leaves the calibration source). If the particle experiences a positive magnetic field gradient (i.e., moving into a higher magnetic field region) the longitudinal component of its velocity, $v_\parallel(z)$, will decrease and may become negative: in this case the particle is reflected by the magnetic field gradient, like a mirror. This effect is called the magnetic mirror effect and is used to create magnetic bottles that can confine charged particles.

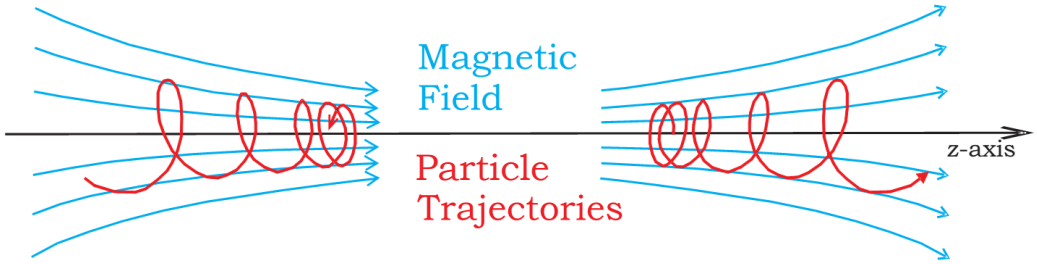

Figure 5.3. Illustration of the magnetic mirror effect (left) and the inverse magnetic mirror effect (right). Figure taken from [Sim10].

The opposite effect also exists when the particle is moving towards a lower magnetic field region. The longitudinal component $v_\parallel(z)$ will this time increase while the perpendicular component of its velocity, $v_\perp(z)$, will decrease: this is the inverse magnetic mirror effect. It is used in MAC-E filters to transfer the particle's kinetic energy into the component that the selection potential will be sensitive to. Figure 5.3 illustrates both of those effects.

5.1.2. Transmission function

In *a*SPECTino adiabatic conditions are fulfilled during the whole transport (i.e., $\Delta B/B \ll 1$ and $\Delta E/E \ll 1$ during one particle gyration) for low-energy positrons (up to a few hundreds eV) but not for low-energy protons. As shown in Equation (5.6) their larger mass implies a larger gyration radius at similar energies

and therefore imposes stronger requirements on field gradient. This section is therefore only dedicated to low-energy positrons in *a*SPECTino.

Using Equations (5.4) and 5.8 allow to rewrite the magnetic moment as:

$$\mu(z) = \frac{mv_{\perp}^2(z)}{2B(z)} = \frac{E_{\mathrm{k}\perp}(z)}{B(z)} = \frac{E_{\mathrm{k}}(z)\sin^2\theta(z)}{B(z)} = \text{const.} \tag{5.11}$$

As the positron magnetic moment is the same all over its trajectory, one can than write:

$$\mu(0) = \mu_0 = \frac{E_{\mathrm{k}}(0)\sin^2\theta(0)}{B(0)} = \mu_{\mathrm{AP}} = \frac{E_{\mathrm{k}}(\mathrm{AP})\sin^2\theta(\mathrm{AP})}{B(\mathrm{AP})}, \tag{5.12}$$

with 0 and AP denoting the two positions of interest, respectively the positron emission at the source and the positron selection in the analyzing plane. The 0 and AP indices stand respectively for $z = 0$ and $z = \mathrm{AP}$ and the z dependency for variables without indice will no longer be written to lighten the equations. Solving Equation (5.12) for $\sin^2\theta$ gives:

$$\sin^2\theta = \frac{B}{B_0}\frac{E_{\mathrm{k}0}}{E_{\mathrm{k}}}\sin^2\theta_0. \tag{5.13}$$

The longitudinal kinetic energy in the adiabatic approximation, noted $E_{\mathrm{k}_{\parallel}}^{\mathrm{ad}}$, can then, using Equations (5.5) and 5.13, be expressed as:

$$E_{\mathrm{k}_{\parallel}}^{\mathrm{ad}} = E_{\mathrm{k}} - \frac{B}{B_0}E_{\mathrm{k}0}\sin^2\theta_0. \tag{5.14}$$

As the total energy E is conserved in the system, we can express:

$$E = E_{\mathrm{k}} + E_{\mathrm{p}} = E_{\mathrm{k}} + eU, \tag{5.15}$$

with E_{p} the potential energy of the positron and U the electrostatic potential at a position z. We assume that the particle is emitted at $z = 0$ in U_0:

$$E_{\mathrm{k}} = E_{\mathrm{k}0} - e(U - U_0). \tag{5.16}$$

Equation (5.14) can then be re-expressed as:

$$E_{\mathrm{k}_{\parallel}}^{\mathrm{ad}} = E_{\mathrm{k}0} - e(U - U_0) - \frac{B}{B_0}E_{\mathrm{k}0}\sin^2\theta_0. \tag{5.17}$$

If $E_{\mathrm{k}_{\parallel}}^{\mathrm{ad}}$ becomes negative or null along the positron trajectory, it will not reach the detector. As a result the minimum initial kinetic energy $E_{\mathrm{k}_{\mathrm{Tr}}}$ required for the positron to overcome the potential barrier is:

$$E_{\mathrm{k}_{\mathrm{Tr}}} = \frac{e(U_{\mathrm{AP}} - U_0)}{1 - \frac{B_{\mathrm{AP}}}{B_0}\sin^2\theta_0}. \tag{5.18}$$

In the *a*SPECTino spectrometer the ratio between the magnetic field in the AP to the magnetic field in the region where positrons are emitted is $\frac{B_{\mathrm{AP}}}{B_0} = 0.223$ (more details in Section 5.2.2). Equation (5.18) therefore allows to determine if a positron will pass through the analyzing plane and be detected or not, based on its initial emission conditions.

5.2. Design and characteristics of the spectrometer

The spectrometer, shown in Figure 5.4, was built and used in the "*a*SPECT zone" of the Institut Laue-Langevin, in the neutron hall ILL7, close to the instrument IN16b. This experimental area and the reference frame of the *a*SPECTino spectrometer, which will be used for all matters related to the spectrometer in this work, are shown in Figure 5.5.

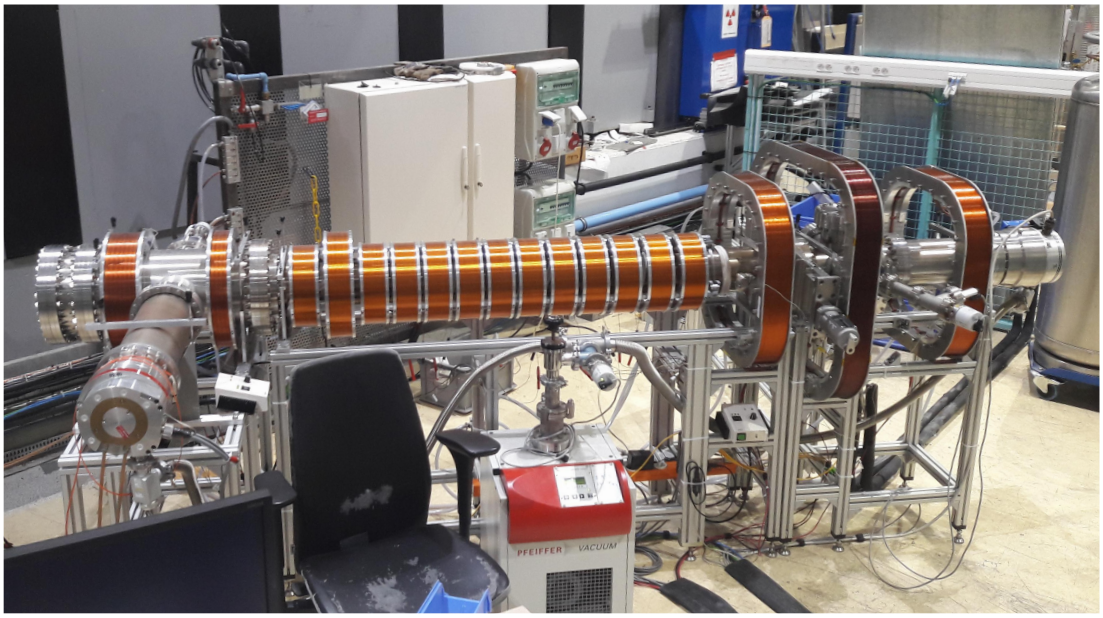

Figure 5.4. Photography of the *a*SPECTino spectrometer in its experimental area.

5.2.1. Vacuum chamber

The apparatus chamber was designed using commercially available 304L Stainless Steel tubes with Conflat (CF) flanges[3]. The source part can be separated from the spectrometer part by a gate valve, allowing manipulations of the source (e.g., crystal annealing, application of H_2 or O_2, access to the source) without venting or contaminating the full spectrometer. In order to reach a Ultra-High Vacuum, two CF160 turbo-molecular pumps (TMP) with pumping speeds of around 600 l/s are backed with a two stage (primary pump plus a small TMP) pumping station.

The geometry of the spectrometer was optimized to make the pumping as efficient as possible: the first TMP has a direct view on the main tube of the spectrometer and the second one is facing the big volume close to the detector, as described in Figure 5.6. Furthermore the two TMPs are far from the coils and are

[3]The CF standard uses knife-edge flanges and a metallic gasket, usually copper, that can be baked out up to 450 °C to create a Ultra-High Vacuum vessel.

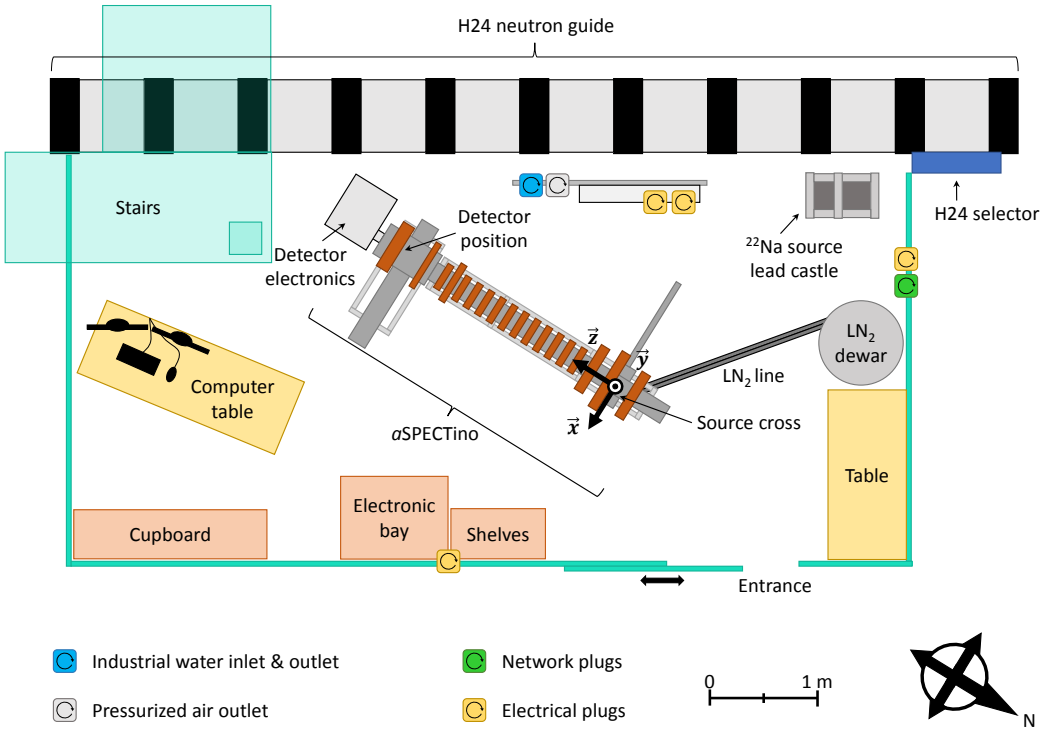

Figure 5.5. The experimental zone of the *a*SPECTino spectrometer is located near the H24 neutron guide. The 1 mCi ^{22}Na source required for CALIPSO (see Section 6.1.2.1 for more details) can be stored in the dedicated lead castle located in the corner of the area and described in Appendix C. The center of the right-handed frame used for the spectrometer, point (0,0,0), is located at the center of the source cross with the z-axis going through the center of the main long tube of the spectrometer, pointing toward the detector. The y-axis is vertical and points toward the sky.

in a low magnetic field region to prevent high eddy currents[4]. Once the apparatus is closed, a leak test can be performed using an He spectrometer, with a typical leak rate background between 4×10^{-10} mbar L s^{-1} and 1×10^{-9} mbar L s^{-1} for the *a*SPECTino spectrometer under normal conditions.

Pressure is sensed at three key locations (see Figure 5.6): close to the source, close to the detector and at the TMPs backing line. Three sensor technologies are used: Pirani gauge, hot cathode and cold cathode. Pirani gauges use the pressure dependent thermal conductivity of gases to measure the pressure in the range of 5×10^{-4} mbar to 1000 mbar whereas hot and cold cathodes use rest gas ionization

[4]Eddy currents induce heat on the rotor of TMPs. Rotors are conductive and turning at high frequency, typically 800 Hz for the ones of *a*SPECTino. If they are sitting in a magnetic field, electrical current loops will be induced in the rotor, opposing its rotation. The resulting increased power consumption will heat the rotor and can damage it. This effect is particularly important when the TMP is mounted perpendicular to the magnetic field. In such configuration, the magnetic field should not exceed a few mT at the TMP [W+11].

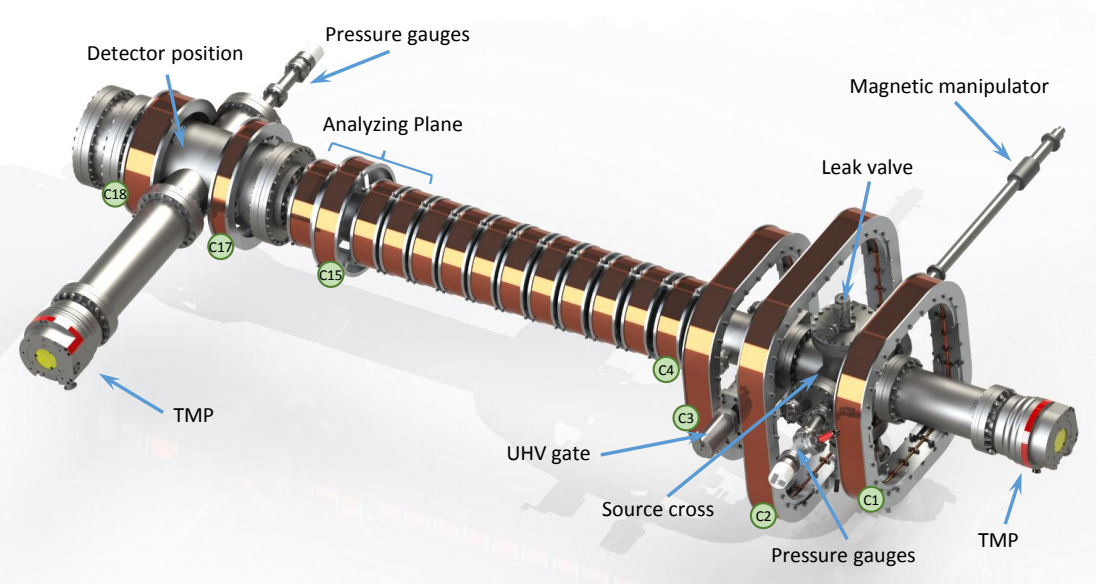

Figure 5.6. Scheme of the *a*SPECTino spectrometer. Coils are indexed from C1 to C18 (as detailed in Section 5.2.2). The UHV gate can isolate the two parts of the spectrometer (i.e., the source part and the detector part) and each part is equipped with a TMP and a set of pressure gauges. More details on the source cross and its equipments are presented in Figure 6.3.

to measure the pressure from respectively 5×10^{-10} mbar and 5×10^{-11} mbar to 0.01 mbar (values for the models used in *a*SPECTino). The pressure sensor at the TMPs backing line is a full range combo composed of a Pirani sensor and a hot cathode. The other two sets of pressure sensors are composed of two distinct apparatuses: a Pirani gauge and a cold cathode, resulting in a total of five pressure sensors for *a*SPECTino. Both cold cathodes and hot cathodes use an inverted magnetron design with strong permanent magnets. For this reason all the non-Pirani sensors are set far away from the coils and the central tubing of the spectrometer.

5.2.1.1. Baking of the vacuum vessel

In order to reach the UHV regime, the whole spectrometer can be baked up to 150 °C[5] to increase the out-gassing rate, actively releasing trapped gases (mainly N_2 and H_2O) from the materials. This process is required in order to achieve pressures lower than 10^{-8} mbar in a reasonable time. Four heating bands of 1450 W, driven by two temperature-controlled power supply units, are used to heat *a*SPECTino.

The typical bake-out routine is to heat the apparatus which is already in the HV

[5]The higher the bake-out temperature, the more efficient this procedure is. Several parts of the spectrometer limit the maximum bake-out temperature, such as the detector and some feedthroughs.

range until the new, higher pressure is stable: for *a*SPECTino this needs several days (between two and four). Then the heating is stopped and the pressure can go down by around two orders of magnitude. In the *a*SPECTino spectrometer with the full detector mechanics (except the detector itself) and no CALIPSO source the typical pressures are in the level of 7×10^{-10} mbar at the detector cross gauge and 1×10^{-9} mbar at the source cross.

5.2.2. Magnetic field

5.2.2.1. Simulations and design

The magnetic field of the spectrometer was designed using RADIA (see Section 4.2.2) and optimized by studying the positron transport along *a*SPECTino in simulations (see Chapter 4). Several configurations were tested with the following constraints:

- a reasonable size (and price) for the whole apparatus
- no in-vacuum coils
- a strong field and a large homogeneous field region at the source location
- a weak field and a large homogeneous field region at the analyzing plane region
- a strong field at the detector position
- $\Delta B/B \ll 1$ during one particle gyration for positrons (see Section 5.1.1.2)

In order to fulfill these conditions, two Maxwell coils were introduced in the simulation, respectively at the source location and at the analyzing plane. A Maxwell coil, described in Figure 5.7, consists of three coils that provide a field with better homogeneity than Helmholtz coils. Because the *a*SPECTino coil system is complex and longitudinally asymmetric, the current-density and the positioning of the Maxwell coils were slightly modified from the theoretical values. Furthermore a small gradient was introduced at the source position in order to avoid any undesired reflection due to a magnetic mirror effect on freshly born low-energy protons or positrons.

The final design consists of 12 coils and two sets of Maxwell coils, resulting in a total of 18 resistive coils (see Figure 5.6). The simulated magnetic field in the center of the bore tube is shown in Figure 5.8. Furthermore Figure 5.9 represents the Larmor radius of positrons as a function of their energy for several magnetic field strengths encountered in the *a*SPECTino spectrometer (i.e., from 3.5 to 16 mT).

The Earth magnetic field values in the experimental area, taken from the WMM[6] model, are detailed in Table 5.1. As seen in Figure 5.5 the North component of the magnetic field X_g is roughly parallel to the spectrometer z axis and will not strongly impact the spectrometer behavior. The two other Earth

[6]The World Magnetic Model describes the slow-varying magnetic field component of the Earth. It is developed by the United States National Geospatial-Intelligence Agency (NGA) and the United Kingdom's Defence Geographic Centre (DGC). As the Earth magnetic field is constantly changing, models describing it are regularly updated, like the WMM every five years. More information can be found in [fEI17].

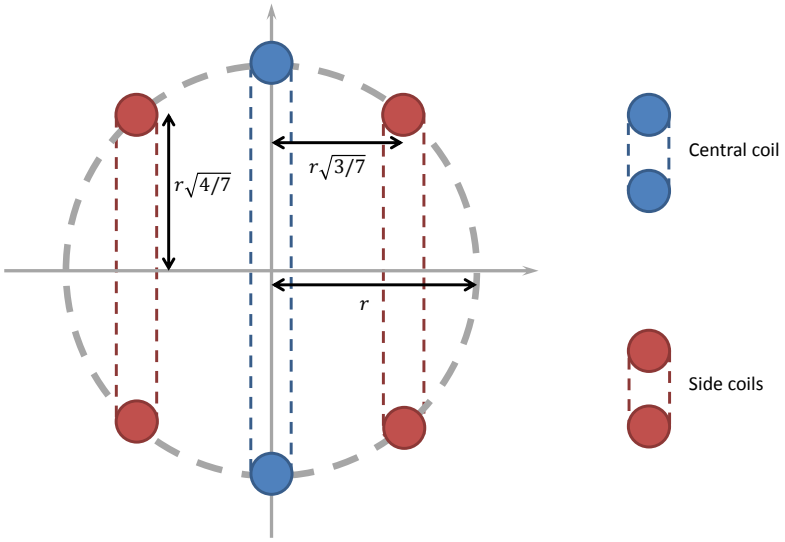

Figure 5.7. A Maxwell coil is composed of three coils which are standing at the surface of a virtual sphere of radius r. The side coils must have a number of ampere-turn equal to 49/64 of the ampere-turn of the central coil to create a highly uniform magnetic field [Gar67].

magnetic field components induce a shift in the low-energy positrons trajectory of around -3.5 mm in the x direction and -16 mm in the y direction at the detector position of the spectrometer when using the standard magnetic field configuration. The *a*SPECTino detector center being fixed at $x = y = 0$, those shifts can be compensated easily by simply adjusting the emission position of the positrons. The *a*SPECTino spectrometer was built without the use of magnetic materials.

Table 5.1. Earth magnetic field values for January the 1, 2017. X_g, Y_g and Z_g are respectively the geographical north (positive northward), east (positive eastward) and vertical (positive downward) components of the magnetic field vector. The earth magnetic field total intensity from this dataset is $F = 47083$ nT.

	Component i		
	X_g	Y_g	Z_g
B_i (nT)	22 773	610	41 194
ΔB_i (nT)	138	89	165
$\mathrm{d}B_i/\mathrm{d}t$ (nT/year)	16	48	21

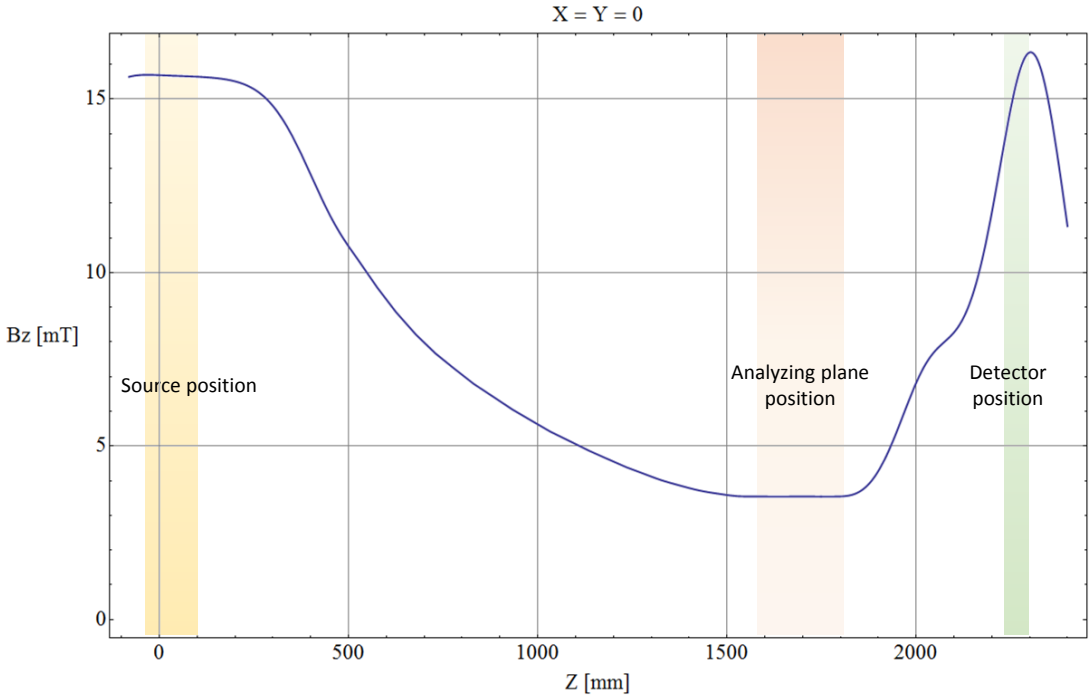

Figure 5.8. RADIA simulation of the magnetic field along the *a*SPECTino spectrometer. The calibration source is located at the source position where a field with a small gradient (around 500 µT m^{-1}) is created by the first set of Maxwell coils.

5.2.2.2. Coils production and characteristics

The aluminum mechanical structures of the coils were designed under SolidWorks and then produced in-house for coils C1 to C3 and at an outside company for coils C4 to C18. The small coils (C4 to C18) were self-winded using a lathe in the Atelier Libre-Service of the ILL, whereas coils C1 to C3 required a manual (but still motor-assisted) winding as they couldn't fit in the lathe. All coils properties are detailed in Table 5.2.

Because of their high power, coils C1, C2, C3 and C18 require dedicated cooling. For C1, C2 and C3 it is provided by a copper tube supplied with industrial water in the center of each big coil structure, keeping the maximum operating temperature at a reasonable level (less than 90 °C at equilibrium at nominal power). Coil C18 requires a smaller current and is therefore only cooled by three 120 mm fans which are blowing ambient air from the bottom of the coil.

The insulated copper wire can withstand up to 180 °C and this temperature could be easily achieved at nominal power in case of cooling failure. In order to avoid any damage to the coils the Power Supply Units (PSUs) have a voltage threshold limit that shuts down the PSU if the voltage exceeds a define value. As conductivity is a function of the material temperature, if a coil becomes hotter, its resistivity will increase and so the output voltage of the PSU (in current regulation mode). Furthermore a type-K thermocouple was inserted, during the winding,

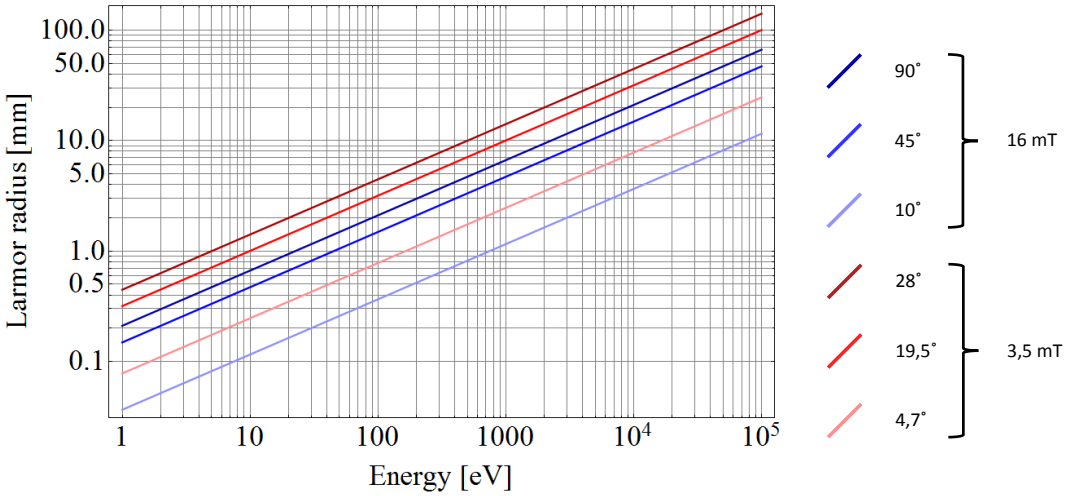

Figure 5.9. Plot of the positron Larmor radius at the source emission position (red) and at the analyzing plane (blue) for different emission angles compared to the magnetic field. The emission angle at the AP is derived from the initial emission angle with Equation (5.13). For instance a positron with an initial emission angle of 90° will have its momentum forming an angle of only 28° once in the AP because of the inverse magnetic mirror effect, as detailed in Section 5.1.

in the center of coils C1, C2, C3 and C18 to directly measure the temperature in the hottest place of those coils. Pictures of details of some of those coils are shown in Figure 5.10.

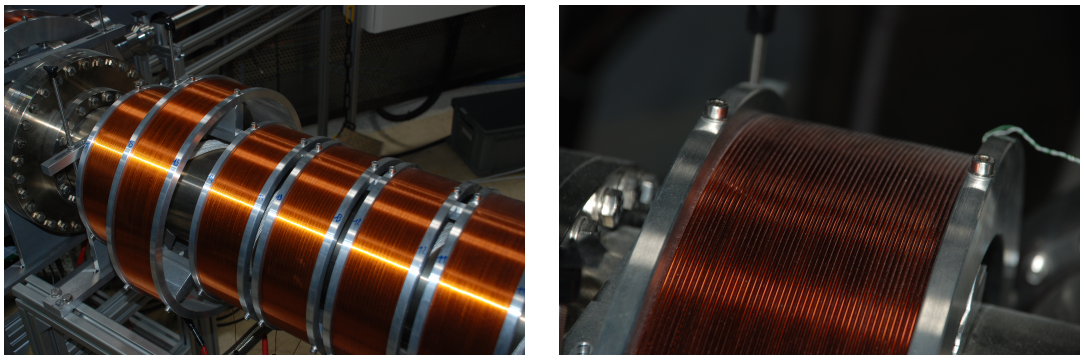

(a) (b)

Figure 5.10. (a): Detail of the small coils and the Maxwell coil of the Analyzing plane. (b): Zoom on the surface of coil C18 (the coil closest to the detector). The wire of the type-K thermocouple installed in the center of the coil is visible on the right.

Table 5.2. Characteristics of the coils of the *a*SPECTino spectrometer and current configuration corresponding to the magnetic field simulation shown in Figure 5.8.

	⌀ or		Total nb. of			Electrical properties			
Coil name	width (mm)	Cu wire ⌀ (mm)	Layers	Turns	Z pos. (mm)	R (Ω)	Current (A)	Power (W)	Cooling
C1	412	2.0	16	648	-180	6.8	6.588	295.7	Water
C2	756	2.5	14	441	92	4.0	12.155	597.3	Water
C3	412	2.0	16	648	335	6.8	5.525	207.9	Water
C4	246	1.0	6	375	545	6.6	0.893	5.2	-
C5	246	1.0	6	375	655	6.6	1.054	7.3	-
C6	246	1.0	6	375	763	6.6	1.131	8.4	-
C7	246	1.0	6	375	869	6.6	1.080	7.7	-
C8	246	1.0	6	375	972	6.6	1.003	6.6	-
C9	246	1.0	6	375	1075	6.6	0.918	5.5	-
C10	246	1.0	6	375	1175	6.6	0.825	4.5	-
C11	246	1.0	6	375	1275	6.6	0.748	3.7	-
C12	246	1.0	6	375	1375	6.6	0.672	3.0	-
C13	246	1.0	6	375	1475	6.6	0.612	2.5	-
C14	246	1.0	6	375	1575	6.6	0.490	1.6	-
C15	326	1.0	6	375	1682	8.6	1.076	10.0	-
C16	246	1.0	6	375	1788	6.6	0.416	1.1	-
C17	316	2.0	14	329	2031	2.1	3.902	31.3	-
C18	316	2.0	14	595	2307	3.7	7.310	198.6	Air

For coils C1, C2, C3, C17 and C18, the current is provided using commercial PSUs from Elektro-Automatik whereas a self-made 16 channels current supply unit, controlled by a computer, provides the current for coils C4 to C16. More information about this PSU is given in appendix B.

5.2.3. Electrostatic field

5.2.3.1. Selection electrode

The selection electrode of *a*SPECTino, shown in Figure 5.11a, is held and isolated from the bore tube by a small aluminum support coupled with ceramic insulators. This design allows to install several electrodes in the main tube of the spectrometer. As a result transition electrodes can be installed if necessary.

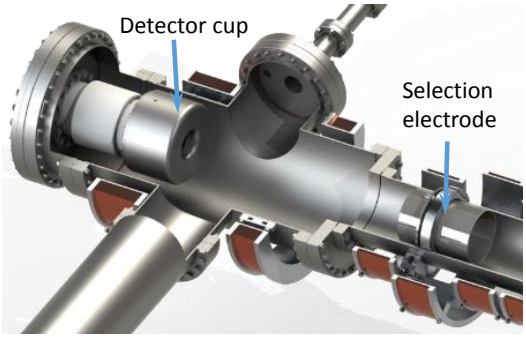

(a)

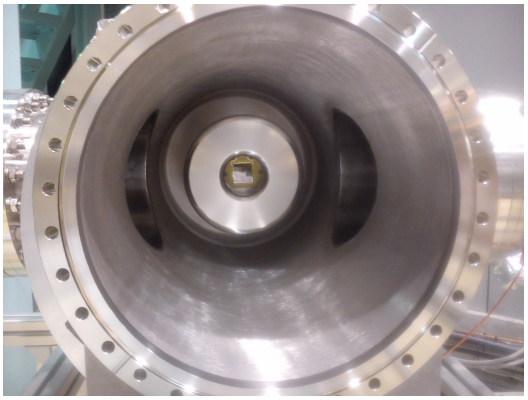

(b)

Figure 5.11. (a): View of the inside of the detector part of *a*SPECTino, with the selection electrode at the AP on the right and the detector mechanics (i.e., insulation ceramic, feed-through, detector and detector cup) on the left. (b): Picture of the detector cup with a silicon detector in its center, viewed from the AP position.

5.2.3.2. Detector cup

The detector cup, shown in Figure 5.11, is a stainless steel electrode that softens the electrostatic field at the detector surroundings, reducing discharges due to the high voltage. The detector cup design was directly inspired by the one of the *a*SPECT apparatus (see [Kon11]) and was produced in-house. The four screws holding the detector cup were filed down to remove sharp edges as much as possible. The high-voltage was tested down to −35 kV, with several discharges during the slow commissioning ramp-up. As the whole mechanical setup was brand new, small metallic imperfections or residuals may have created local high electric fields, causing the discharges. Once at −35 kV, the setup ran for approximately 20 hours without trouble and the following ramp-ups to a maximum of −23 kV did not trigger any discharges.

5.3. Detection system

As shown in Figure 5.12 the detector is mounted on a DN100CF flange at the end of a long ceramic break that can support a potential difference of up to 60 kV. The detector high-voltage is created by a low-current high-voltage power supply applied to the secondary circuit of an insulating transformer. The latter allows to decouple the detector circuit from the standard 230 V AC power: the insulating transformer reproduces the 230 V AC with a reference potential set by the HV power supply. All the high-voltage system is located in a plexiglass box at the back of the spectrometer and connected only to the detector and the detector cup. It is vented by two fans located at the bottom and top of the box, creating a flow of fresh air to cool the electronics.

An aluminum tube surrounded by a 2 mm thick plexiglass tube is inserted inside the ceramic break, up to the detector flange. This two-layer tube ensures

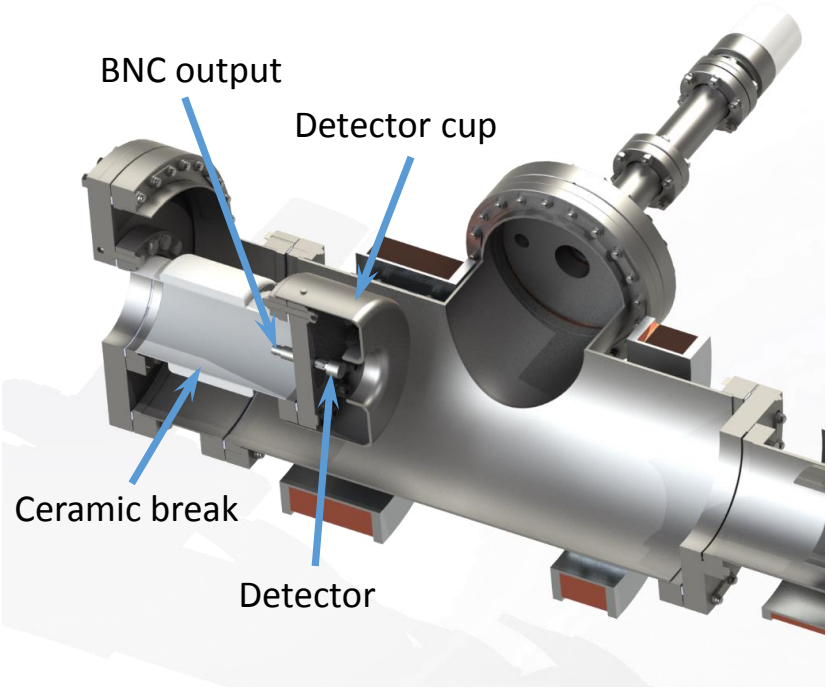

Figure 5.12. Setup for the detector of *a*SPECTino. The solid-state detector, protected from direct discharges by the detector cup, is located at the center (i.e., $x = y = 0$) of the spectrometer axis. The large ceramic break of around 100 mm diameter is mounted reversely (ambient pressure is inside the ceramic break) and isolates the spectrometer from the detector potential.

the proper connection between the detector feedthrough and the plexiglass box and the insulation between the detector HV and the spectrometer.

It is possible to mount different kinds of solid-state detectors on *a*SPECTino, as the DN100CF feedthrough flange can be changed without too much efforts. The modification of the detector flange and the detector itself takes around two to three hours, but a few days are required in order to vent, re-pump and bake out the relevant part of the spectrometer.

The default setup of the *a*SPECTino detection system consists of a partially depleted PIN diode[7] from CANBERRA, held at room temperature. This silicon detector has a thin Al entrance window of less than 50 nm, with a circular active surface of 50 mm^2 ($\varnothing = 8$ mm) and 100 µm depth, resulting in a detector capacitance of around 100 pF[8]. The thin entrance window is essential for detection of low-energy protons and positrons as it ensures that they can reach the depleted region of the silicon detector. On the other hand a thin depleted region offers

[7] A PIN diode is composed of three layers: a p-type and a n-type semiconductor and an intrinsic region in-between.

[8] The capacitance of the detector, and more generally the detection system (i.e., the detector and the line up to the first amplification stage), strongly impacts the signal to noise ratio. In regular solid-state detectors the capacitance is related to the detector size: the smaller the detector the lower the noise and the thinner the detector the higher the noise.

a lower sensitivity to gammas (i.e., background). It is certified with a 4.6 keV FWHM resolution at 300 K and is running with a positive bias of 60 V provided by a low-noise power supply. This detector was used in the TRINE experiment to detect low-energy protons [SBP+04]. A 1/4-32 (UNF) Microdot connector is supplied at the back of the detector and it is directly connected to the 10-32 (UNF) Microdot to BNC feed-through of the flange, using a vented connector made in-house, as those are not commercially available.

5.3.1. Data acquisition system

5.3.1.1. Preamplifier and Amplifier

As the ceramic break supporting the detector is very large (internal diameter of 100 mm), the first stage of electronics can be put right behind the detector, inside the ceramic break itself. An ORTEC 142A charge-sensitive preamplifier is connected to the detector using a RG-62/U coaxial cable[9] of 15 cm length, adding only 7 pF to the system capacitance. The pre-amplifier converts the current collected from the detector into a voltage output proportional to the integrated input current: an example is shown in Figure 5.13.

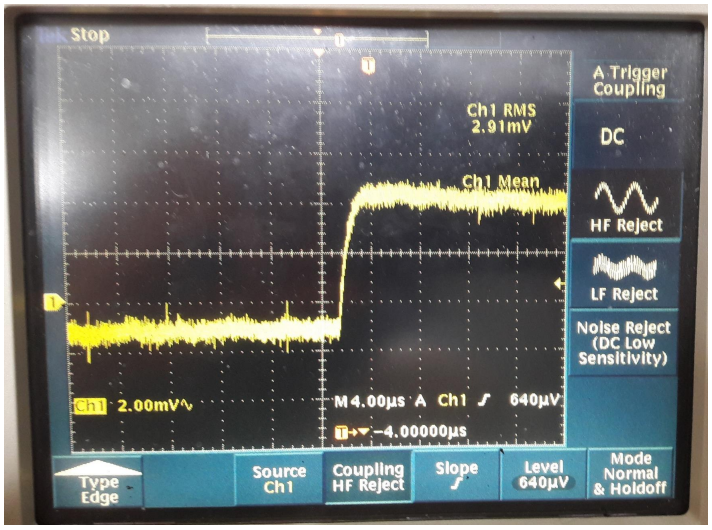

Figure 5.13. Example of an output signal from the ORTEC 142A preamplifier using a scope. The signal is decomposed into two parts: first a fast rising signal and then a slow exponential decay.

The signal from the ORTEC 142A is sent to an ORTEC 570 amplifier which filters and transforms the signal into a fast pulse. Shaping time constant can be selected on the amplifier, from 0.5 µs to 10 µs. A shaping time of 2 µs offers a good compromise between energy resolution and dead-time of the system for the expected count rate (a few kHz maximum). The height of the shaped pulse is directly proportional to the energy deposited in the detector. Non-linear effects

[9] RG-62/U cables have the same 93 Ω impedance as the preamplifier input and a low capacitance value per meter.

can be neglected as the precise energy spectrum is not very important after the acceleration is of lesser importance.

A big effort was made to reduce the noise along all the steps of the signal chain. Many different configurations were tested and the best performance was obtained by connecting the Al tube inside the ceramic break directly to the pre-amplifier mass and then to double shield the coaxial cable running to the amplifier using a copper braid. Finally a low-pass filter was also installed in-between the pre-amplifier and the amplifier.

5.3.1.2. Analog to Digital Converter (ADC)

The signal issued from the amplifier is then treated by the ADC which is a 14-bit 100 MHz CAEN[10] V1724 flash ADC[11] card with a $-2.25\,\mathrm{V}$ to $2.25\,\mathrm{V}$ input range. It is a VME card that should be used inside a VME crate, but the plexiglass box for the detector electronics is too small for it. The solution was to create a dedicated box, shown in Figure 5.14, containing the card and providing all the required voltages. The ADC can then be fully controlled using the integrated optical link, outside of a VME crate. The optical link is compatible with operating the card at high voltage and the control unit at ground.

Figure 5.14. The V1724 ADC card in its dedicated box. This VME card can be controlled using only its optical link (front connector) but requires an external power supply and all its VME flags need to be set at their ground level. This is done through the use of a specifically built power supply. Both the ADC box and its power supply are cooled by several fans and are installed in the plexiglass box regrouping all the detector electronics sitting at HV.

[10] **C**ostruzioni **A**pparecchiature **E**lettroniche **N**ucleari. This industrial spin off of the Italian Nuclear Physics Research is specialized in "the design, the production and the supply of electronic instrumentation for radiation and low light sensors".

[11] A flash ADC compares the input voltage with a certain number of reference voltages. All those comparisons are made at the same time, in parallel, resulting in a very high sampling rate. However the better the resolution the more comparators are needed: $2^n - 1$ for a n-bit conversion.

The analog data coming from the amplifier is continuously digitized and the high sampling rate results in a high flow of data, of more than 140 MB/s. A trigger condition is therefore applied at the V1724 card: a RC^2 filter is used to detect events. If the trigger condition is fulfilled the event (the waveform, timestamp, channel ID etc.) is saved in a buffer.

Once the buffer of the card is full (128 events), it is flushed and transferred to the computer through a two step process. First the data is sent, through optical fibers, to a first VME card sitting in the VME crate of the electronic bay. Afterwards the data is transferred to the computer via the optical link, where it is saved into a list mode file and finally convert into a ROOT file for further analysis, as described in Section 4.4.

5.3.2. Detector calibration

The PIN diode detector of *a*SPECTino was calibrated using a sealed ^{133}Ba source which decays by electron capture with a half-life $\tau = 10.51$ y [KRK11]:

$$^{133}\mathrm{Ba} + e^- \rightarrow {}^{133}\mathrm{Cs} + \nu_e + 517.4 \text{ keV}. \tag{5.19}$$

As the source is sealed in several millimeters of plastic, only photons are coming out of it. The small detector depleted region depth makes it sensitive to low-energy photons only (both hard X-rays and soft gamma rays). As shown in Table 5.3 such a source is well adapted for the calibration of solid-state detectors at low energy as there are several transitions between 30 and 80 keV.

Table 5.3. List of hard X-rays (left) and soft gamma-rays (right) issued from ^{133}Ba decay. Values taken from [KRK11].

X-rays			Gamma rays	
E (keV)	I (%)	Assignment	E_γ (keV)	I_γ (%)
30.625	33.9	Cs K_{α_2}	53.162	2.14 (3)
30.973	62.2	Cs K_{α_1}	79.614	2.65 (5)
34.920	5.88	Cs K_{β_3}	80.998	32.9 (3)
34.987	11.6	Cs K_{β_1}		

The low activity of the calibration source (around 5 kBq) imposed a small distance to the detector in order to acquire data in a reasonable time scale. As a result the sealed source was installed in an aluminum support fixed at the end of a magnetic manipulator installed next to the detector specifically for this calibration. The source could then be positioned at approximately 10 cm in front of the detector or moved away to acquire background spectra.

A Geant4 simulation was performed to check the consistency of the measurement and validate the identification of the energy peaks. In order to consider the detector resolution, a noise similar to the one specified on the detector datasheet (i.e., 4.6 keV at room temperature) was introduced in a post-treatment of the

data using the data analysis software detailed in Section 4.4.2. The simulated spectrum is shown in Figure 5.15.

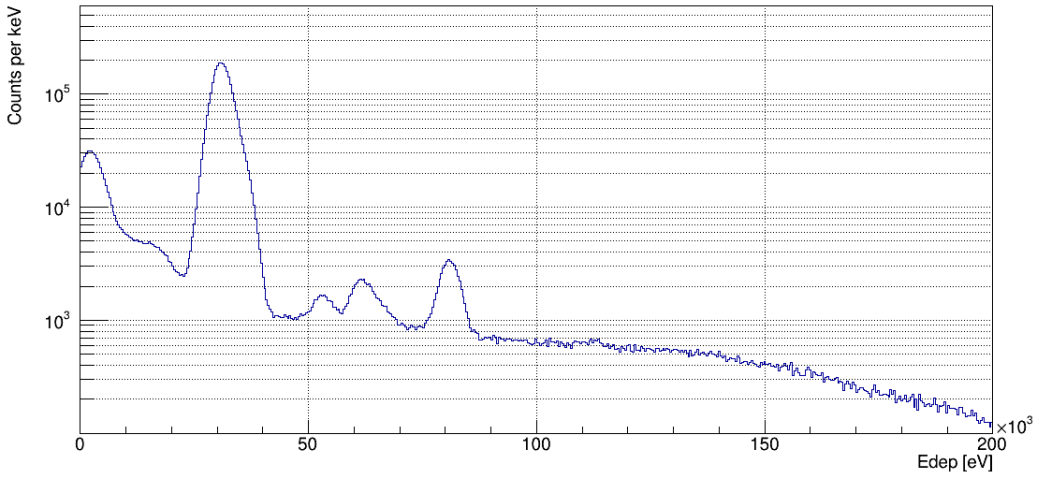

Figure 5.15. Simulated spectrum of the deposited energy in the *a*SPECTino PIN diode with a ^{133}Ba sealed source. A noise issued from a Gaussian distribution of 4.6 keV FWHM was folded in to simulate the detector noise.

Several datasets were acquired with different signal cable setups in order to find the configuration with the lowest noise (more details in Section 5.3.1). The ^{133}Ba spectrum issued from those tests is shown in Figure 5.16. Finally a background measurement performed under the same conditions is shown in Figure 5.17 along with simulated spectrum of low-energy protons and positrons hitting the *a*SPECTino detector set at a $-25\,\mathrm{kV}$ potential.

Comparison of the simulated and the measured spectrum shows a good agreement the electronic noise region, with the exception of the shoulder at about 22 keV in the measured spectrum (Figure 5.16). After investigation, this shoulder is most likely related to Ag X-rays issued from the screws around the detector, inside the detector cup. Those screws are coated with Ag in order to avoid galling[12] as this problem arose when changing the detector feedthrough flange. The Ag $K_{\alpha 2}$ and $K_{\alpha 1}$ energies are respectively of 21.99 keV and 22.163 keV [Bla08].

The calibration formula for the PIN diode detector derived from the measured spectra and the simulation is:

$$E_{\mathrm{dep}} = 0.027 \times \mathrm{ch}_{\mathrm{ADC}} + 0.318, \tag{5.20}$$

with E_{dep} the deposited energy in the detector, in keV and $\mathrm{ch}_{\mathrm{ADC}}$ the channel number of the Analog-to-Digital Converter (ADC) system.

Using Equation (5.20) and Figure 5.17 we can see that the electronic noise of the detection system does not exceed 10 keV when the detection system is

[12] The term galling refers to the cold welding of two surfaces, typically stainless steel nuts and bolts. For instance, screwing a threaded bolt without any lubricant can remove the protective oxide layer and expose bare reactive surfaces, leading to the complete freezing of the thread.

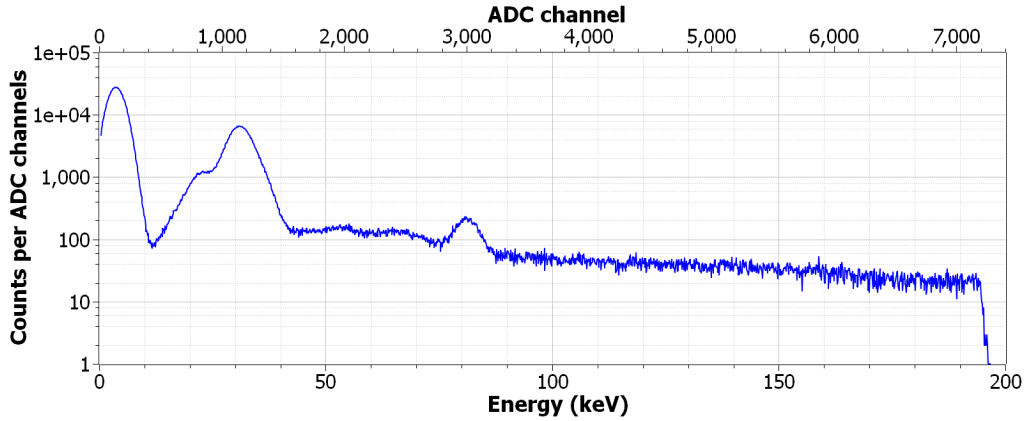

Figure 5.16. ^{133}Ba spectrum issued from a 10 hours data acquisition with the *a*SPECTino detection system at ground. The ^{133}Ba sealed source was directly in front of the detector at a distance of around 10 cm. Equation (5.20) was used for the energy calibration.

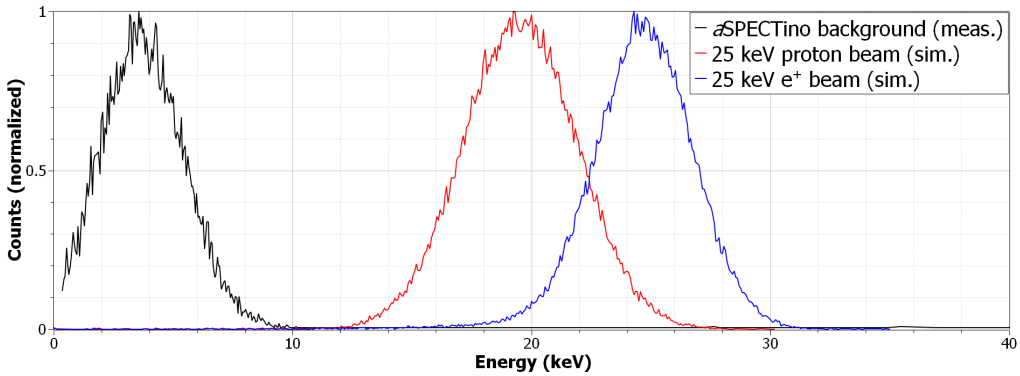

Figure 5.17. Background measurement (black) issued from a 15 minutes data acquisition in similar conditions as in Figure 5.16. During the measurement the ^{133}Ba source was moved away from the detector, at around 30 cm on its side. The background is strongly dominated by the electronic noise of the detection system and limited to the 0 to 10 keV range. Simulations of low-energy protons (red) and positrons (blue) accelerated onto the *a*SPECTino detector set at $-25\,\mathrm{kV}$ show a significant difference between the energy deposited in the dead layer of the detector for the two kind of particles. In both cases a detector potential of $-25\,\mathrm{kV}$ allows to separate the signal from the background. The counts are normalized to fit with the background and correspond to a count rate of around 110 particles per second for each run.

held at ground. Setting the detection system at high-voltage introduces a new contribution to the electronic noise of the setup (i.e., the noise of the HV power

supply) and increases the noise upper limit by about 20%. Therefore the system should be operated with a detector potential between -20 kV and -25 kV in order to obtain a signal issued from proton or positron detection that is well separated from the electronic noise.

Conclusion

This chapter detailed the design and characteristics of the *a*SPECTino spectrometer. It offers a practical setup that can detect low-energy charged particles and offer the possibility to easily intervene on the CALIPSO source installed inside. It also reproduces, with the exception of the lower magnetic field, typical experimental conditions encountered in proton spectroscopy experiments. It has been demonstrated experimentally that an acceleration voltage of -25 kV is sufficient for the detection of positrons and protons and that the setup is stable for up to -35 kV.

Chapter 6

The CALIPSO source

> The true delight is in the finding out rather than in the knowing.
>
> *(Isaac Asimov)*

Contents

6.1. Design of the apparatus 82
6.1.1. Gas inlet 85
6.1.2. Moderated positron source 86
6.1.3. Proton source 90
6.2. Crystal holder 92
6.2.1. Cold source 92
6.2.2. Crystal block 93
6.2.3. Piezo motor 95

CALIPSO stands for both CALIbration Positron SOurce and CALIbration Proton SOurce. At the beginning of this project, the plan was to create two distinct apparatuses: one for the moderated positron source and one for the low-energy proton source. However it turned out that the optimum design for both those sources required several similar key-features:

- A tungsten (110) crystal,
- Cooling of the crystal down to cryogenic temperatures,
- Cleaning of the crystal surface by annealing.

As a result I decided to create a single apparatus that would allow to produce both moderated positrons and low-energy protons, but not at the same time. The most important element of the CALIPSO system is the tungsten (110) crystal. Two high-purity (99.999%) tungsten (110) of 9 mm diameter and 1 mm thickness were ordered to be used in CALIPSO. They are polished with a roughness inferior to 0.01 μm and their orientation accuracy is lower than 1 degree. For all the preliminary tests, simple polycrystalline tungsten disks of the same dimensions are used in order to preserve the high-quality crystals. The concept of the source, based on the methods described in Chapters 2 and 3, is to either:

- Bombard the clean and cool crystal with positrons issued from a radioactive β^+ source to create a beam of low-energy moderated positrons.
- Deposit a mono-layer of hydrogen on the clean and cool crystal and then bombard it with low-energy electrons to create a beam of low-energy protons by ESD.

In both configurations the crystal first needs to be cleaned by annealing it inside the spectrometer vacuum. The cleaning procedure, described in Section 7.1.2, requires the heating of the crystal to high temperatures (up to 1900 °C). A complex crystal holder, detailed in Section 6.2, was therefore designed to perform adequate heating and cooling of the crystal and operation of the source for both its configurations.

In the positron configuration, moderated positrons should be separated from primary and, as soon as possible, from scattered positrons in order to maximize the signal-to-background ratio. This is achieved by an $\mathbf{E} \times \mathbf{B}$ separator which is used to vertically shift the beam of moderated positrons[1]. Undrifted positrons cannot leave CALIPSO via the output aperture. Only low-energy particles are extracted from the outer box of the CALIPSO source.

All the components of the source have a low outgassing rate (i.e., UHV compatibility) and a low magnetic susceptibility, except for the very thin (0.16 mm diameter) type-K thermocouple used at the back of the source, which is magnetic. CALIPSO parts are made of stainless steel (304 and 306), OFHC[2] copper, tantalum, molybdenum, ceramics, aluminum and Kapton. The preliminary tests performed with the complete crystal holder of CALIPSO (see Chapter 7) did not impact the vacuum quality in the *a*SPECTino source cross. The complete source weights approximately 350 gr.

6.1. Design of the apparatus

The CALIPSO system is contained in a modular parallelepipedal box of $60 \times 60 \times 80$ mm^3, as shown in Figure 6.1. Eight aluminum corners are linked together with small SS316 profiles and the walls of the box are made of SS316 grids. This design allows to set the whole box at a defined potential and to keep an efficient pumping of the source. The front panel is plain apart from the extraction hole, whose position and diameter are dependent on the CALIPSO configuration and needs. This ensures that particles which are not preferentially selected hit the front panel and do not exit CALIPSO, at least not from the front side.

The crystal sits inside its dedicated holder at the back of the box, shown in Figures 6.1 and 6.2. In-between the crystal, which is the place where moderated positrons and low-energy protons are emitted, and the output of the source stand several components, such as: the two drift electrodes, the capillary of the gas inlet, the ^{22}Na positron source and the low-energy electron source. Only one

[1] As the low-magnetic field of *a*SPECTino is not able to contain low-energy protons, it is not possible to apply such a drift in the proton configuration.

[2] Oxygen Free High thermal Conductivity.

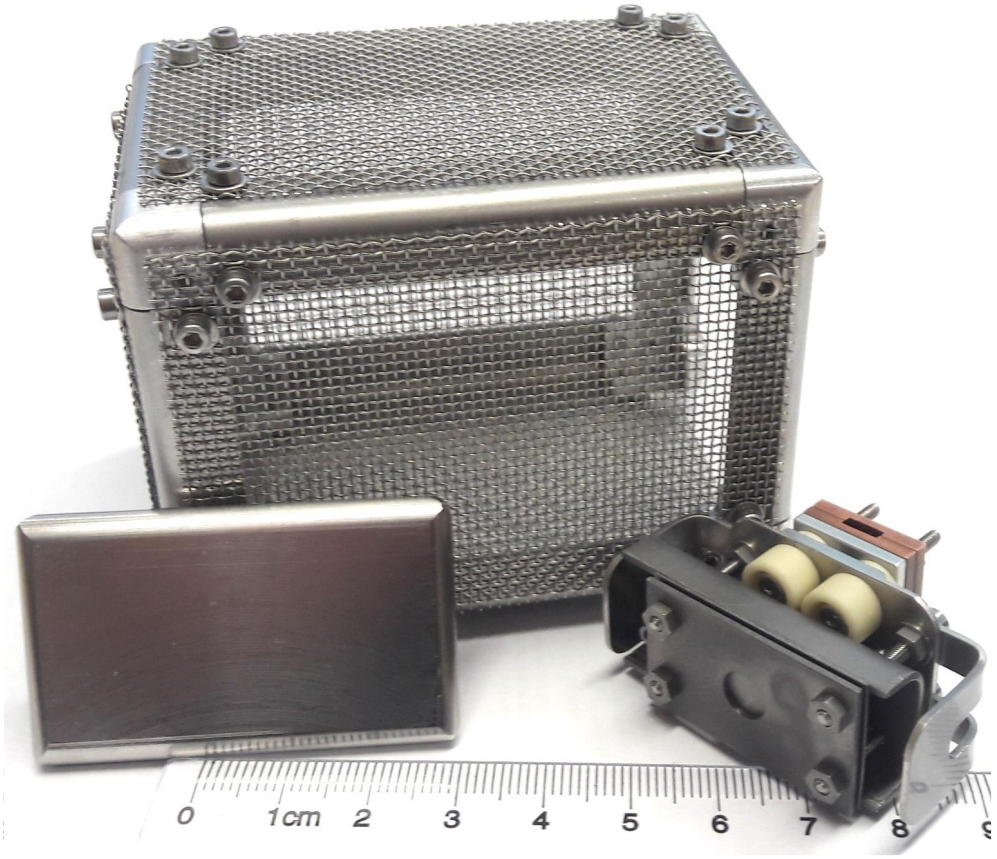

Figure 6.1. Main components of CALIPSO, with a metric ruler as a reference scale. Components are, from left to right: one of the two drift electrodes (see Section 6.1.2.2), the CALIPSO outer box and the crystal holder (see Section 6.2).

component has to be exchanged in order to go from one configuration to the other (i.e., from positron emission to proton emission or vice-versa). Running the CALIPSO source in its positron configuration requires the ^{22}Na radioactive source whereas the proton configuration necessitates the low-energy electron source.

Once the low-energy particles are created and extracted, they come out of CALIPSO and are post-accelerated by the potential difference between the box of CALIPSO and the extraction grid, at ground potential, located in front of the CALIPSO output. This potential, that we will name the CALIPSO potential, defines the output mean kinetic energy of the particles and is, for instance, varied in order to scan a potential for a measurement (see Section 7.2).

In order to operate the source many connections are required through *a*SPECTino. Table 6.1 summarizes all the different feedthroughs, connectors and uses of the cables of CALIPSO as well as the corresponding section to look for more details. The box itself is mechanically fixed on the arm of a magnetic manipulator, as shown in Figure 6.3, allowing the source to be moved along and/or turned around the x-axis.

Table 6.1. List of all the feedthroughs and connectors used for the CALIPSO source. All wires are insulated with Kapton except for the W-Rh wires of the type-C thermocouple which are insulated using ceramic beads. All the thermocouple temperature sensors (both of CALIPSO and *a*SPECTino's coils) are continuously read by a dedicated ADC (Omega d8300) connected to the computer of the experiment.

	Feedthrough		Line		Relevant section
Name	Type	Position	Type	Function	
LN_2 line	2 LN_2 tubes DN40CF	Bot. #1	Stainless steel tubes x 2	Crystal cooling, down to LN_2 temperatures	6.2.1
Crystal heating line	7 pins DN40CF	Bot. #2	⌀ 0.60 mm Cu wire	Hot cathode for crystal electron bombardment	6.2.2.1
Electron source line			⌀ 0.60 mm Cu wire	Hot cathode for ESD on the crystal	6.1.3
Current return line			⌀ 0.60 mm Cu wire	Return line of the two hot cathodes	
CALIPSO box pot.			⌀ 0.25 mm Cu wire	Post acceleration voltage of the output particles	6.1
Crystal potential			⌀ 0.25 mm Cu wire	Dedicated crystal potential for crystal heating and operation of CALIPSO	6.2
Drift electrode #1 pot.			⌀ 0.25 mm Cu wire	ExB drift for particle extraction	6.1.2.2
Drift electrode #2 pot.			⌀ 0.25 mm Cu wire		
Piezo motor line	Sub-D 15 DN63CF	Bot. #3	15 wires& PEEK Sub-D15 connectors	Piezo motor power and control	6.2.3
Crystal TC-C	TC (2K + 1C) DN40CF	Bot. #4	⌀ 0.60 mm W-Rh wires	Crystal temperature measurement up to 2300 °C	6.2.1
Cold source TC-K			⌀ 0.20 mm Chromel and Alumel & Kapton	Cold source temperature measurement, down to −150 °C	6.2.2.1
Optional TC-K			⌀ 0.20 mm Chromel and Alumel & Kapton	Optional type-K thermocouple slot	
Gas inlet	Gas dosing valve DN63CF	Top	Stainless steel capillary	Gas inlet for crystal cleaning and hydrogen deposition	6.1.1

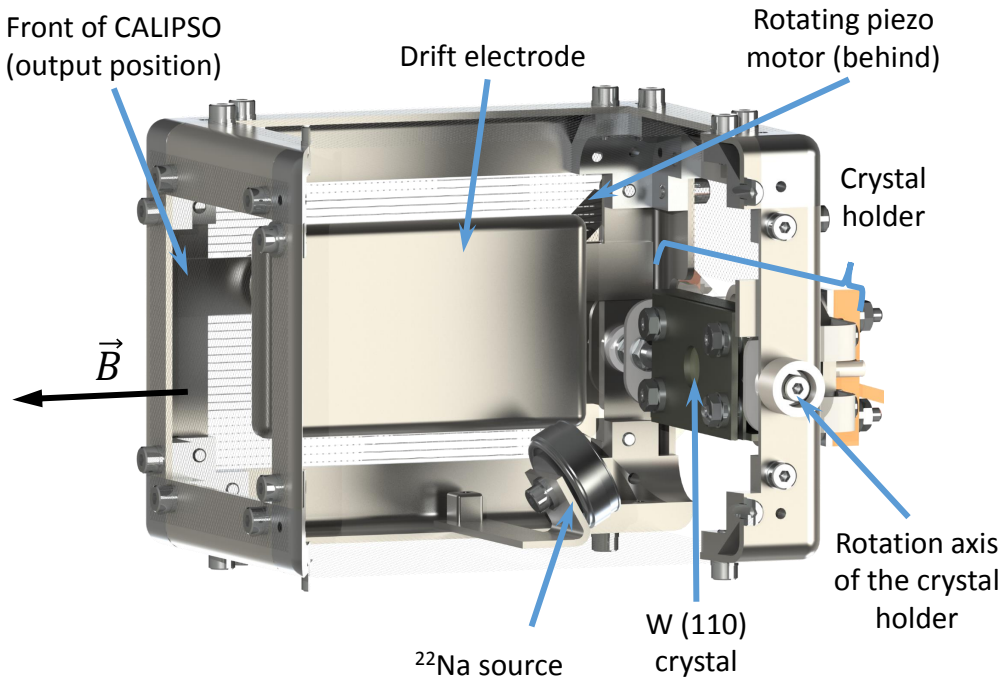

Figure 6.2. View of the inside of the CALIPSO source in its positron configuration. Primary positrons are emitted from the radioactive ^{22}Na source and hit the tungsten (110) crystal maintained in the crystal holder. Two electrodes (as the front electrode would block the view, only the back one is visible here) create a transverse electric field. The resulting drift guides the low-energy positrons towards the exit of the CALIPSO box. The proton configuration is very similar except that the ^{22}Na source is replaced by a low-energy electron source. The magnetic field when CALIPSO is installed in *a*SPECTino is indicated.

6.1.1. Gas inlet

A gas inlet is required for two different tasks. First, as detailed in Section 7.1.2, the cleaning of the crystal's surface has to be performed under a O_2 partial pressure of around 1×10^{-7} mbar [AHB+97, ZPZ+10]. Second, the hydrogen deposit onto the crystal's surface in the proton configuration of the source requires a H_2 exposure with similar partial pressure ranges. A full-metal high-precision gas dosing valve (Pfeiffer UDV 040) is used for the gas inlet. It is installed at the top of the source cross of *a*SPECTino and is rated with a minimal flow rate of $1 \times 10^{-10}\,\mathrm{mbar\,L\,s^{-1}}$ for pure gases.

A thin and flexible stainless steel capillary goes from the leak valve into the top of CALIPSO to guide the gas right in front of the crystal (assuming the crystal is turned upward using the piezoelectric motor described in Section 6.2.3). Since the capillary is at ground (spectrometer potential) and CALIPSO on its own acceleration potential, the capillary is inserted into an alumina tube which is itself covered by an aluminum layer to CALIPSO.

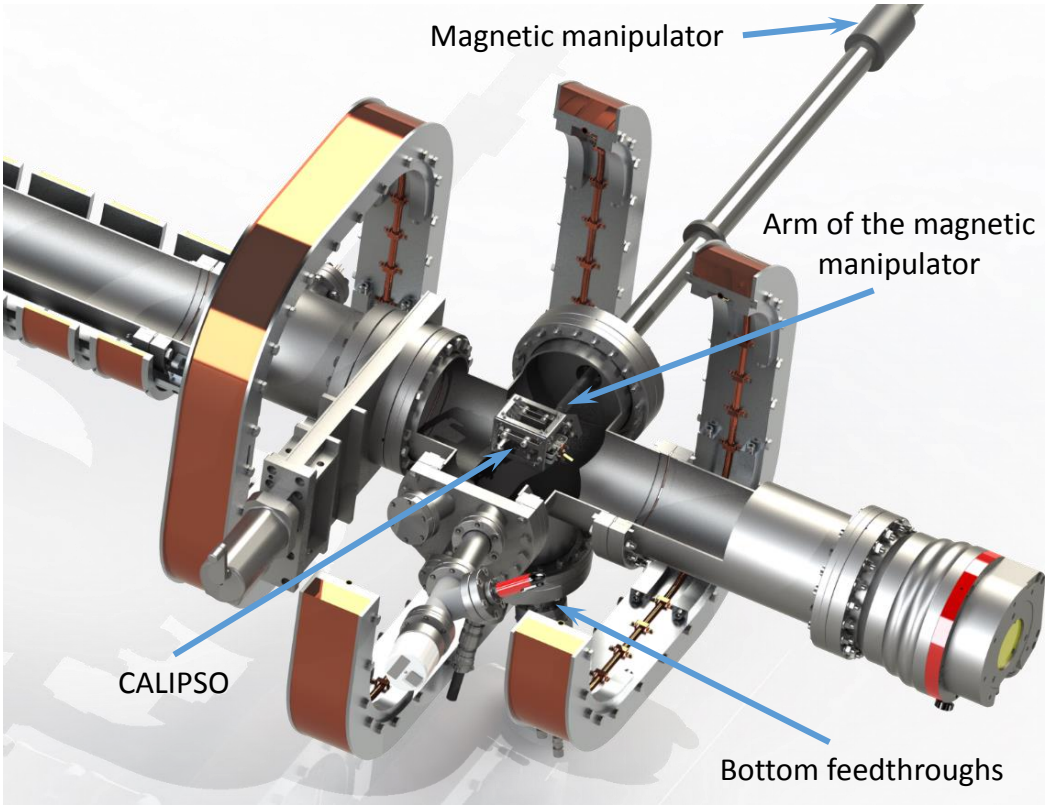

Figure 6.3. Open view of the source cross of *a*SPECTino with the CALIPSO source installed. The bottom flange of the source cross contains four feedthroughs (listed in Table 6.1) while the top flange, hidden in this figure but visible in Figure 5.6, is dedicated to the leak valve feedthrough (description in Section 6.1.1). The CALIPSO source is mounted and accessed through the front flange (i.e., the one in front of the magnetic manipulator and equipped with the pressure sensors).

The air-side connector is a VCR 1/4" where gas bottles can be connected, with a maximum pressure at the valve input of 1.5 bar during operation.

6.1.2. Moderated positron source

Many different geometries are possible for the positron primary source/moderator system, as detailed in Figure 3.7. It is common to couple the backscattering (also called reflexion) geometry with a point-like source in order to avoid blocking of the outcoming low-energy positron beam by the source. Such geometries usually have a higher efficiency compared to transmission geometries [W+15].

The choice made for the positron configuration of the CALIPSO source is to use a backscattering geometry with a 'big' primary source. By taking profit of the magnetic field the source will be exposed to (either in *a*SPECTino or in proton spectroscopy experiments) it is possible to move the primary positron source away from the moderated positrons trajectory at the cost of a smaller efficiency,

as shown in Figure 6.4.

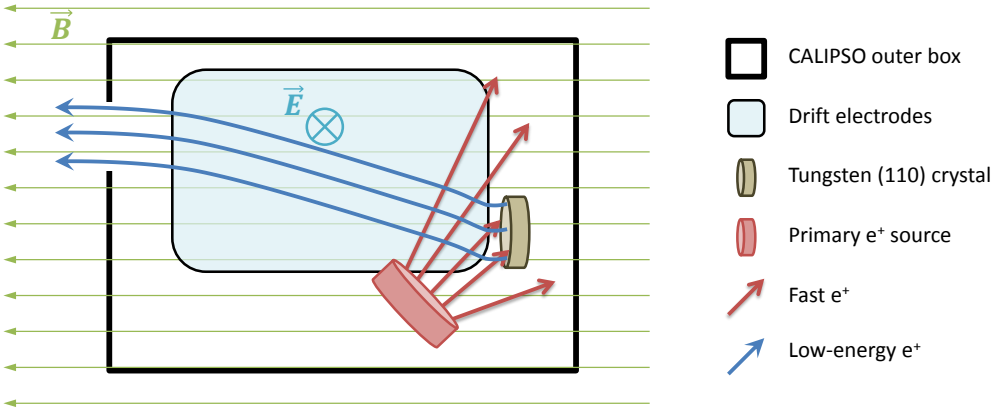

Figure 6.4. Scheme of the positron configuration of CALIPSO. Fast positrons emitted by the primary positron source are bombarding the tungsten (110) crystal. The weak magnetic field does not really impact their trajectory. Some of the positrons hitting the moderator crystal are re-emitted after moderation with a well defined low-energy and an angle close to the normal of the crystal's surface. These positrons are then extracted from the source by an $\mathbf{E} \times \mathbf{B}$ field created by two electrodes.

Depending on the position of the positron primary source compared to the tungsten crystal, the fraction of primary positrons hitting the moderator stands between 2 to 10% in the magnetic field environment of *a*SPECTino. The closer to the crystal the primary source is the higher the ratio, but with an impact on the low-energy positron extraction

6.1.2.1. Positron primary source

Several possibilities for the positron primary source were explored, like ^{64}Cu created by neutron capture on ^{63}Cu at an ILL neutron beamline or ^{58}Co that can be used as a point-like source. However ^{22}Na with its high β^+ branching ratio (90.5%) and long half-life of $\tau_{1/2} = 2.6$ y was identified as candidate. It is usually used in sodium-chloride form and contained in a capsule to prevent radioactive contamination. ^{22}Na β^+ decay,

$$^{22}\mathrm{Na} \rightarrow {}^{22}\mathrm{Ne} + e^+ + \nu_e, \tag{6.1}$$

emits positrons with a broad energy distribution and a maximum kinetic energy $E_{\max} = 545.67$ keV[3] [Bas15], shown in Figure 6.5. Both the main β^+ decay branch and the electron capture branch (the other decay possibility) are accompanied by a 1.275 MeV gamma ray emission from the ^{22}Ne de-excitation. Furthermore every

[3]Two branches exist for the ^{22}Na β^+ decay, the other one leading directly to the ^{22}Ne ground state. The latter being very rare (0.056% of all ^{22}Na decays) it is ignored here.

positron that can not escape the source capsule will be annihilated, resulting in two 511 keV photons. As a result ^{22}Na sources have a substantial gamma emission that needs to be considered when it comes to radioprotection of the users (more details can be found in Appendix C).

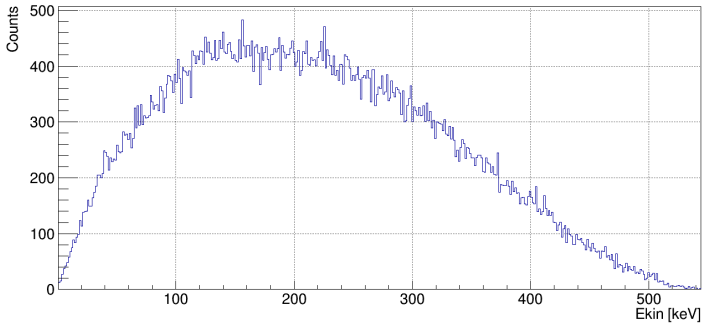

Figure 6.5. Positron spectrum of the main β^+ decay branch for ^{22}Na issued from the simulations. Because of the repulsive potential of the nuclei there is a low probability for low-energy positrons.

From the simulations performed in this work it appeared that an activity of 10^7 Bq or higher was required to get a beam of at least a few hundreds moderated positrons/sec at the CALIPSO output in the worst case scenario (i.e., a low efficiency in the 10^{-4} range). On the other hand having a source with an activity higher than 10^8 Bq would have resulted in a very complicated handling of the source due to its high gamma emission rate. As a result the choice was made to acquire a 1 mCi (37 Mbq) ^{22}Na source.

This commercial source, whose plans are shown in Figure 6.6, is sold in a UHV capsule and was ordered from Eckert & Ziegler. It is composed of a Sodium Chloride deposit on a platinum disk which is encapsulated in a small aluminum case with a 5 µm thick titanium window. Because of the platinum high-Z the back plate acts as a positron reflector (see Figure 3.2). The thin titanium foil allows for a hermetic volume while minimizing the losses during the foil traversal. Simulations showed that more than 60% of the positrons created inside the source capsule are extracted.

The capsule is mounted and stays on a stainless steel support which can be directly installed in CALIPSO when required. When the source is not used it is kept with its support in a dedicated and locked lead castle located in the experimental zone, described in Appendix C.

6.1.2.2. Moderated positron extraction

Two 316 stainless steel electrodes, shown in Figures 6.1 and 6.2, are installed inside CALIPSO to create an $\mathbf{E} \times \mathbf{B}$ drift that increases the low-energy positrons extraction efficiency. The borders of the electrodes facing the center of CALIPSO were limed and polished using high-gritted sandpaper in order to smooth as much as possible the electric field they generate.

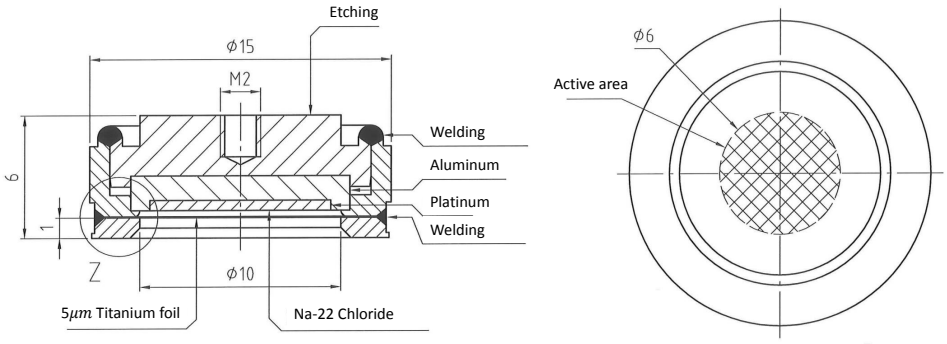

Figure 6.6. Plans of the ^{22}Na source. Figure provided by the manufacturer Eckert & Ziegler.

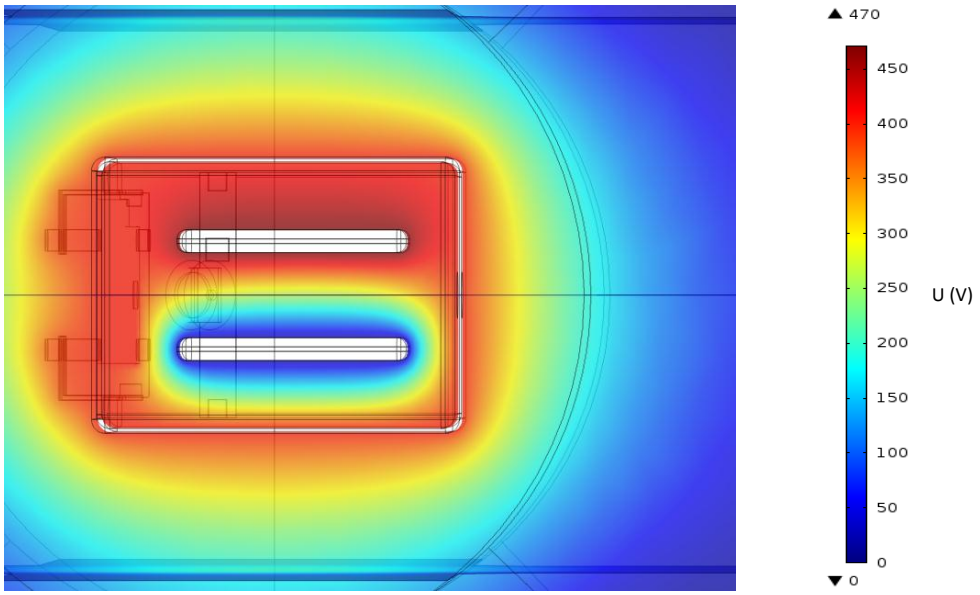

Figure 6.7. Example of electric potentials inside CALIPSO, viewed from the top. In this configuration the acceleration potential of the CALIPSO box is $V_{\text{acc}} = 400$ V, the crystal potential $V_{\text{cry}} = 402$ V and the drift electrodes respectively $V_{\text{Edr1}} = 470$ V (top) and $V_{\text{Edr2}} = 20$ V (bottom). The crystal holder is located at the left of the picture, and the CALIPSO exit on the right.

Simulations of the resulting electric field and drift were performed to find suitable configurations. Figure 6.7 shows an example of the electric potential map inside CALIPSO and Figure 6.8 the resulting drift and the low-energy positrons extraction. Simulations showed that all the re-emitted moderated positrons are extracted from CALIPSO while only a small fraction of fast positrons manages to hit the detector.

It is interesting to note that flat dipole electrodes in $\mathbf{E} \times \mathbf{B}$ setups induces

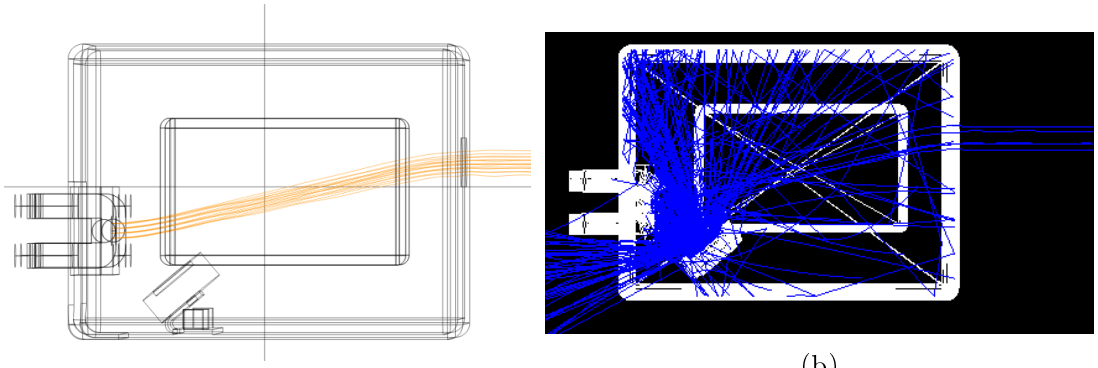

(a) (b)

Figure 6.8. (a): Simulation of the drift induced by the $\mathbf{E}\times\mathbf{B}$ region in CALIPSO on low-energy positrons. This simple dataset was performed directly under COMSOL to get a simple view on the re-emitted positrons extraction. (b): Geant4 simulation of positron extraction in CALIPSO with the same electric field setup as in 6.8a. Positrons issued from ^{22}Na decay that escaped the source capsule may hit the tungsten (110) crystal and may then be possibly re-emitted after being moderated. In this case the EM field setup in CALIPSO guides the low-energy positrons to the exit, as seen on the right of the picture.

a beam distortion, as shown for CALIPSO in Figure 6.9. This effect can be strongly reduced by using cylindrical electrodes [HCWS86]. As this effect is not problematic in this work and the creation of such electrodes is very difficult this solution was not explored.

6.1.3. Proton source

The CALIPSO proton configuration is based around the proton ESD from hydrogen on tungsten (110), as described in Chapter 2. The setup of CALIPSO in this configuration is very similar to the positron one: only the ^{22}Na source is replaced by a simple low-energy electron gun. A hot cathode combined with an extraction grid at low potential provides a broad and uniform low-energy electron beam with a sufficient flux [LY94].

The hydrogen deposition on the surface of the crystal should be perform after it has been cleaned, as detailed in Section 7.1.2. A H_2 partial pressure in the 10^{-8} mbar range during 15 min will result in a saturation coverage of hydrogen. This can be coupled with a short flash[4] in hydrogen ambient to remove the possible few impurities still on the surface [AHB+97].

Because of the low strength of the magnetic field created by *a*SPECTino low-energy protons can not be fully confined. Only protons which are emitted with a low angle compared to the magnetic field lines of the spectrometer have a chance to hit the detector. As described in Chapter 2 protons issued from H-

[4]This term refers to a fast heating of the crystal (in the 1500 °C to 2000 °C range) during a few seconds.

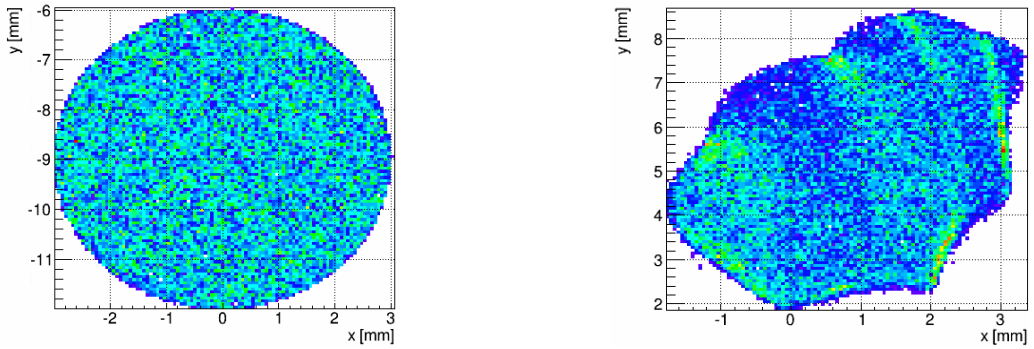

Figure 6.9. Re-emitted moderated positron beam profile at their creation at the tungsten (110) surface (left) and at the output of CALIPSO in aSPECTino, after the $\mathbf{E} \times \mathbf{B}$ drift (right). The expected beam profile distortion is visible in the small compression in the x-direction and the small expansion in the y-direction, with a global deformation of the profile.

W(110) ESD are emitted preferentially normal to the crystal surface. Assuming a Gaussian distribution for the angular emission with a conservative FHWM of 20°, simulations have shown that more than 65% of the desorbed protons would hit the aSPECTino detector. This results is only achievable with no $\mathbf{E} \times \mathbf{B}$ drifts in CALIPSO: the field created by those electrodes is not homogeneous over the whole CALIPSO inner volume and induces asymmetries in the electric field. In the case of protons in a low magnetic field environment, those electric field imperfections lead to strong deviations in the proton trajectories, preventing any proton from hitting the detector.

6.1.3.1. Vacuum deterioration

The source cross of the aSPECTino spectrometer, with the UHV gate closed, has a volume of approximately 10 L and is equipped with a TMP having a pumping speed of about $500\,\mathrm{L\,s^{-1}}$ for light gases such as H_2. The gas load is expressed as:

$$Q = S \times P_{\mathrm{HV}}, \tag{6.2}$$

with S the total pumping speed of the system in L/s, P_{HV} the pressure in mbar and Q the gas load in mbarL/s. The optimistic case of a base pressure of 1×10^{-12} mbar in this volume corresponds to a base gas load of $Q_{\mathrm{b}} = 5 \times 10^{-10}$ mbarL/s. As 1 mbar corresponds to 2.6×10^{16} molecules/cm^3, the base gas load corresponds to 1.3×10^{11} molecules/s entering the system during its normal operation. This gas flow inside the apparatus is mainly due to hydrogen permeation through the stainless steel walls of the apparatus.

The neutral to ionic desorption ratio of ESD is around 1%, as discussed in Chapter 2. Assuming the goal of 10^4 desorbed protons per second, the neutral desorption creates 10^6 H/s, well below the corresponding gas load of an empty system in UHV.

Comparing the neutral desorption rate to the permeation leaks in a UHV system shows that the vacuum deterioration induced by the operation of CALIPSO in its proton configuration is completely negligible even at a base pressure of 10^{-12} mbar.

6.2. Crystal holder

The crystal holder is the critical part of CALIPSO, for both configurations. It is composed of many small and fragile parts and has to provide several different functions:

- **Cooling of the tungsten crystal down to LN_2 temperatures:** As seen in Chapter 2 the hydrogen adsorption process on the tungsten (110) surface should be performed at low temperature to maximize the proton ESD output. Furthermore the energy spread of the moderated positron beam is directly related to the moderator crystal temperature, as shown in Chapter 3.
- **Fast heating of the crystal:** Both CALIPSO configurations require a clean tungsten crystal to operate in good conditions. The cleaning procedure of the crystal, detailed in Section 7.1.2, requires to heat the tungsten up to 1900 °C.
- **Crystal rotation:** Rotating the crystal around the axis shown in Figure 6.2 allows the crystal to directly face the capillary of the gas inlet and to adjust the crystal angle independent from the CALIPSO box. It also allows to reduce the heat load by thermal radiation to the radioactive ^{22}Na source when flash annealing is performed.

Figure 6.10 shows an exploded view of the CALIPSO crystal holder and its high complexity for a small system. The crystal holder is fixed to the structure of CALIPSO through a rotating axis controlled by a piezoelectric-motor. This axis is made of stainless steel and electrically insulated from the rest of the source with ceramic spacers. It was designed to minimize the conduction between the crystal holder and the rest of the CALIPSO apparatus.

6.2.1. Cold source

As argued above the tungsten crystal needs to be cooled down for both configurations of CALIPSO. As shown in Figure 5.5 a fixed LN_2 line connects a dewar to the LN_2 feedthrough of *a*SPECTino, located at the bottom of the source cross.

The LN_2 line inside *a*SPECTino is composed of two stainless steel flexibles welded on both sides of an OFHC Cu block: the nitrogen is in direct contact with the copper. An OFHC Cu braid links this block to the so-called cold source of the crystal holder, ensuring the thermal connection while keeping CALIPSO mobile.

The cold source is located at the back of the crystal holder and is composed of two OFHC Cu plates an one aluminum plate. The braid is firmly pressed

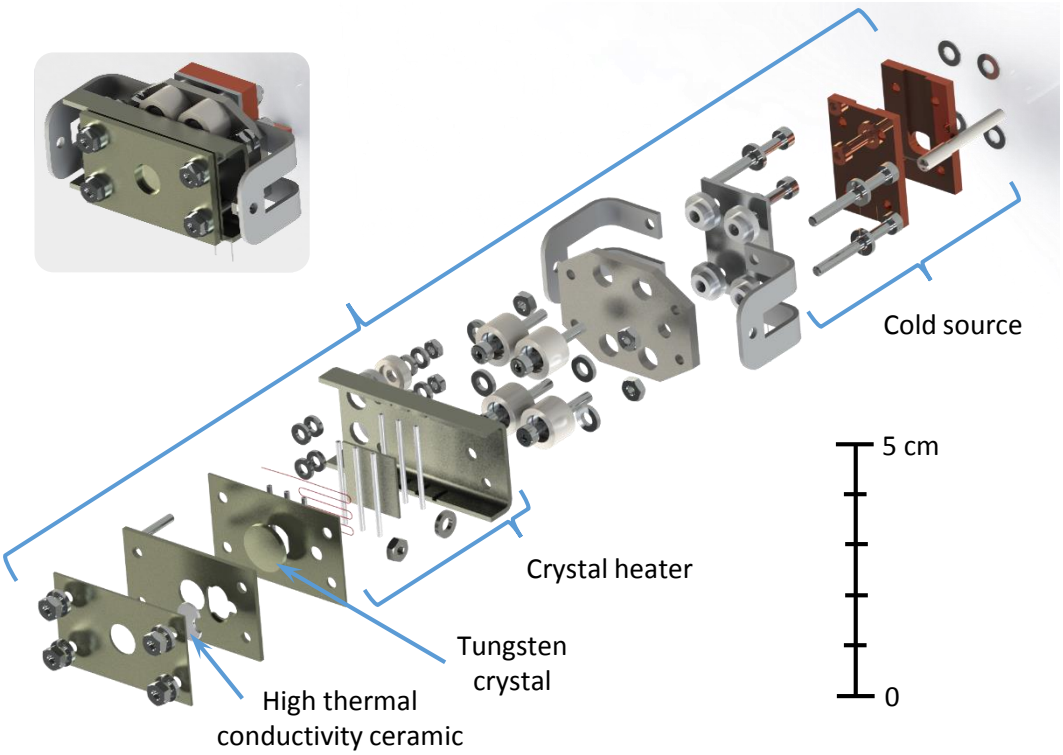

Figure 6.10. Exploded view of the crystal holder of CALIPSO. The cold source, detailed in Section 6.2.1, is located at the back of the crystal holder and is at ground potential. Ceramic isolators separate the cold source potential from the potential of the crystal, which is independent from the one of the CALIPSO box. An assembly of tantalum plates holds the crystal heater and the tungsten crystal, as explained in Section 6.2.2.1. A high thermal conductivity ceramic ensures a proper electric insulation between the crystal and its temperature sensor while maintaining a good thermal connection, as detailed in Section 6.2.2.2.

between the two copper plates and a type-K thermocouple, pressed between the copper block and the aluminum plate, allows to continuously monitor the cold source temperature. As aluminum melts at 660 °C the temperature at the cold source should never exceed a few hundreds Celsius degrees. All those elements are at the spectrometer potential (i.e., at ground).

6.2.2. Crystal block

The second part of the crystal holder is the block containing the tungsten crystal and the crystal heater. A stainless steel plate is used as a platform on which the cold source, the crystal block and the two arms of the rotating axis are connected. As the crystal potential can be different from the one of CALIPSO, ceramic split bushes are used to electrically isolate the crystal block from both the cold source and the rest of the CALIPSO apparatus.

Because the crystal should be heated up to 1900 °C all the elements of the crystal block are either made of tantalum, molybdenum or ceramic which can stand those ranges of temperature.

Four molybdenum screws are holding the four tantalum plates composing the crystal block. The first Ta plate was first machined and then bent twice to form this final U profile. The tungsten crystal is held in-between the three last Ta plates, as detailed in Section 6.2.2.2.

6.2.2.1. Crystal heater

The heating of the crystal is performed by electron bombardment: electrons are emitted from a hot cathode and then accelerated onto the crystal, where they deposite their energy and heat the crystal.

Nine small alumina tubes of 1 mm diameter are inserted into the U shaped plate's grooves and hold a small Ta electrode and the crystal heater hot cathode, as shown in Figure 6.12. The hot cathode and the electrode are set at the same potential and are electrically insulated from the crystal block. The hot cathode consists of a ⌀ 0.15 mm, 90 mm long thoriated tungsten wire[5] shaped to maximize the electronic bombardment onto the crystal, as shown in Figure 6.11. During the heating, the crystal block is set at an accelerating potential of up to 2 kV. The Ta electrode focuses the electronic bombardment onto the crystal by reflecting electrons emitted in the wrong direction and therefore increases the crystal heating while avoiding unnecessary heating of the rest of the crystal holder.

6.2.2.2. Crystal temperature sensor

The crystal temperature is measured using a type-C[6] thermocouple (TC-C) of 0.127 mm diameter installed as close as possible to the crystal, as shown in Figure 6.13. Since the crystal has to be set to high voltage (up to 2 kV) compared to the spectrometer when the annealing is performed, it's not possible to connect directly the thermocouple onto the crystal (thermocouple feedthrough and reading electronics are not rated for such high voltages). The electric insulation and thermal connection is done using a piece of Shapal Hi-M ceramics. This machinable material is one of the rare ceramics that have both a good dielectric strength (here: 65 kV/mm) and a good thermal conductivity (92 $Wm^{-1}K^{-1}$ at 1900 °C).

The other side of the bare TC-C wire is connected, at the back of the crystal holder, to its bare extension grade wire[7] which is protected from undesired elec-

[5] Adding a small amount of thorium oxide in tungsten (W 99 /ThO_2 0.9% in our case) reduces strongly the material work function, from 4.55 eV down to 2.64 eV [Hay16, SOMSC10]. As a result electron emission at the same filament temperature is higher, as the potential barrier to overcome is smaller.

[6] A type-C thermocouple is composed of Tungsten-5% Rhenium vs. Tungsten-26% Rhenium and can measure temperatures in the 0 °C to 2320 °C range. The addition of rhenium makes the alloy less brittle.

[7] Extension grade wires are cheaper and usually easier to handle than thermocouple grade wires but can not withstand a similar temperature range. They allow to easily extend the spatial range of thermocouple probes.

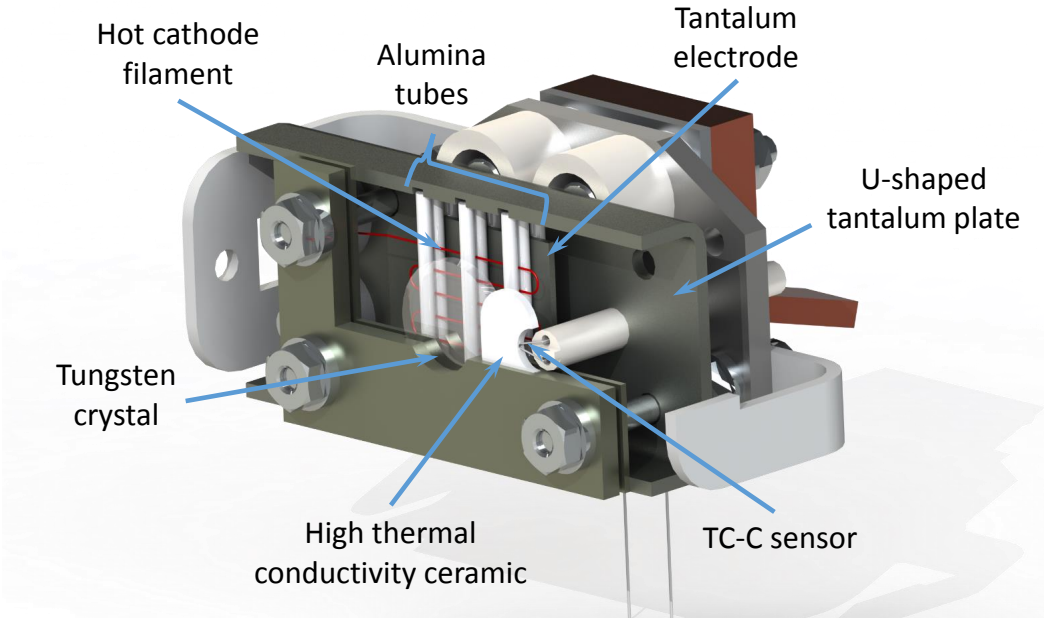

Figure 6.11. Partial open view of the crystal holder. The tungsten crystal is shown transparent in order to make the crystal heater more visible. The U shaped tantalum plate holds three stacks of three alumina tubes in dedicated grooves. These aluminum tubes are holding the crystal heater system, as detailed in Section 6.2.2.1. The tungsten crystal temperature is measured using a type-C thermocouple in thermal contact with the crystal through a dedicated high-thermal conductivity ceramic, as described in Section 6.2.2.2.

trical contacts by ceramic beads. After the feedthrough, the air-side of the line is plugged into the temperature reader of aSPECTino, as all the temperature sensors of this system.

6.2.3. Piezo motor

The rotation of the crystal, as described in the introduction of Section 6.2 and in Figure 6.2, is performed by a small closed loop[8] UHV piezo rotator (Attocube ECR3030), shown in Figure 6.14. The body of the motor is made of stainless steel and can be baked out to a maximum temperature of 150 °C. An optoelectronic readout mechanism gives the relative position of the rotator over the full 360° endless range, with a precision of the order of the 1/1000 degree.

The piezo motor can be operated in the 0 °C to 100 °C temperature range. It is connected to the rotation axis through low-thermal conductivity components (ceramic spacers and stainless steel screws) and is connected to the magnetic

[8] Closed loop rotators, opposed to open loop rotators, have an integrated encoding system. As a result the absolute position of the rotator is known, resulting in a better reproducibility and a higher precision.

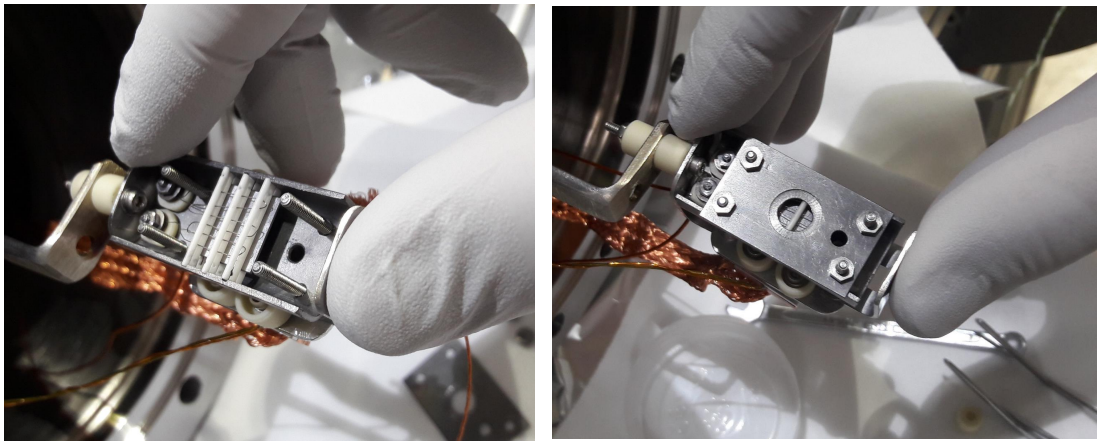

(a) (b)

Figure 6.12. (a): CALIPSO crystal holder during its assembly. The 3×3 ceramic tubes are holding the Ta electrode and, above it, the hot cathode filament. All the ceramic tubes are vented by little incisions on each of their side. The two Ta screws and washers for the hot cathode current inlet are visible on the left, below the index. (b): Picture of the same setup but with the first Ta plate installed. This plate holds the crystal heater parts and a circular groove, in its center, holds the tungsten crystal in place. As seen through the central hole of this plate the tungsten crystal is in direct view of the hot cathode filament.

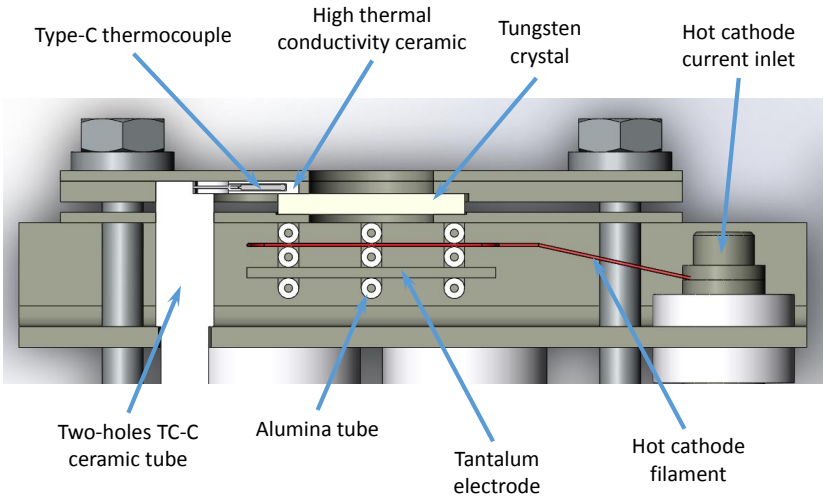

Figure 6.13. Side view of the crystal block. The alumina tubes, Ta electrode and hot cathode filament are visible below the crystal. Part of the crystal top surface is in direct contact with the high-thermal conductivity ceramic piece. The TC-C sensor is inserted inside a small hole of this ceramic element, as close as possible to the crystal. The rest of the thermocouple wire is then guided and protected by a long two-holes ceramic tube to the back of the crystal holder.

manipulator arm with an OFHC Cu braid in order to keep its temperature in its operating range.

Figure 6.14. Picture of the CALIPSO UHV piezo rotator (left) and its UHV cable and connector (right).

Conclusion

This chapter listed and discussed the technical requirements for the CALIPSO source and detailed the design and characteristics of CALIPSO, for both its proton and positron configurations, and several simulations results have shown the expected behavior of CALIPSO. The majority of the source components are common between the two CALIPSO configurations, allowing an easy switch between the two possibilities the source offers. The design of CALIPSO and of its crystal holder allows fulfill all the requirements needed for the creation of a moderated positron beam and a low-energy ESD proton beam (heating to high temperatures and cooling to cryogenic temperature of the tungsten crystal, moderated positron extraction etc.)

Chapter 7

Results and outlook

Experimentation is the least arrogant method of gaining knowledge. The experimenter humbly asks a question of nature.

(Isaac Asimov)

Contents

7.1. Preliminary tests of the crystal holder 99
7.1.1. Cold source 100
7.1.2. Crystal cleaning and annealing 102
7.2. Procedure for potential comparison 106
7.3. Strong magnetic field environment 110
7.3.1. Positron configuration 110
7.3.2. Proton configuration 111

Preliminary tests were performed on several features of the CALIPSO source. Their outcome as well as solutions for the encountered problems are presented in this chapter. The comparison of electric potentials using CALIPSO is detailed and the few modifications of the setup that should be applied to use efficiently CALIPSO in proton spectroscopy experiments with a strong magnetic field are presented.

7.1. Preliminary tests of the crystal holder

The central importance of the crystal holder in CALIPSO as well as its complexity justify tests of the crystal holder as a stand-alone apparatus, outside CALIPSO. Those preliminary tests were dedicated to the cooling and heating of the tungsten (110) crystal, replaced for these measurements by a polycrystalline tungsten disk. Figure 7.1 shows the installation of the crystal holder in the aSPECTino source cross, before installing the polycrystalline tungsten disk. During these tests a

small quartz window was installed at the front flange of the source cross, giving a direct view on the crystal holder.

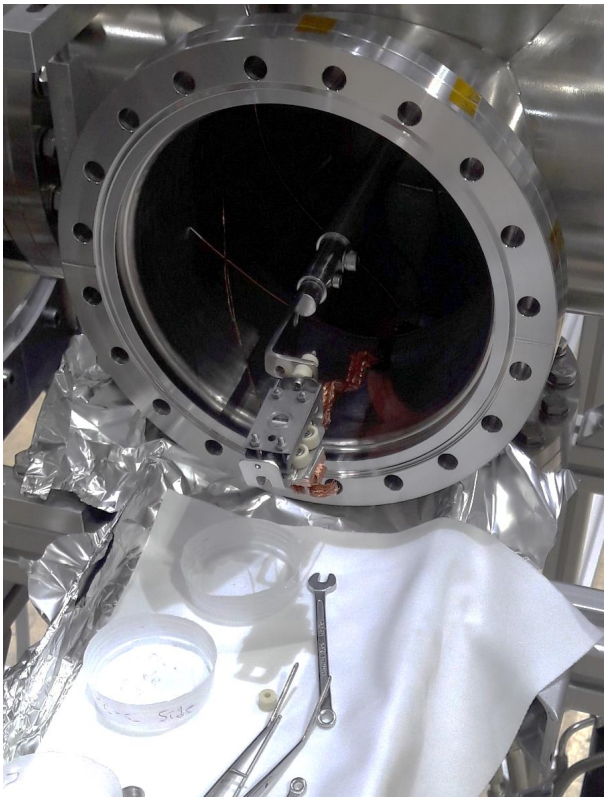

Figure 7.1. Installation of the crystal holder into the source cross of *a*SPECTino. The front flange of the source cross is removed to allow the magnetic manipulator arm to be outside of the vacuum tubing for the installation of the crystal holder (or CALIPSO).

7.1.1. Cold source

The cooling of the crystal holder is performed using a continuous flow of gaseous (or liquid) nitrogen into the LN_2 line, coming from an external dewar. As shown in Figure 7.2 the cold source of CALIPSO went from room temperature to 200 K in approximately two hours. As liquid nitrogen was flowing from the output of the LN_2 line, the copper cold block inside *a*SPECTino, in direct contact with liquid nitrogen, was expected to be at 77 K. The cold source of the crystal holder could not reach this temperature and always stabilized at 200 K. Even though the CALIPSO source can still operate at this temperature level, its performances would improve at lower temperature for both its configurations, as described in Sections 2.2.2 and 3.3.3.

Such a temperature level can be the due to:

- **Poor mechanical contact between the copper blocks and the copper braid:** the OFHC Cu braid connecting the crystal holder cold source

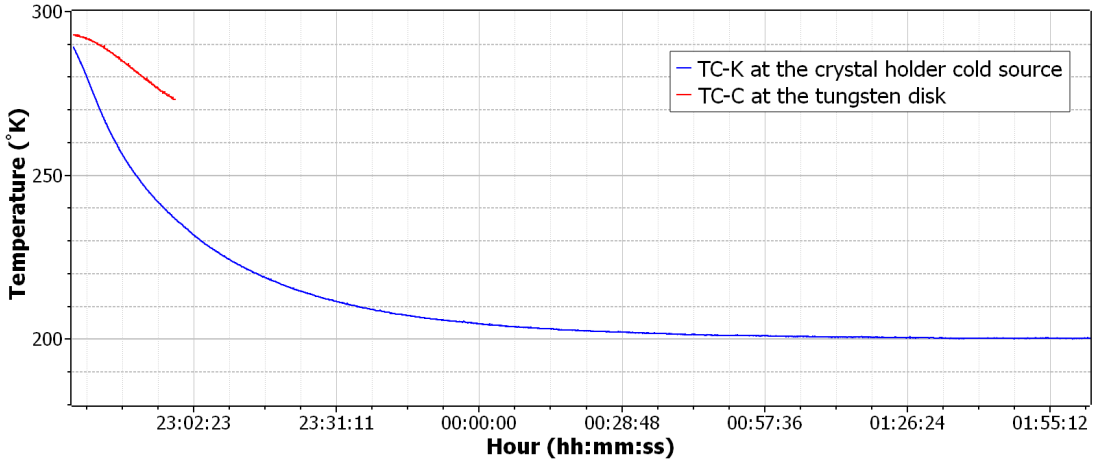

Figure 7.2. Cooling curve of the crystal holder. The temperature is measured at the cold source of the crystal holder using the dedicated type-K thermocouple (blue) and at the tungsten crystal position using a type-C thermocouple (red). The latter is dedicated to the measurement of high temperatures and its reading system does not provide any temperature information below 0 °C.

to the cold block of the LN_2 line is pressed between two OFHC plates, at both of its extremities. Even though it is firmly compressed the resulting thermal contact may be insufficient and therefore limit the heat transfer.

- **Thermal radiation from the spectrometer:** the crystal holder is surrounded by the vacuum chamber of the spectrometer which stands at room temperature. The thermal radiation on the crystal holder is therefore consequent and is most probably a strong limiting factor in this measurement.
- **Heat transfer at the magnetic manipulator arm:** the physical contact between the crystal holder and the magnetic manipulator axis may induce a heat transfer. However these two elements are in physical contact through a ceramic (Steatite C-221)/stainless steel interface of 40 mm^2, with both those materials having a low thermal conductivity of respectively 2.5 and 16 $Wm^{-1}K^{-1}$ [MW05, Hay16]. This contribution should therefore be small and not be the dominating problem here.
- **Insufficient cooling power:** the LN_2 flow may be insufficient and limit the cooling capacity. However this option is excluded as one can get a strong flow of LN_2 at the output of the cooling line.

In order to maximize the heat exchange at both copper braid extremities some indium should be added at the copper braid/copper block interface. Because of its high malleability indium will fill all the possible empty spaces and ensure a proper thermal connection between the copper blocks and the copper braid.

Concerning the thermal radiation problem, several improvements are proposed. First a small aluminum envelope could be added around the crystal holder, as

shown in Figure 7.3. This box would be thermally connected directly to the cold source of the crystal holder and therefore be at the same potential (i.e., ground). Its outer surface should be polished to reduce as much as possible its absorptivity and act as an efficient thermal radiation screen.

Figure 7.3. Aluminum thermal radiation screen for the crystal holder. Only a few mechanical adjustments are required on the CALIPSO outer box to install this upgrade.

Second the rest of the outer elements of the crystal holder and specifically the front tantalum plate should also be polished, for the same reason. Finally the wrapping of the copper braid with multi-layer insulator[1] (MLI) was considered and is easy to implement, but may be poorly effective. As the copper braid is flexible and is moving during the CALIPSO source installation and operation, the MLI would have to be highly segmented over the braid length to keep the same mobility, reducing its effectiveness. The implementation of these three upgrades should allow to reach much lower temperatures at the cold source and the crystal of CALIPSO.

No thermocouple can be used in the full range of temperatures the tungsten crystal is exposed to. Therefore only a type-C thermocouple (TC-C), dedicated to high-temperatures, is installed near the crystal. In order to perform a calibration of the temperature evolution at the crystal compared to the one at the cold source of the crystal holder a type-K thermocouple has to be installed at the place of the TC-C. The calibration should be performed for both cooling and light heating[2].

7.1.2. Crystal cleaning and annealing

The tungsten crystal bulk and surface quality is of primordial importance for the good operation of CALIPSO, as mentioned many times in this work. The crystal needs to be annealed in order to remove defects from the lattice and to have a clean surface to maximize the re-emission of moderated positrons and to perform the hydrogen deposit in the proton configuration.

[1] Multi-layer insulator consists of a piling of two layers: one with a high reflectivity and one with a low thermal conductivity. Each new layer acts as the previous layer thermal radiation screen: the higher the number of layers, the more effective the insulation. In the case of a UHV setup those two layers are usually a thin aluminum deposit on top of Kapton.

[2] Type-K thermocouples can only withstands temperatures lower than 1260 °C.

Tungsten is a popular substrate in surface science and well defined cleaning procedures of tungsten crystals have been developed, such as in [ZPZ+10]. This procedure can be decomposed into two steps. First, as carbon trapped in the bulk of tungsten is migrating to the surface during annealing, several heating sequences at around 900 °C are performed in oxygen atmosphere. The oxygen reacts with the carbon at the surface of the crystal, forming CO gas. A mass spectrometer can be installed at the front flange of the source cross to track the CO partial pressure and determine if carbon is completely removed from the crystal or not [ZPZ+10].

Once the surface is carbon-free, the second step of the procedure is dedicated to the removal of the oxide layer created by the previous operation and the atomic oxygen trapped on the surface. This is done by heating the crystal up to 1900 °C in vacuum (i.e., with closed oxygen leak valve) for a few seconds. This procedure is commonly called flash annealing.

As the flash annealing may have induced segregation of carbon from the bulk to the surface, another flash annealing in oxygen atmosphere can be performed and the CO partial pressure monitored, similarly to the first step but at 1900 °C. If no CO peak is detected the crystal can be considered clean and annealed, otherwise the whole operation should be performed again. The complete cleaning procedure taken from [ZPZ+10] is summarized in Figure 7.4.

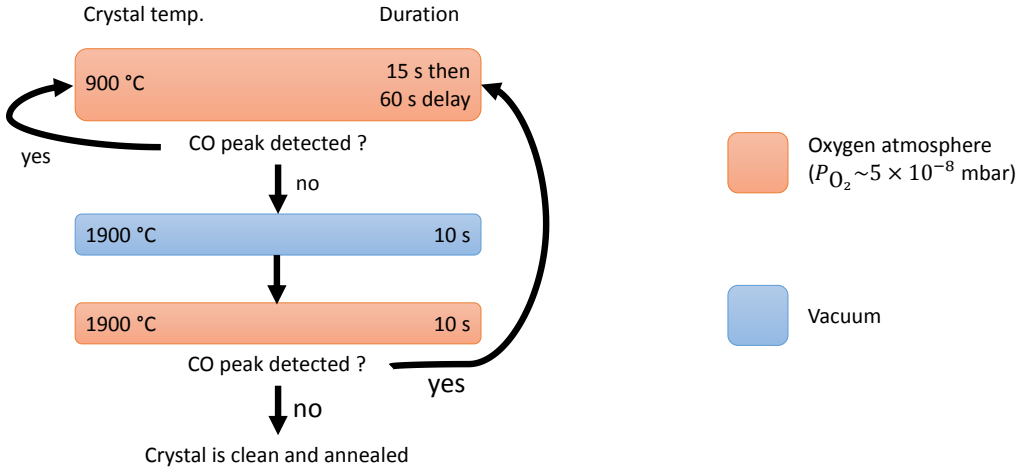

Figure 7.4. Steps of the cleaning and annealing procedure described in Section 7.1.2.

7.1.2.1. Hot cathode

The crystal heater required to perform the cleaning and annealing procedure and described in Section 6.2.2.1 was tested along with the cold source but without the acceleration potential at the crystal since the high-current and high-voltage power supply was not available at this time. Therefore the resulting heating power and consequently the temperature measured at the crystal position are

not representative of the crystal heater real capacities, as discussed below. Those measurements were rather a good opportunity to test the hot cathode and the response of the two thermocouples to a heat load.

Pictures of the crystal heater filament for different currents are shown in Figure 7.5 and the measured temperatures during the operation of the filament at 4 A during 30 s without LN_2 cooling are shown in Figure 7.6. As expected there is a strong difference in the temperature response from the two parts of the crystal holder to the generated heat load. The cold source temperature rise was both smaller and slower then its counter-part.

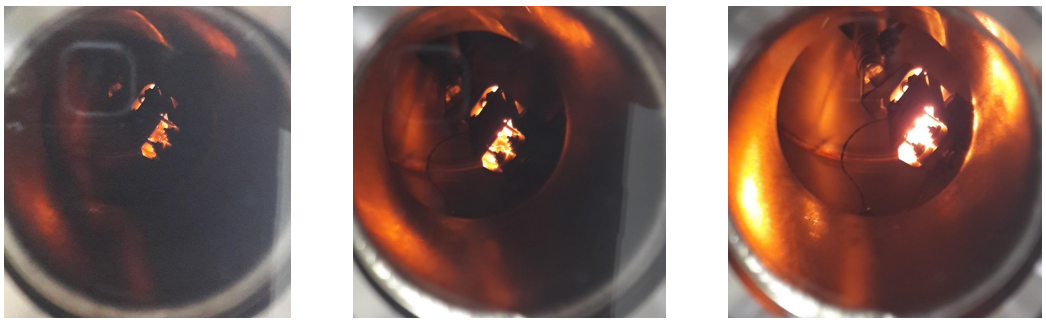

Figure 7.5. Pictures of the inside of the cross source of *a*SPECTino during the tests of the crystal holder hot cathode. The current passing through the filament is respectively, from left to right, 1.5 A, 1.8 A and 2.1 A. Much higher currents, up to 4.5 A, were tested but there was too much light emission to see anything on the pictures.

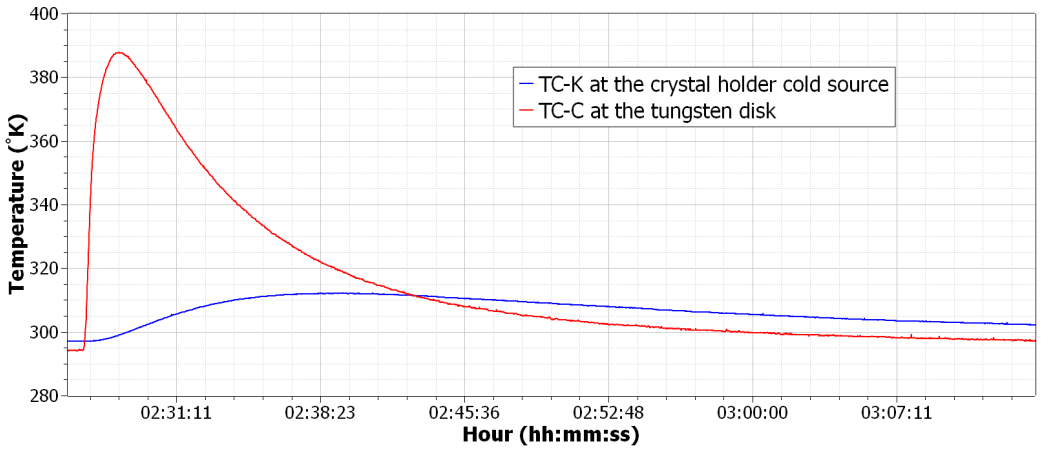

Figure 7.6. Measured temperatures of the crystal disk and the cold source of the crystal holder. The hot cathode filament was traversed by a current of 4 A during 30 secs, with the crystal holder (including the cold source) starting at approximately 273 K. This measurement was performed during the system warming meaning that the LN_2 cooling was stopped. No acceleration potential was applied to the crystal.

The crystal heater hot cathode current was tested up to 4.5 A for a few seconds and the system was then cooled and dismounted to check the status of the different parts of the crystal holder. As shown in Figure 7.7 several parts ended up destroyed: the hot cathode filament, the high-thermal conductivity ceramic for temperature sensing at the crystal and one of the alumina tubes holding the filament.

Figure 7.7. Picture of the damaged parts (in red) of the crystal holder: the high-thermal conductivity ceramic (top left), the hot cathode filament (bottom left) and one of the alumina tubes (right).

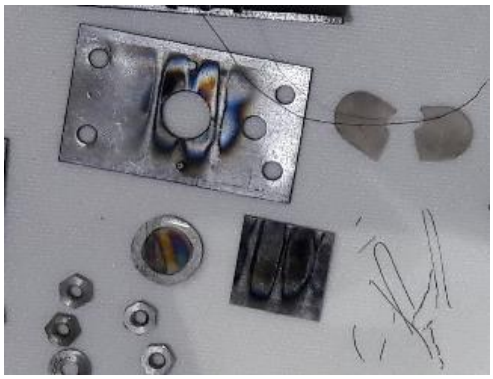

Figure 7.8. Zoom on the tungsten disk and tantalum plates. All the parts exposed to the filament show the same iridescent pattern on their surface and the filament broke at several places.

The ceramic part used for measuring the crystal temperature is the most fragile part of CALIPSO: a 3 mm deep hole of 0.35 mm diameter has to be drilled in the

0.60 mm thick side of the part. This very sensitive operation can be performed using a slow drilling speed, a micro feed chuck and above all patience. It is not clear if the breaking of this piece is related to mechanical constraints during its very difficult assembly, during the cooling tests or during the heating tests. In any case after this measurement a new design of this piece and the tantalum plates holding it has been developed in order to:

- Simplify as much as possible the assembly,
- Reduce the mechanical constraints on the piece while maintaining a good contact with the tungsten crystal.

The schemes shown in Chapter 6 are already showing this new design.

Similarly to the cold source/crystal temperature calibration, the temperature at the tungsten crystal can be measured. Such test would allow to confirm the temperature response of the TC-C used in conjunction with the high-conductivity ceramic part and to calibrate it.

7.2. Procedure for potential comparison

One of the main motivations of the moderated positron source is to compare electrostatic potentials of electrodes with ≤ 10 mV accuracy (see Chapter 1). A simulation was performed to estimate the precision that can be achieved in such comparison. The simulation setup is composed of CALIPSO and *a*SPECTino equipped with a cylindrical electrode located at the AP. A selection potential is applied to the electrode and only the positrons that pass through this barrier are counted in the *a*SPECTino detector. The acceleration potential of CALIPSO V_{acc} (i.e., the mean kinetic energy of the positron beam) is varied to scan this potential.

After having accumulated enough data the electrode potential is shifted by 10 mV and the same procedure is performed again. Such a simulation was done for a moderator crystal temperature of 200 K corresponding to an energy spread FWHM of approximately 45 meV and achievable in the existing setup (see Section 7.1). Six different V_{acc} values were used with 50k low-energy positrons per potential, for a total of 600k simulated low-energy positrons. The simulation's results are detailed in Table 7.1.

In order to interpret the procedure, let's first assume that all positrons are emitted strictly parallel to the magnetic field lines and that axial components of the electric field of the electrode are negligible. Then positrons with an energy higher than the potential difference, $E + eV_{\mathrm{acc}} > eU_{\mathrm{elec}}$ are transmitted. E is the positron kinetic energy after moderation. Assuming a Gaussian energy distribution after moderation with mean energy E_0 and standard variation σ, the fraction of transmitted positrons can be calculated as follows:

$$T(V_{\mathrm{acc}}) = \int_{e(U_{\mathrm{elec}}-V_{\mathrm{acc}})}^{\infty} \frac{1}{\sqrt{2\pi\sigma^2}} \exp -\frac{(E-E_0)^2}{2\sigma^2} dE. \tag{7.1}$$

Table 7.1. Results of the simulation of potentials comparison. As the acceleration potential of CALIPSO is varied the number of positrons that can pass the electrode potential is also changed. 50k low-energy positrons are created per acceleration potential value and per configuration. The difference between the two configurations U_{elec} and $(U_{\text{elec}} + 10\ \text{mV})$ is the strongest in the transition region (in this example $V_{\text{acc}} = 176.75$ and $V_{\text{acc}} = 176.76$). These are the high-sensitivity points.

	U_{elec}		$U_{\text{elec}} + 10$ mV	
V_{acc} (V)	Counts	Stat. error	Counts	Stat. error
176.00	0	1	0	1
176.20	0	1	0	1
176.75	24440	156.3	23060	151.9
176.76	25122	158.5	23965	154.8
177.20	49670	222.9	49530	222.6
177.40	50000	223.6	50000	223.6

This can be rewritten using the error function:

$$T(V_{\text{acc}}) = \frac{1}{2}\left(1 + \text{erf}\left(\frac{eV_{\text{acc}} - (eU_{\text{elec}} - E_0)}{\sqrt{2}\sigma}\right)\right). \tag{7.2}$$

This means that the resulting transmission has a width that is related to the width of the initial energy distribution of the positrons. This underlines the interest to use a narrow energy distribution, as obtained from moderated positrons.

The position of the transition, $eU_{\text{elec}} - E_0$, depends on the initial mean positron energy and the applied potential. Different potentials (or electrodes) can be compared by using the same initial energy distribution and scanning V_{acc}. In reality, the positron energy distribution is not perfectly Gaussian (a Maxwell-Boltzmann distribution is more realistic and was used in the simulations) and the angular distribution with respect to the magnetic field broadens the width of the transmission, depending on this distribution and on the magnetic field ratio between emission point and electrode. Because of the preferred forward emission of moderated positrons, this broadening should be small. Further deviations from the derived error function (see Equation (7.2)) may be caused by non-axial electrostatic field components.

To analyze the data, the simulated transmission of positrons for the two different electrode voltages U_{elec} and $(U_{\text{elec}} + 10\ \text{mV})$ were fitted as a function of V_{acc} using Equation (7.2), with the parameters σ and $b = U_{\text{elec}} - E_0/e$ (E_0 and U_{elec} cannot be separated). The parameter σ was the same for both fits. Concerning the errors, the values in Table 7.1 come from simulations, resulting in exactly 50000 positrons if V_{acc} is high enough. In experiment, this number would fluctuate because of the statistical emission from the source. Therefore $\sqrt{N}$ is used as

uncertainty and 1 in case of 0 counts. The fit results are:

$$\sigma = 0.137(5)\ \text{eV},$$
$$b1 = 176.757(1)\ \text{V},$$
$$b2 = 176.765(1)\ \text{V},$$

with a reduced $\chi^2 = 2.9$. The high χ^2 value reflects the imperfect description of the transmission by the error function as discussed above. However, the sensitivity and accuracy of the potential comparison is well below 10 mV for the simulated statistics.

If V_{acc} is below $U_{\text{elec}} - E_0/e$, the rate in the experiment is dominated by background. Background can be determined by applying $V_{\text{acc}} = 0$ and subtracted but increases the uncertainty. In order to estimate the effect, we use the aSPECT background rate in the region of interest of about 0.1 Hz [Mai14]. Assuming 1000 s per data point, the uncertainty due to background is about 10 counts. This uncertainty was added to that of the simulations and used in the fits. The results are

$$\sigma = 0.161(7)\ \text{eV},$$
$$b1 = 176.757(1)\ \text{V},$$
$$b2 = 176.767(1)\ \text{V},$$

with $\chi^2 = 1.5$ – the uncertainty due to background modifies the sensitivity to σ (and absorbs a part of the imperfections of the fit function) but barely effects the results for the potential comparison itself.

Such a result was achieved with a total of 600k positrons. In the very pessimistic scenario of the CALIPSO source having a moderated positron re-emission efficiency of only $\epsilon = 10^{-4}$ and that only 2% of the created positrons in the ^{22}Na source capsule hit the crystal moderator (value for the configuration shown in Figure 6.8), it would emit around 40 low-energy positrons per second. It would therefore take approximately 4 hours to compare two potentials over one beam trajectory with an accuracy of at least 10 mV in aSPECTino. However if we assume the CALIPSO source to perform at its expected level ($\epsilon = 1 \times 10^{-3}$) and to emit at least 700 low-energy positrons per second, the time to scan a beam trajectory is reduced to only 15 minutes. Furthermore as detailed in Section 7.3 using CALIPSO in a high magnetic field, as in the case of proton spectroscopy experiment such as aSPECT or PERC, induces a much higher low-energy positrons yield.

In the aSPECT spectrometer, the three silicon detectors of the apparatus are sensitive to a projected area in the region where protons are created, called the Decay Volume (DV), of around 800 mm^2[Mai14]. These protons are guided by the strong magnetic field towards the analyzing plane (AP) of the spectrometer where they are selected due to the selection potential created by the AP electrode. The precise knowledge of the absolute potential difference between these two regions (AP and DV) is a very important systematic effect of this experiment, as already discussed in Chapter 1. In order to compare these two potentials using

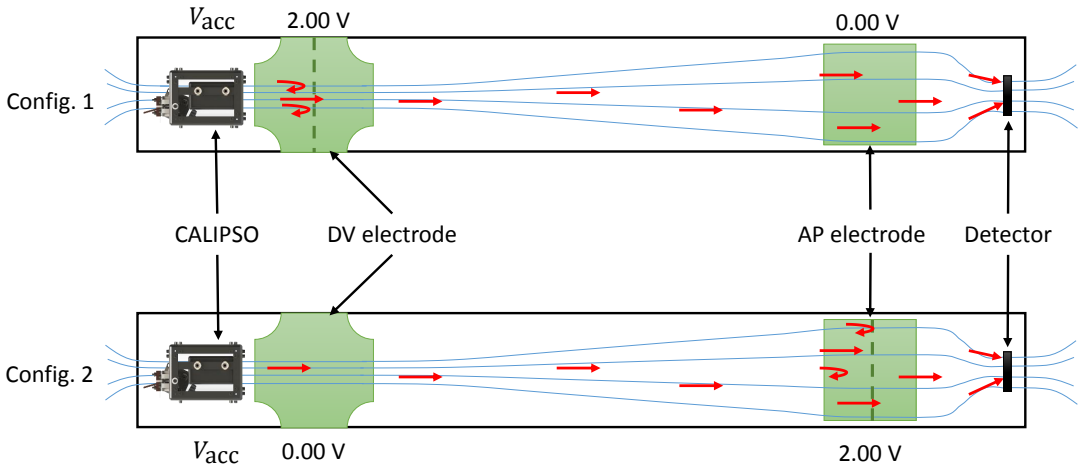

Figure 7.9. Scheme of the two configurations of *a*SPECT that can be used to compare the absolute potential between the region where protons are created by neutron β-decay (DV) and where they are selected (AP). The first configuration is sensitive to the DV potential, with the CALIPSO source acceleration potential V_{acc} tuned around 2 V. By setting the AP potential to 0 V, no positrons that passed the DV barrier are reflected at the AP. In configuration 2, the AP potential is ramped up to the desired value, 2 V in this example, with DV at 0 V. To perform the scan of this potential V_{acc} is tuned around the new AP potential. Using similar V_{acc} for both sources reduces potential systematic effects in positron extraction and transport. By comparing the results of the two scans one can derive the absolute potential differences, as demonstrated in the simulations shown above.

CALIPSO, the source could be installed behind the DV electrode, facing the AP and the detectors, as shown in Figure 7.9.

In order to compare these two potentials the following two configurations can be used: first the DV is set to 2 V and the AP to 0 V and second the potentials are exchanged, the DV is set to 0 V and the AP to 2 V. Using such a setup ensures that during the first configuration all the positrons that did pass the DV potential can not be reflected by the AP. Once the potential comparison procedure described above, scaled to this setup, is performed the absolute difference between the DV and AP potentials over the beam trajectory is known. The transmission mainly depends on the energy and also on the angular distribution of the positrons – in order to change them as little as possible comparisons should be done at similar acceleration voltages and magnetic fields (the latter is of course not achievable if one compares DV and AP). This measurement should then be repeated at a new position until the entire relevant DV and AP area is scanned.

As low-energy positrons of the CALIPSO source are emitted all over the 6 mm diameter crystal's surface, the CALIPSO low-energy positrons beam size is of the order of 28 mm^2 (the beam spread due to the gyration movement is ignored due to the tiny Larmor radius in such a strong magnetic field). As a result it would require approximately 30 potential comparison measurements to scan the totality of the relevant space. Using the very conservative 10 minutes per run (due to higher positron yield, see Section 7.3.1) this means the complete comparison of two potentials for a defined electric potential configuration with an accuracy of at least 10 mV is possible in a few hours.

7.3. Strong magnetic field environment

In order to use CALIPSO in proton spectroscopy experiments the source needs to be adapted to strong magnetic environments. In the case of the aSPECT spectrometer mentioned in the previous section, this means that CALIPSO will be operated in a 2.2 T magnetic field. In such environment both low-energy protons and high-energy positrons are well confined. With only a few design modifications[3], the consequences on the CALIPSO source performance are highly beneficial for both its configurations.

7.3.1. Positron configuration

For the positron configuration the main advantage is the confinement of high-energy positrons emitted by the ^{22}Na source. By installing the primary positron source several centimeters away from the tungsten crystal but in its direct view, simulations showed that approximately 37.5% of the positrons created inside the source capsule are hitting the positron moderator crystal. This results in a high production rate of low-energy positrons: around 14k/s assuming a moderation efficiency of $\epsilon = 1.1 \times 10^{-3}$. However the strong magnetic field imposes a much

[3] The two electrodes should be enlarged a bit and the CALIPSO housing extended of 20 mm to contain the longer electrodes.

higher transverse electric drift field (of the order of $150\,\mathrm{V\,mm^{-1}}$ along the x-axis) in order to avoid hitting the ^{22}Na source capsule with the moderated positron beam. Such field can be obtained by diminishing the distance between the drift electrodes down to less then 10 mm. As fast and slow positrons are well confined they cannot hit the drift electrodes during their way to the crystal and out of CALIPSO.

7.3.2. Proton configuration

In the case of the proton configuration the problem (and solution) is similar. The low-energy electron source must face the crystal: the electron trajectories will be similar to the magnetic field lines. Therefore if no drift is applied to the desorbed protons they will ineluctably hit the low-energy electron source, as for the low-energy positrons with the ^{22}Na source in a strong magnetic field. The applied drift and resulting low-energy proton extraction is shown in Figure 7.10.

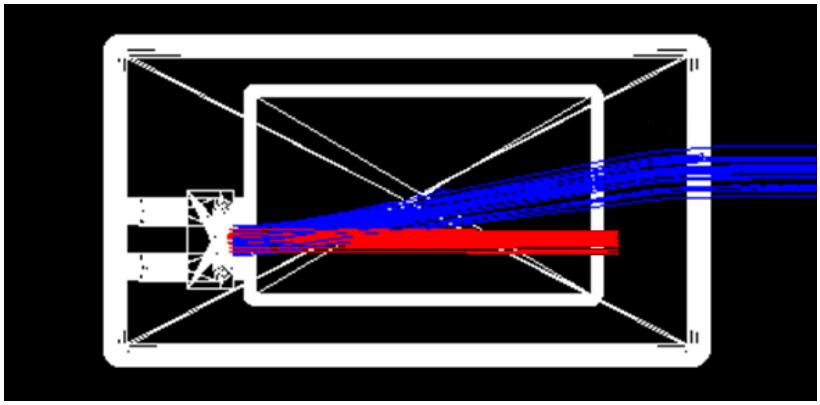

Figure 7.10. Simulation of the behavior of the proton configuration of the CALIPSO source in a strong magnetic field of 2.2 T. Low-energy electrons (red) are created (right) and hit the tungsten crystal (left). Desorbed protons (blue) are extracted by the field to the source output (right). In this configuration the acceleration potential of the CALIPSO box is $V_{\mathrm{acc}} = 400$ V, the crystal potential $V_{\mathrm{cry}} = 420$ V and the drift electrodes respectively $V_{\mathrm{Edr1}} = 540$ V and $V_{\mathrm{Edr2}} = -360$ V. The low-energy electron source is set at $V_{\mathrm{Elec}} = 540$ V.

Conclusion

Preliminary results of tests performed on the crystal holder were detailed and solutions to the few encountered problems presented. The capacity for the positron configuration of CALIPSO to compare two potentials with an accuracy of better than 10 mV was demonstrated in simulations and the corresponding measurement procedure detailed. The usage of CALIPSO in strong magnetic fields was also detailed for both its configurations. These results show that CALIPSO, using

the proposed modifications to the setup, performs better than in weak magnetic field and can fulfill its objectives: precisely compare, in-situ, two electrodes and provide a proton beam for detector characterizations without significant vacuum deterioration.

Conclusion

This thesis was dedicated to the design and realization of the *a*SPECTino spectrometer and the CALIPSO low-energy calibration source. This work is motivated by the emerging necessity to measure in-situ and with a high accuracy electrostatic potentials in proton spectroscopy experiments in free-neutron β-decay in order to reach the 10^{-4} accuracy level. The possibility to also develop a non-vacuum deteriorating low-energy proton source is an important addition for in-situ proton detector calibrations.

Simulations required for the conception and optimization of both the spectrometer and the calibration source were developed using the Geant4 libraries. Both, magnetic and electrostatic fields in those apparatuses, generated from different simulation codes, were implemented in the particle tracking in order to obtain a complete description of these systems and their behavior. These simulations are easily adaptable to different experimental conditions, such as a higher magnetic field environment.

The *a*SPECTino spectrometer, a required test setup for the development of low-energy calibration sources, is operational and offers a high modularity. Its development required the creation of many components:

- Vacuum tubing and vacuum generation and measurement,
- Resistive coils design and creation,
- Multi-channel power supply creation,
- Detection system development, optimization and characterization,
- Data analysis tools.

Experimental tests have demonstrated that noise level, detector resolution and high-voltage stability are sufficient for the detection of low-energy positrons and protons. *a*SPECTino is a complete and functional apparatus which is well-adapted to implement, optimize and characterize low-energy calibration sources.

During this thesis the initial project of developing two distinct calibration sources, one of moderated positrons and one of low-energy protons, evolved into the creation of a single apparatus, capable of emitting low-energy protons and positrons depending on its configuration: CALIPSO. The CALIPSO source revolves around two different physical processes by using the same central element: a tungsten (110) crystal. The source design is completed, as well as the creation and assembly of its mains components. Preliminary tests were performed on the tungsten crystal treatment, both in heating and cooling, and showed that several improvements should be applied for CALIPSO to perform optimally.

The work achieved during this thesis allows many tests and characterizations of CALIPSO for both its configurations. From literature and simulations one

can expect a beam of more than 10^4 moderated positrons per second in high magnetic fields with a narrow energy spread (FWHM of 30 mV) and a narrow angular spread. Simulations have shown that CALIPSO can be operated in both strong and weak magnetic field environments. Simulations have demonstrated that the moderated positron source will allow to compare electrodes in-situ with a precision of better than 10 mV within a time scale of one hour. The proton source is expected to produce around 10^4 low-energy protons per second with an energy spread of a few eV and without significant vacuum deterioration in a UHV vessel.

CALIPSO should therefore be able to fulfill its ultimate goals and to perform precise in-situ electrostatic potential comparisons and characterizations of proton detectors.

Appendix A

Data analysis program

Examples of the program interface are shown in Figures A.1 and A.2. The frame is divided into five main parts:

- **ROOT file loading and plot extraction:** the path input to open a ROOT file behaves like a Linux terminal when pressing *Tab*: it will autocomplete the path when possible and display the possibilities in the text output. The *Extract Canvas* button allows to duplicate the actual plot of the software into a separate window. This new plot is completely independent and can be modified without affecting the original one. This button can be used several times and is very practical to look at several plots at the same time.

- **Main menu and options:** on the left of the main menu is a sliding menu and the respective options are on the right. For instance the *Action* tab contains two sub-menus: *Single event* allows to look for one event (a track or a detector hit) at a time, like its position versus time, whereas *Multi event* can display variables of more than one event (like an energy spectrum). The *Option* tab contains the cuts panel where one can select what cut to apply and define each cut independently. For instance, in the Geant4 data analysis tool, one can choose to select only a defined type of particle (like e^-, e^+, γ or any selection of those) with an initial energy comprised in a defined range that hit a detector (or not). The cuts can be switched On and Off for both, *Single event* and *Multi event* plots: in case of *Single event* one can navigate directly to single events that passed all the applied cuts.

- **Text output of the software:** the text output displays information about the program behavior, for example the ROOT file path or software errors.

- **Interactive plot window:** an important functionality of the software is the plot window (named *canvas* in ROOT). All the plots are drawn inside this area and, like every ROOT canvas, it is fully interactive: one can modify axis, titles, colors, perform fits etc.

- **Status bar, progress bar and exit button:** at the bottom of the plot area stands the status bar that displays several information about the

ROOT file (like the total number of entries) and entries themselves (like the particle's type in case of a single event plot). Below is the progress bar that gives an estimation of how long is left for a plot to be created: in case of files with several millions events the plot creation is not instantaneous. Finally the *Exit* button is located at the bottom of the software frame.

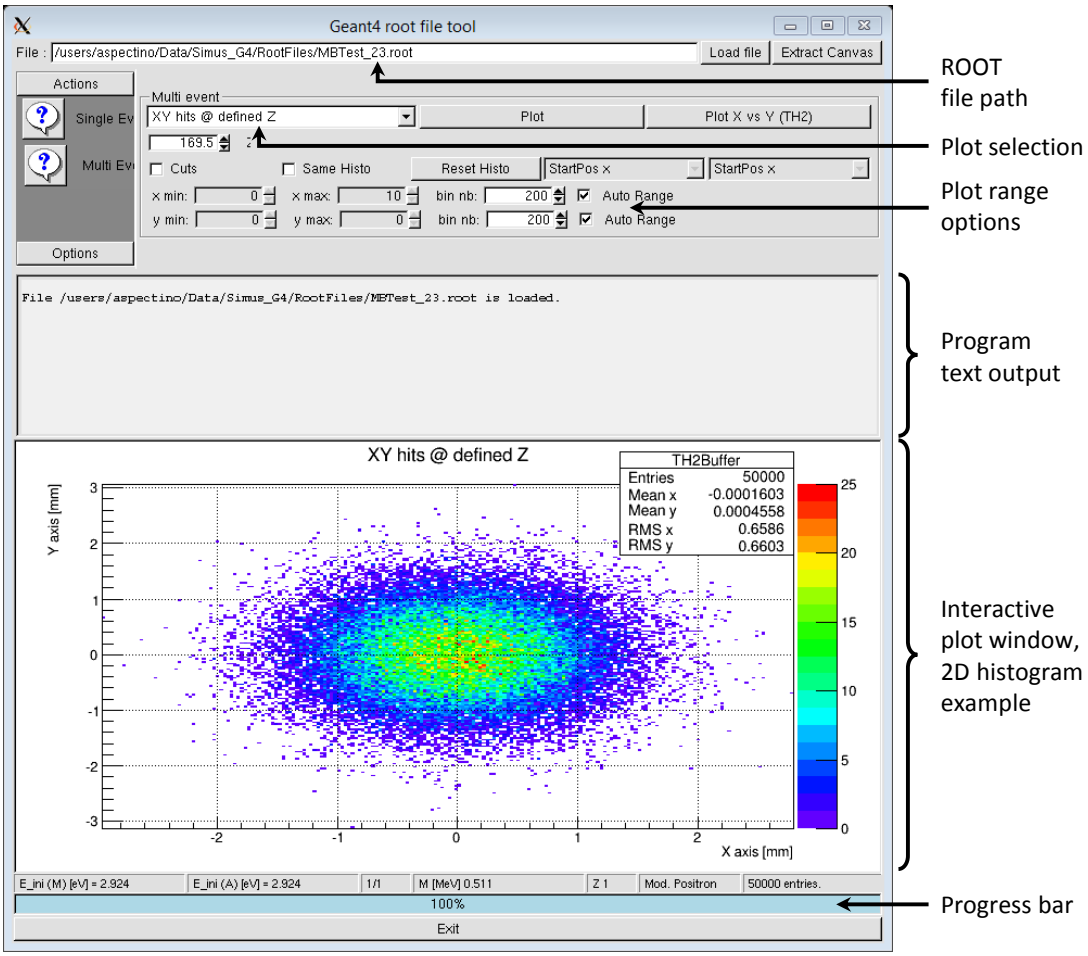

Figure A.1. First screenshot of the data analysis software. In this example a ROOT file containing the results of a simple simulation with 50,000 particles was loaded. A plot showing the hits of positrons from a point source onto a plate is displayed in the canvas part of the program.

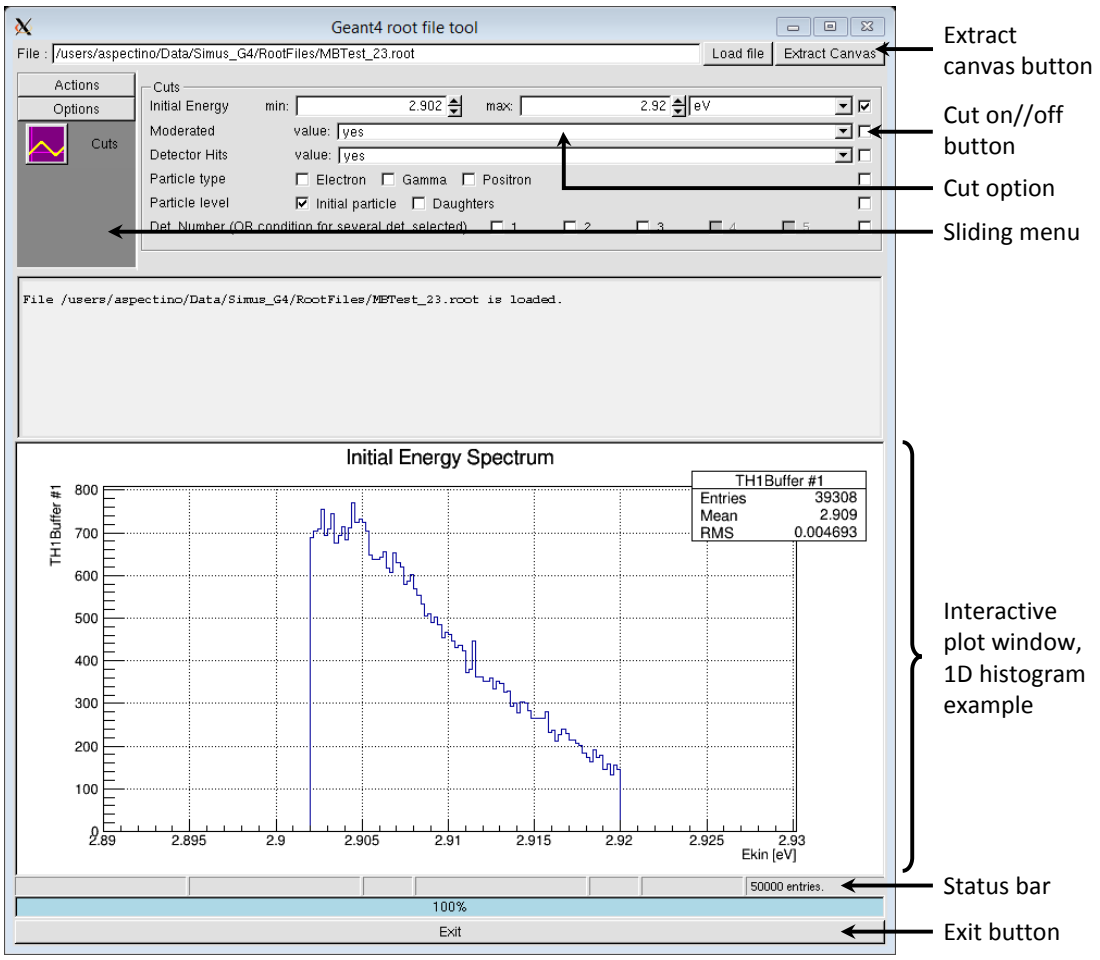

Figure A.2. Second screenshot of the data analysis software. The same file as in Figure A.1 was used and an energy cut was applied. The plot is showing the initial particle energy with the cut applied.

Appendix B

Multi-channel power supply

The *a*SPECTino spectrometer is composed of 18 coils, among which 13 require a current lower than 1.2 A. Because of the high price of commercial multi-channel power supply units, I chose to build this power supply myself. This apparatus uses bipolar transistors and operational amplifiers to deliver a current proportional to a voltage value given as an input. The electronic concept was kindly provided by Florian PIEGSA as a similar system was developed for one of his experiences. The rest of the setup (box, PCB cards design, interfacing etc.) was designed and built independently.

Design

The central concept of this apparatus is detailed in Figure B.2 with the electronic scheme of the PCB cards. OP27 operational amplifiers are used to drive the current load through bipolar transistors. The current at the output load is proportional, within the limits of the electronic components, to the input voltage given to the operational amplifier:

$$I_{\text{out}} = \frac{U_{\text{in}}}{R_{\text{L}}}, \tag{B.1}$$

with I_{out} the current at the load (i.e., the current output) in A, U_{in} the input voltage in V and R_{L} the resistivity of the load in Ω. Using Equation (B.1) and resistivity values of the coils from Table 5.2, one can get the maximum possible current with a +10/-10 V input. Measuring the potential difference at the coil leads allow to correct for the small temperatures effects on R_{L}.

This system is scaled to deliver to a 6.6 Ω load (resistivity of coils C4-C14 and C16) a maximum current of 1.2 A per channel for 12 channels and up to 1.5 A for the 4 last channels using an amplification for the input potential. Current is drawn from two commercial switched-mode power supplies of 150 W each, located on the inside of the top cover of the box, as shown in Figure B.4. A total of four $92 \times 92\times$ mm^2 fans ensure the proper cooling of the bipolar transistors, which are the main heating source of the system. The box of the apparatus, shown in Figure B.4, contains eight PCB cards with two independent channels per card, 16 channels in total, with two cards having an amplified input. Outputs consist of two banana plugs per channel, as shown in Figure B.3.

Voltage inputs are controlled from a computer using two 8 channels DAC (Digital to Analog Converter) which provides -10 V to +10 V with a 12 bit resolution and are transmitted to the apparatus through a circular connector at its back.

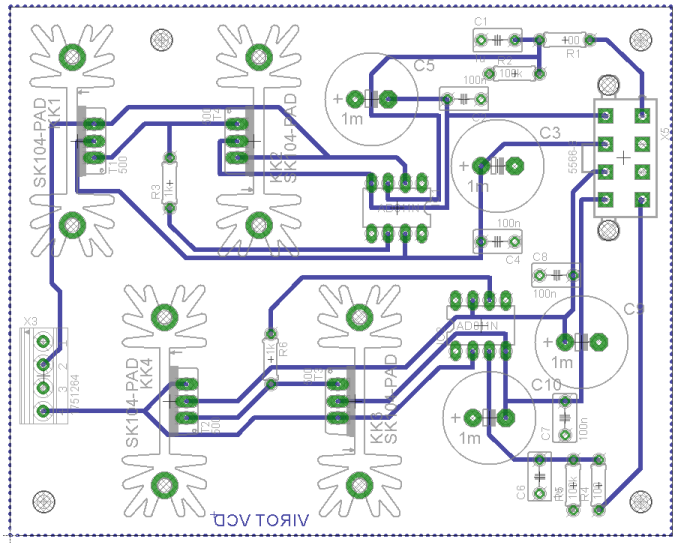

Figure B.1. Plan of a PCB card. All the PCB surface, except for the blue routes on the plan, is a ground plane. Each PCB has an eight channel Molex connector input and a four channel terminal.

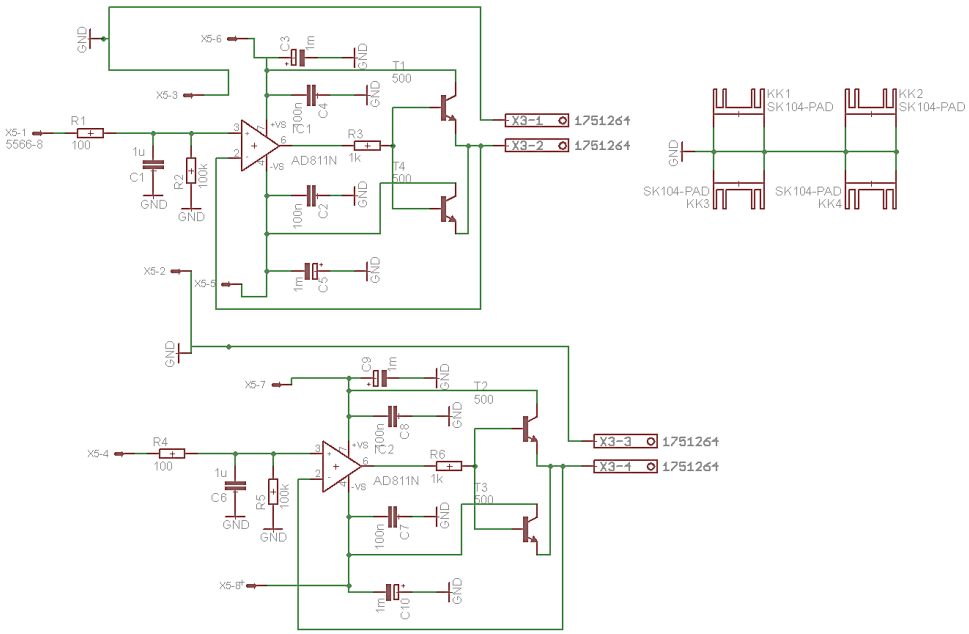

Figure B.2. Electronic scheme of the PCB cards shown in Figure B.1. Note that the bipolar transistor heat sinks are grounded (top right).

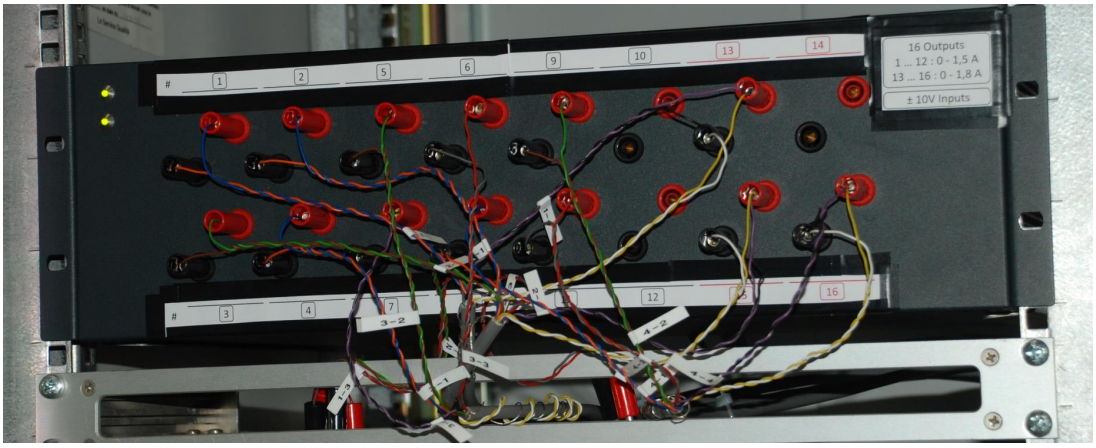

Figure B.3. Front panel of the multi-channel power supply showing the 16 channels. The two green leds (top left) indicate the status "OK" of the main switched-mode power supplies from which the current is drawn.

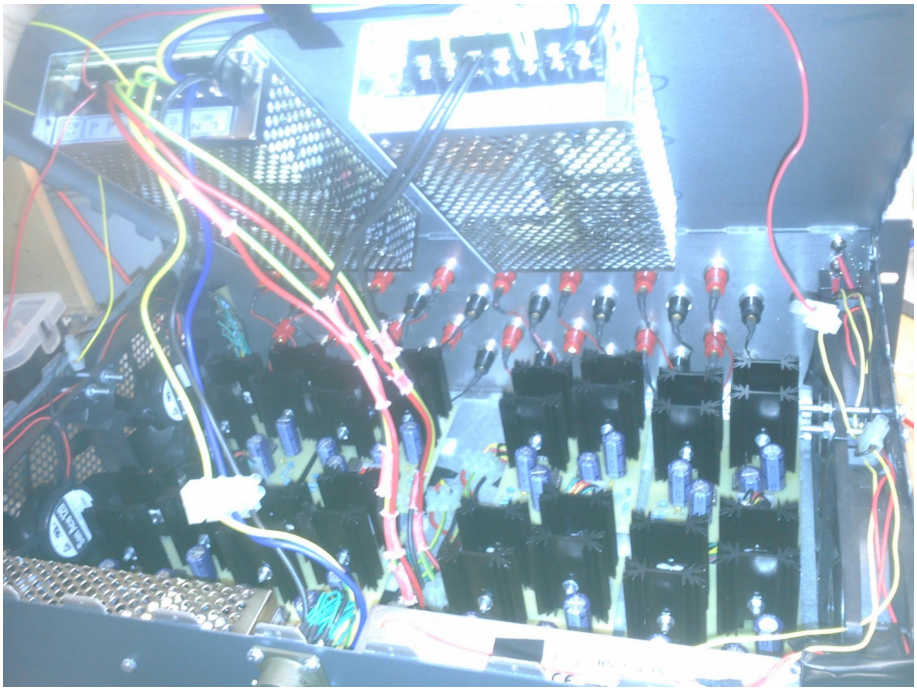

Figure B.4. Inside view of the multi-channel power supply, showing the circular connector for the potential inputs (bottom), the two switched-mode power supplies (top), cooling fans (left and right), PCB cards (center) and output connectors (in the back).

Performances

Temperature tests were performed using type-K thermocouples installed directly on a bipolar transistor heatsinks. At full load on 12 of the 16 channels, the temperature did not go higher than 51 °C, at an ambient temperature of 22 °C. Furthermore the current stability for a defined set of input voltages is very good since it does not depend on the temperature of the components. Shifts in the current value were noticed in case of a current load change on another channel. However, once the correct input voltage configuration is set, the current of each output is stable. Current ripple was also measured and ranges between 3 and 6 mA. This ripple is not problematic in this work but could be improved by just changing the two switched-mode power supplies for more stable versions. Example of the behavior of the multi-channel power supply is shown in Figure **??** for one of the amplified channels.

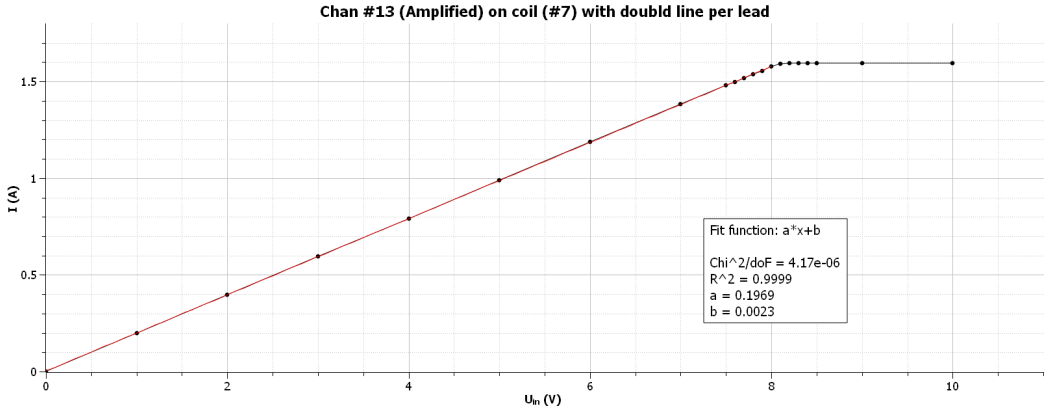

Figure B.5. Measured output of an amplified channel of the multi-channel power supply with coil C7. The linear response saturates at $U_{\text{in}} = 8$ V due to the amplification, with a corresponding current in the C7 of about 1.6 A.

Appendix C

Lead-castle for the ^{22}Na source

As discussed in Section 6.1.2.1 the 1 mCi ^{22}Na positron source emits a lot of high-energy gamma rays and should therefore be used with caution. With a dose of around 4 mSv/h at 5 cm of the capsule, both the source usage and storage have to be the safest possible for the operator.

When the source is not used in the CALIPSO source, it has to be stored in a place that must be:

- **Shielded:** As previously mentioned the source dose without any kind of protection is high and exposure to the unshielded source should be limited as much as possible. A lead shielding allows to consequently reduce the radiation level: 5 cm of Pb reduces the radiation dose coming from the source by a factor 20.

- **Locked:** The access to the source capsule has to be restricted to the authorized personnel only. It should therefore be locked in a way that no unpredicted exposure is possible, and that no one can access the source by error.

- **Adapted:** The source capsule has a 5 µm Ti window and is therefore fragile. The capsule should be stored in a way that avoids any damage. Furthermore as the CALIPSO source is designed to operate in UHV, the storage environment of the capsule should be clean.

The lead castle designed to fulfill those requirements is shown in Figure C.1. It is designed around an aluminum structure in which lead bricks are installed in a crossed assembly, so no direct view of the storage volume is possible. The shielding consists of a minimum of 10 cm of lead in all directions reducing the dose rate at its surface to less than 2 μSv/h. Because of the heavy weight of the system (more than 320 kg) it can not be moved or tilted easily and because of the way the assembly was performed, it is not possible to remove a single lead brick when the castle is closed without dismounting the aluminum structure.

As seen on Figure C.2 the top part of the castle is mounted on a rail so it can be opened. The space between the top plateau and the lead bricks below is less than a millimeter and the castle can only be open if the lock is removed, as seen in Figure C.3.

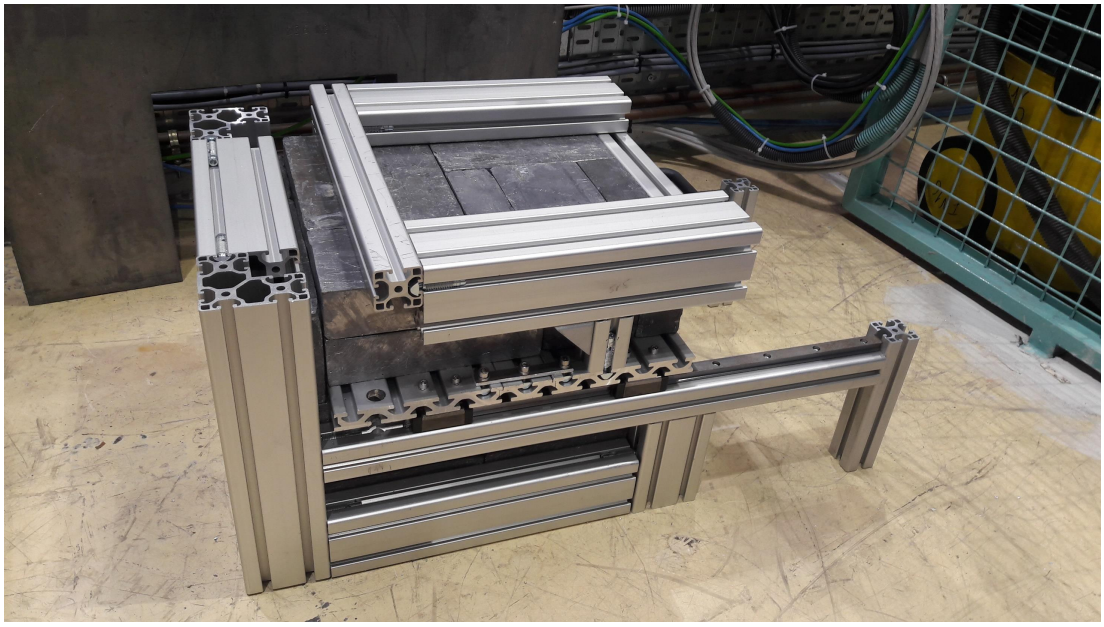

Figure C.1. External view of the closed ^{22}Na source lead castle, located in the experimental zone of the aSPECTino spectrometer. Its size is $70 \times 33 \times 38$ cm^3.

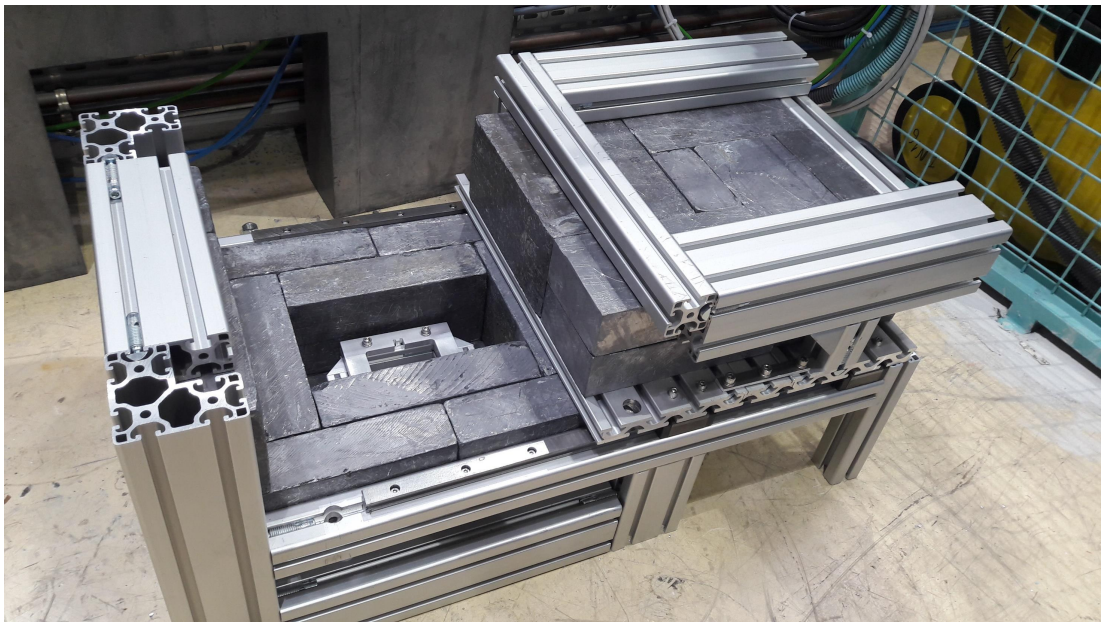

Figure C.2. View of the opened lead castle. The frame designed to hold the source capsule on its stainless steel support is in the center of the storage volume. This volume was later covered from the inside by clean aluminum foils in order to store the capsule in a way compatible with its use in UHV.

Figure C.3. Zoom on the lock of the lead castle. If the bolt is installed then the castle door cannot open at all.

As detailed in Section 6.1.2.1 the capsule is mounted on a small stainless steel bar so it can be easily installed in CALIPSO. The inside of the lead castle is designed to easily hold the source support by using a dedicated frame. In order to install and remove the ^{22}Na source safely an aluminum rod of 40 cm long, dismountable in two, is used to fix on its end the radioactive source support. As a result the operator, when taking the source from the lead castle and installing it into CALIPSO or vice-versa, is not be closer than a few tens centimeters from the source capsule.

Appendix D

Résumé en Français

D.1. Introduction

Le XX$^{\text{e}}$ siècle a vu émerger de nombreuses découvertes physiques majeures et en particulier un développement impressionnant de la physique des particules. La volonté d'identifier et de classifier les particules élémentaires et leurs intéractions a conduit à la création du Modèle Standard de la physique des particules (SM) dans les années 1960. Après plusieurs évolutions, conséquences des recherches expérimentales et théoriques, la formulation actuelle a été finalisée au milieu des années 1970. La Figure 1.1 détaille les particules élémentaires connues et leur classification au sein du SM. Bien que ce modèle soit un franc succès il est incomplet et ne peut expliquer plusieurs phénomènes cruciaux de notre univers, tels que, par exemple, l'asymétrie baryonique ou l'existence et la nature de la matière noire.

Le neutron libre est instable et décroit avec une durée de vie $\tau = 880.2 \pm 1.0$ s [P^{+}16] :

$$n \to p + e^{-} + \overline{\nu_e} + 782 \text{ keV}. \tag{D.1}$$

Cette décroissance β est une sonde pour la physique au delà du SM très populaire : c'est un système sur-contraint qui permet d'étudier le SM via différents points de vue. Ces études portent notamment sur la mesure, très précise, des coefficients de corrélation illustrés sur la Figure 1.2. Parmi ces différents coefficients, plusieurs sont reliés à la mesure directe des protons de basse énergie issus de la décroissance du neutron libre, comme l'asymétrie du proton C ou le paramètre de corrélation entre l'électron et l'antineutrino a, relié par la cinématique au spectre en énergie des protons.

D.1.1. Nécessité d'une source de calibration de positrons modérés

De part leur basse énergie ($E_{\text{k}} \leq 751$ eV), la mesure précise du spectre de recul des protons issus de la décroissance β des neutrons libres est une tâche délicate : la présence de potentiels électrostatiques indésirables altère la mesure et induit une erreur systématique. Dans le cas de l'expérience aSPECT [ZBvdG^{+}00, GBB^{+}04]

qui est dédiée à la mesure de a la différence de potentiel entre les deux electrodes assurant la sélection des protons doit être connue avec une précision de l'ordre de 7 mV (voir Figure 1.3) pour atteindre la précision de mesure attendue $\Delta a/a = 0.3\%$ [Kon11]. Les potentiels électrostatiques doivent être connus avec une précision similaire dans les expériences de prochaine génération telles que PERC ou Nab.

La détermination de ces potentiels implique la mesure de la fonction de travail électronique (eWF) des électrodes. Cette propriété de surface correspond à l'énergie nécessaire pour extraire un électron du volume de l'électrode vers le vide et implique donc un décalage entre le potentiel appliqué à l'électrode et celui subit par les particules se déplaçant à proximité de celles-ci. La fonction de travail possède de nombreuses dépendances, telles que la nature et l'orientation crystallographique de la surface, sa température, sa contamination etc. (voir Tableau 1.1 et Figure 1.4). De ce fait, il est primordial de mesurer ces potentiels directement au sein de l'éxpérience, in-situ, dans les conditions réelles de mesures.

A cet égard une source de calibration de particules chargées positivement et ayant une largeur spectrale très fine est nécessaire. Une source de positrons modérés correspond parfaitement à ces critères et permet d'obtenir un faisceau de positrons avec une faible dispersion en énergie (FWHM de quelques dizaines de meV).

D.1.2. Nécessité d'une source de calibration de protons

Beaucoup de sources de protons commerciales sont disponibles sur le marché et sont le plus souvent basées sur des technologies plasma. Ce plasma est créé à partir d'hydrogène gazeux ionisé par des électrons. De telles instruments nécéssitent un pompage différentiel et opèrent généralement entre 10^{-5} et 10^{-8} mbar. La dégradation du vide induite peut être fatale dans le cas de détecteurs semiconducteurs utilisés dans un volume UHV [Bor10]. De plus ces sources utilisent des champs électriques et/ou magnétiques forts pour confiner les électrons et maximiser la production d'ions. De ce fait ce type de technologie n'est pas adaptée aux besoins pour une source de calibration de proton dans des expériences de décroissance du neutron libre.

La Désorption Stimulée par Electrons (ESD) peut être utilisée pour créer un faisceau de faible intensité de protons de basse énergie. En recouvrant une surface bien définie avec des atomes d'hydrogène puis en les bombardant avec des électrons de basse énergie, des protons sont désorbés de la surface sans avoir recourt à un plasma ou tout autre type de confinement. La création d'un tel faisceau de proton avec une source non perturbative pourrait permettre la caractérisation des détecteurs de proton en toute sécurité et in-situ.

D.1.3. Développement des sources de calibration

Cette thèse se concentre sur deux sujets importants et complémentaires : la création d'un spectromètre pour particules chargées de basse énergie nommé aSPECTino et la création d'une source de calibration de basse énergie deux-

en-un (proton et positron) nommée CALIPSO. Le spectromètre *a*SPECTino a été conçu en premier car il était nécessaire au developpement et aux tests de la source CALIPSO. Cet instrument de trois mètres de long utilise des bobines résistives pour guider les particules chargées qui sont ensuite détectées à l'aide d'un détecteur semi-conducteur soumis à une haute-tension. Des électrodes peuvent être installées le long de la trajectoire des particules pour les sélectionner.

Concernant la source CALIPSO, le projet initial était de développer deux sources de calibration distinctes : une de positrons modérés pour scanner les champs électrostatiques au sein des instruments, et l'autre de protons de basse énergie pour caractériser les détecteurs de proton. Durant la première phase du développement des sources a émergé la possibilité de construire un seul instrument capable de créer les deux types de particules de basse énergie (protons et positrons). De ce fait la source CALIPSO a été developpée avec pour but d'émettre, de façon non simultanée, des protons et des positrons modérés avec de légères modifications. Cet instrument a également été conçu pour être compacte et le plus mobile possible.

Ce travail a été réalisé à l'Institut Laue-Langevin (ILL) à Grenoble, en France, au sein du groupe Nuclear and Particle Physics. Les Chapitres 2 et 3 présentent les concepts physiques utilisés pour la création des protons et positrons de basse energie avec CALIPSO. Le Chapitre 4 détaille la structure des simulations qui ont été utilisées pour développer à la fois le spectromètre *a*SPECTino et la source CALIPSO. Le concept, design et les caractéristiques d'*a*SPECTino et de CALIPSO sont présentées respectivement dans le Chapitre 5 et 6 tandis que le Chapitre 7 décrit les différentes caractérisations qui devraient être faites de la source CALIPSO. Enfin les Appendices A à C détaillent plusieurs éléments techniques de ce travail : le programme pour l'analyse des données, l'alimentation multi-canaux et le château de plomb pour la source ^{22}Na.

D.2. La désorption stimulée par électrons (ESD)

La Désorption Stimulée par Electrons (ESD) est un phénomène qui a été découvert au début du XX^{e} siècle [Dem18, Ter37] mais qui n'a suscité un engouement scientifique qu'à partir des années 60. Ce processus permet la désorption de fragments neutres ou ionisés via le bombardement d'espèces adsorbées par des électrons de basse énergie ($E \leq 500$ eV).

Ce chapitre est dédié à la description de l'ESD et se concentre sur les aspects concernant l'utilisation de ce phénomène pour former un faisceau de protons de basse énergie. Des informations détaillées sur l'ESD et plus globalement les DIET (Desorption Induite par des Transitions Electroniques) peuvent être trouvées dans des revues telles que [TTTM83, RY91, Age94].

D.2.1. Le modèle MGR

Ce modèle, nommé d'après ces auteurs Menzel, Gomer et Redhead, a vu le jour en 1964 et décrit les phénomènes d'excitation par électron unique [Red64, MG64b, MG64a].

La désorption induite par les électrons de basse énergie est la conséquence d'une excitation électronique de la liaison d'adsorption. Le modèle MGR utilise des approximations adiabatiques et fournit une description de l'ESD semi-classique et à une dimension. Le système adsorbat(A)-métal(M) est d'abord considéré dans son état de repos, noté (M+A). Suite à une interaction avec un électron de basse énergie incident, le système subit une transition Franck-Condon (FC) vers un état excité. L'interprétation semi-classique de la transition FC assume que le mouvement nucléaire peut être négligé durant la période d'excitation qui dure environ 10^{-15} s. L'état excité resultant peut être :

- **Antiliant :** $(\mathrm{M} + \mathrm{A})^{\mathrm{a}}$
- **Métastable :** $(\mathrm{M} + \mathrm{A})^{*}$
- **Ionique :** $(\mathrm{M}^{-} + \mathrm{A}^{+})$

Une représentation schématique de l'état au repos et des trois états excités possibles par rapport à z la distance au delà de la surface est montrée sur la Figure 2.1a avec z_0 le centre de la position d'équilibre de la configuration dans l'état au repos. L'approximation adiabatique implique que le système est d'abord électroniquement excité puis survient le mouvement nucléaire sur une période d'environ 10^{-13} s. Ce mouvement converti l'énergie potentielle en énergie cinétique et, en fonction de l'état excité, peut conduire à la libération d'un adsorbat (i.e., désorption). Le passage d'une courbe à l'autre sur la Figure 2.1a correspond à un processus Auger ou à un effet tunnel avec la mer d'électrons du substrat. Ainsi l'excitation du système (M+A) peut conduire à la désorption d'un adsorbat neutre (excité ou pas) ou ionique, mais aussi, par désexcitation et reneutralisation, au même état de repos.

Le modèle MGR ne décrit pas l'ensemble des nombreux systèmes d'ESD possibles mais est adapté pour le système utilisé dans ce travail : l'hydrogène sur un substrat de tungstène (110).

D.2.2. L'hydrogène sur du tungstène (110)

Le bombardement par des électrons de basse énergie d'hydrogène sur un monocrystal de tungstène (110) (H/W(110)) peut émettre des protons et ce en utilisant, dans des conditions comparables, le même crystal que pour l'émission de positrons de basse énergie, comme décrit dans les Chapitres 3 et 6.

Les différents sites d'adsorption possibles sur le tungstène (110) sont indiqués sur la Figure 2.2b. Dans le cas du système H-W(110) la molécule de dihydrogène approche préférentiellement la surface près d'un site "Top" et les atomes d'hydrogène sont adsorbés préférentiellement sur les sites "Threefold Hollow" [BM08]. L'adsorption chimique dissiociative du dihydrogène sur du tungstène (110) est un processus exothermique (i.e., favorable énergétiquement) et peut conduire à la désorption de protons une fois bombardé d'électrons de basse énergie. Durant la désorption le taux de protons désorbés diminue avec la couvertue en hydrogène de la surface. Le taux de protons désorbés initiallement sert alors de référence pour estimer l'efficacité du processus de désorption. Le taux de proton désorbés, lors d'un bombardement électronique constant, augmente fortement si

le processus d'adsorption est réalisé à une température inférieure à 160 K, comme indiqué sur la Figure 2.3a [ZWG93].

Les Figures 2.3a et 2.3b montrent ainsi qu'il est préférable de réaliser l'adsorption de l'hydrogène sur un cristal de tungstène (110) propre et froid jusqu'à atteindre la saturation pour maximiser le taux de protons désorbés par ESD.

De plus il existe un phénomène de seuil quant à l'énergie des électrons de basse énergie incidents : l'énergie minimum requise pour induire une désorption dépend du système et de l'état du fragment désorbé (neutre ou ionique). Dans le cas du tungstène (110) cette valeur seuil est d'environ 15 eV et une valeur d'environ 40 eV permet de maximiser l'efficacité de désorption des protons (i.e., le nombre de protons désorbés par électron incident), comme indiqué sur la Figure 2.4.

Les ions issus de l'ESD ont une énergie de quelques eV et une largeur spectrale qui dépend des charactéristiques de la liaison adsorbat-substrat. Dans le cas des protons emis par l'ESD du système H-W(110), la dispersion en énergie est de l'ordre de quelques eV, comme indiqué sur la Figure 2.6a. La dispersion angulaire des ions issus d'adsorbats monoatomiques est relativement bien définie (FWHM d'environ 20°) et suit un profil Gaussien centré sur la normale de la surface, comme indiqué sur la Figure 2.6b. Cette distribution est légèrement affectée par la température du système, avec une dispersion angulaire plus faible pour un système à plus basse température.

Bien que l'ESD produise principalement des fragments neutres (la désorption d'ions représente environ 1% de l'ensemble des désorptions) la faible section efficace du processus conduit à une dégradation complètement négligeable d'un vide de qualité UHV [ZWG93]. En assumant une intensité nomimale de CALIPSO d'environ 10^4 protons par seconde et les conditions expérimentales typiques du spectromètre *a*SPECTino, la désorption neutre du système H-W(110) ne devrait pas impacter de facon significative la qualité du vide du spectromètre, comme détaillé dans la Section 6.1.3.1.

D.3. Les positrons dans la matière

L'antimatière a été prédite à partir de l'équation de Dirac [Dir28, Dir31] et en 1933 Carl Anderson détecte pour la première fois un positron [And33] : un anti-électron. De part leur nature d'antimatière et leur charge positive, les positrons sont très sensibles aux défauts présents dans la matière et peuvent intéragir de nombreuses façons avec la surface d'un solide, faisant d'eux une sonde très prisée en physique des surfaces. C'est seulement à partir des années 1970 que les positrons ont été couramment utilisés pour sonder la matière condensée grâce à la possibilité de créer des faisceaux mono-énergétique intenses de positrons. La configuration positron de CALIPSO est basée sur les mêmes concepts, détaillés dans ce chapitre, que ceux utilisés pour créer ces faisceaux.

D.3.1. Propriétés et création des positrons

Le théorème CPT implique que la masse, le temps de vie, le rapport gyromagnétique et l'amplitude de charge du positron sont identiques à ceux de l'électron,

avec le signe de la charge étant opposé [CH05]. Le positron est donc un lepton dont les propriétés sont listées dans le Tableau 3.1.

Les positrons peuvent être créés par différents processus : soit par production de pair soit à l'aide d'une source radioactive beta. Dans ce dernier cas une décroissance β^+ convertit un proton en un neutron, un positron et un antineutrino électronique, comme par exemple : $^{22}\mathrm{Na} \longrightarrow {}^{21}\mathrm{Ne} + \mathrm{e}^+ + \nu_\mathrm{e}$. Les isotopes radioactifs β^+ courants et leur propriétés sont listés dans le Tableau 3.2.

D.3.2. Intéractions des positrons dans le métal

Les intéractions des positrons dans un solide diffèrent d'avec celles des électrons en de nombreux points et principalement à cause de leur différence de charge.

Quand un faisceau de positrons frappe une surface, une partie est réflechie. Cette rétrodiffusion dépend, pour un solide semi-infini, de l'énergie des positrons incidents et du numéro atomique Z des constituants du solide, comme décrit sur la Figure 3.2. A l'instar des électrons, les positrons peuvent aussi diffuser sur les atomes du matériau.

Bien que les positrons s'annihilent avec des électrons, la section efficace d'annihilation est cinq à six ordres de grandeur plus petite que celle de diffusion [JR76] et l'échelle de temps typique pour la diffusion ou la diffraction des positrons est de l'ordre de 10^{-15} s.

Les positrons très énergétiques (de l'ordre du MeV) perdent leur énergie principalement via le rayonnement Bremsstrahlung. A des niveaux d'énergies intermédiaires ($E \leq 100$ keV) la diffusion inélastique par excitation des électrons de coeur et de valence domine. A partir de quelques dizaines d'eV, les excitations plasmoniques puis les excitations électrons-trous prennent le dessus. A l'approche des énergies thermales (quelques dixièmes d'eV) les positrons se thermalisent en diffusant avec les phonons [PC70].

Le profil d'implantation des positrons dans la matière peut être décrit en utilisant un profil Makhovien [Mak60] :

$$P(z) = \frac{m z^{m-1}}{z_0^m} \exp\left(-\left(\frac{z}{z_0}\right)^m\right), \tag{D.2}$$

avec z la profondeur d'implantation et m un paramètre sans dimension qui dépend du matériau. z_0 est défini tel que :

$$z_0 = \frac{A}{\rho \cdot \Gamma\left(1 + 1/m\right)} E^n, \tag{D.3}$$

avec A et n des paramètres qui dépendent du matériau, ρ la densité du matériau implanté en g/cm^3, Γ la fonction gamma et E l'énergie initiale des positrons en keV. Des exemples de profils Makhoviens pour l'implantation de positrons dans le tungstène sont indiqués sur la Figure 3.3.

De part leur charge positive, les positrons de basse-énergie ont une grande probabilité de se retrouver piégés dans une région de potentiel inférieur induit par un défaut du réseau, ce qui conduit inévitablement à une annihilation avec un électron. Pour qu'un positron thermalisé puisse diffuser vers la surface du

solide il faut donc une densité de défaut au sein du réseau qui soit la plus faible possible.

D.3.3. La ré-émission de positrons modérés

Sous certaines circonstances, les positrons peuvent être ré-émis d'un matériau, nommé modérateur, avec une énergie faible et très bien définie et une faible dispersion angulaire. Ce processus est spécifique aux positrons et permet de créer des faisceaux monochromatiques et lumineux de positrons de basse-énergie. La configuration positron de CALIPSO est basée sur ce processus.

Afin de décrire ce processus en détail il faut tout d'abord introduire la notion de fonction de travail. La fonction de travail correspond à l'énergie minimum qu'il faut fournir pour pouvoir extraire une particule depuis le volume d'un matériau vers le vide (à plus de 10 nm de la surface) [Kit04]. Cette propriété de surface est définie telle que :

$$\phi_{\mp} = \pm D - \mu_{\mp}, \tag{D.4}$$

avec $\phi_{\mp}$ la fonction de travail électronique ou positronique, D la valeur de la barrière surfacique dipolaire et $\mu_{\mp}$ le potentiel chimique électronique ou positronique. La Figure 3.6 détaille les potentiels électroniques et positroniques à proximité de l'interface solide/vide et les fonctions de travail résultantes. Si D est suffisamment grand alors la fonction de travail positronique peut être négative : si un positron de basse-énergie diffuse près de l'interface solide-vide, il sera alors ré-émis depuis le solide vers le vide.

Une conséquence directe de cette définition de la fonction de travail est sa dépendance aux propriétés surfaciques, que ce soit l'orientation crystallographique, les contaminations ou même la température [Kie86, IK01], comme indiqué sur la Figure 1.4. Les valeurs des fonctions de travail électroniques et positroniques pour des modérateurs de positrons typiques sont listés dans la Table 3.3.

Afin de quantifier la probabilité qu'un positron ayant pénétré un modérateur soit ré-émis en tant que positron modéré par la fonction de travail, nous pouvons définir l'éfficacité telle que :

$$\epsilon = \frac{N_{\text{reem}}}{N_{\text{inc}}} \tag{D.5}$$

avec N_{reem} le nombre de positrons modérés ré-émis et N_{inc} le nombre de positrons incidents ayant frappés le modérateur. L'éfficacité possède de nombreuses dépendances, telle que la source primaire de positrons, la géométrie (voir Figure 3.7) ou encore la qualité et la nature du modérateur.

Pour un modérateur métallique mono-cristallin, propre et à température ambiante, la dispersion en énergie des positrons modérés ré-émis est de l'ordre de 75 meV [FLG86]. Cette valeur est la conséquence de la distribution thermale des positrons ré-émis : si on réduit la température du modérateur alors on réduit aussi la dispersion en énergie des positrons ré-émis, comme indiqué sur la Figure 3.8.

La source CALIPSO se base sur un crystal de tungstène (110) pour modérer des positrons issus d'une source β^+ et créer un faisceau de positrons de basse-énergie

avec une dispersion angulaire et énergétique très faible.

D.4. Simulations Geant4

La création du spectromètre *a*SPECTino et de la source CALIPSO a nécéssité de nombreuses simulations afin de vérifier la viabilité de leur conception ainsi que pour optimiser ces deux appareils. Pour ce faire les librairies Geant4 ont été utilisées ainsi que différents logiciels de simulation pour calculer les cartes de champ électromagnétique du système.

D.4.1. Structure des simulations Geant4

Geant4 est un code orienté objet en C++ libre d'accès qui utilise les méthodes Monte Carlo afin de simuler les traces de particules et leur intéractions à travers la matière. Etant donné la faible énergie des particules qui nous intéressent la liste physique PENELOPE à été utilisée pour traiter les intéractions électromagnétiques de 1 GeV à 100 eV. Lorsqu'une particule évolue à travers un champ électromagnétique sa trajectoire se propage à l'aide d'un *stepper* (voir Figure 4.3), en l'occurence un Runge-Kutta à l'ordre 4.

Un évènement primaire inclut la trace initiale créée par l'utilisateur et toutes les traces secondaires résultantes, comme indiqué sur la Figure 4.4. Les traces sont alors créées et traitées selon la règle "dernière arrivée première sortie".

La géométrie du système est importée directement depuis SolidWorks vers Geant4 grâce à la librairie CADMESH qui utilise le format STL pour intégrer les géométries, même complexe, au sein du traceur, comme dans l'exemple décrit sur la Figure 4.5.

Les nombreuses informations issues des simulations sont stockées dans un fichier, comme indiqué sur la Figure 4.6.

D.4.2. Intégration des champs électromagnétiques

Geant4 ne pouvant pas calculer de champs électromagnétiques complexes par lui-même, il est nécessaire d'utiliser des programmes annexes. Plusieurs solutions sont alors possibles : soit de calculer directement la valeur du champ en chaque point requis au fur et à mesure de la simulation, soit d'utiliser une grille précalculée à partir de laquelle la valeur du champ en chaque point est rapidement extrapolée. Cette dernière solution offre en elle-même deux approches distinctes, à savoir l'utilisation de grilles structurées ou non-structurées.

Dans ce travail le choix a été fait de travailler avec des cartes de champs précalculées : structurée pour le champ magnétique et non-structurée pour le champ électrique.

Une carte structurée offre plusieurs avantages. Elle permet en effet de déterminer très rapidement dans quelle cellule se situe le point étudié et l'interpolation qui s'en suit peut être réalisée sans effort conséquent. On peut également utiliser une grille à géométrie adaptive si besoin. Néanmoins si la carte est très inhomogène alors il devient très complexe et fastidieux de gérer les différentes tailles

de cellules. De plus ce type de méthode pose problème quand il s'agit de calculer et interpoler un champ à la bordure d'un objet dont les contours sont aussi les conditions limites pour la simulation (comme par exemple un objet métallique pour le calcul du champ électrostatique). Ce problème est illustré sur la Figure 4.7 et peut être résolu en utilisant des cartes non-structurées.

Le champ magnétique du système est calculé grâce au logiciel RADIA et est calculé sur l'ensemble du spectromètre *a*SPECTino sur une grille de $160 \times 160 \times 2700$ mm^3 avec des cellules de $1 \times 1 \times 1$ mm^3, pour un total d'environ 70 millions de points. Le champ électrostatique est quant à lui calculé à l'aide du logiciel COMSOL Multiphysics et exporté en suivant la grille non-structurée utilisée par ce programme, comme montré sur la Figure 4.8.

Afin de déterminer dans quelle cellule de la carte non-structurée du champ électrique se trouve un point, la structure de données "CellTree" a été utilisée [GJ10]. Cette structure permet d'éviter les problèmes typiques de duplication des cellules (voir Figure 4.13) en utilisant des doubles séparations, comme détaillé sur la Figure 4.14. Une fois la cellule pertinente trouvée une interpolation tri-linéaire est alors réalisée, comme indiqué sur la Figure 4.15.

D.4.3. Processus de réémission des positrons modérés

La ré-émission de positrons modérés grâce à la fonction de travail positronique négative de certains matériaux n'est pas intégrée dans Geant4. Afin de simuler ce processus une approche statistique à été implémentée. On peut ainsi modéliser à l'aide d'une équation 1D la possibilité pour un positron modéré de diffuser (ou pas) vers la surface d'un matériau en fonction de son lieu d'implatation comme suit :

$$f = e^{-a/L_{+\text{red.}}}, \tag{D.6}$$

avec f la fraction de positrons implantés à la profondeur a qui vont diffuser vers la surface du modérateur et $L_{+\text{red.}}$ la longueur de diffusion réduite ($L_{+\text{red.}} \approx 17$ nm pour le tungstène et pour une telle approximation 1D [KL09, W$^+$15]).

Au sein de la simulation Geant4, les positrons sont suivis jusqu'à leur thermalisation puis, pour les positrons ayant pu diffuser jusqu'à la surface du modérateur, ils sont ré-émis avec une énergie qui suit une distribution de Maxwell-Boltzmann.

D.4.4. Programme d'analyse des données

Les données issues des simulations sont stockées dans des fichiers ROOT qui peuvent ensuite être analysés à l'aide d'un programme, lui aussi développé en C++ avec les librairies ROOT, disposant d'une interface graphique. Ce programme, dont la fenêtre principale est visible sur la Figure 4.17, permet d'analyser également les données réelles issues du spectromètre *a*SPECTino et est détaillé plus en détail dans l'Annexe A.

D.5. Le spectromètre *a*SPECTino

Afin de développer et d'optimiser la source CALIPSO il a été nécessaire de construire un banc de test : le spectromètre *a*SPECTino. *a*SPECTino est un Filtre MAC-E qui permet de sélectionner et de détecter des particules chargées de basse-énergie.

D.5.1. Filtre MAC-E

Un Filtre MAC-E utilise des champs électromagnétiques pour sélectionner des particules chargées avec une fonction de transmission très piquée. Un gradient magnétique négatif transfère l'énergie cinétique des particules vers leur composante longitudinale (i.e., parallèle au champ magnétique) puis une barrière de potentiel, nommé Plan d'Analyse (AP), les sélectionne. Les particules ayant surpassées cette barrière sont concentrées sur un détecteur sous haute tension à l'aide d'un champ magnétique intense. Le spectre intégré peut alors être mesuré en faisant varier le potentiel de sélection.

Dans le spectromètre *a*SPECTino la source de calibration est située au niveau de la croix de la source (voir la Figure 5.1) où règne un champ magnétique d'environ 16 mT. Les particules de basse-énergie (protons ou positrons) sont alors guidées à l'aide du champ magnétique vers l'AP qui est une région avec une champ magnétique de faible intensité (environ 3.5 mT). Une électrode cylindrique peut être installée à l'AP pour créer un potentiel de sélection. Les particules ayant pu traverser cette barrière sont alors accélerées par la haute tension du détecteur (jusqu'à -30 kV). Elles sont détectées à l'aide d'un détecteur semi-conducteur. Le signal résultant est alors amplifié et digitalisé par le système d'acquisition du spectromètre.

D.5.2. Description du spectromètre

Le spectromètre, montré sur la Figure 5.4 et schématisé sur la Figure 5.6, a été construit et utilisé dans la zone "*a*SPECT" de l'Institut Laue-Langevin, dans le hall neutron ILL7, à côté de l'instrument IN16b.

La chambre à vide de l'instrument est séparée en deux parties : la croix Source, dotée de nombreuses traversées, et la partie détecteur qui contient le système de détection. Afin d'obtenir un vide de qualité UHV, le spectromètre est équipé de deux pompes turbo-moléculaires et peut être chauffé dans son ensemble jusqu'à environ 150 °C.

Le champ magnétique est créé à l'aide de 18 bobines résistives installées à l'extérieur du tube à vide. Deux bobines de Maxwell (voir Figure 5.7) sont utilisées pour créer des zones de champ magnétique homogène au niveau de la source et de l'AP. Le champ magnétique le long de l'axe principal du spectromètre est présenté sur la Figure 5.8 et les caractéristiques des différentes bobines sont regroupées sur le Tableau 5.2.

D.5.3. Système de détection

Comme indiqué sur la Figure 5.12 le détecteur est monté sur une bride au bout d'un séparateur en céramique permettant d'appliquer une différence de potentiel entre le spectromètre et le détecteur jusqu'à 60 kV. Le détecteur par défaut du spectromètre est une diode PIN de la marque CANBERRA, utilisée à température ambiante. Ce détecteur silicium possède une fenêtre d'entrée en aluminium de moins de 50 nm et possède une surface active de $50\,\mathrm{mm}^2$.

L'ensemble de l'électronique du détecteur est également soumis à la haute tension et est confiné dans une boite en plexiglas à l'arrière du spectromètre. Cet ensemble est composé d'un préamplificateur ORTEC 142A, situé au plus près du détecteur, d'un amplificateur ORTEC 570 et enfin d'un ADC CAEN V1724 (voir Figure 5.14).

Le système de détection à été calibré à l'aide d'une source radioactive de ^{133}Ba qui décroit par capture électronique. La source étant scellée dans du plastique, seuls les photons peuvent en sortir et être détectés. Le spectre résultant d'une simulation Geant4 de l'énergie déposée dans le détecteur par une telle source est montrée sur la Figure 5.15 tandis que le spectre acquis à l'aide d'*a*SPECTino et de la source est présenté sur la Figure 5.16.

La calibration résultante indique qu'une haute tension d'environ -25 kV est amplement suffisante pour séparer le signal issu de protons (ou de positrons) de basse-énergie du bruit électronique du système de détection, comme indiqué sur la Figure 5.17.

D.6. La source CALIPSO

CALIPSO est à la fois l'acronyme de CALIbration Positron SOurce et de CALIbration Proton SOurce. Cette source a pour but de pouvoir émettre soit des protons de basse-énergie soit des positrons modérés en ne changeant que très légèrement le système. L'élément central de CALIPSO est un cristal de tungstène (110) de haute pureté (99.999%) poli avec une granularité inférieure à 0.01 μm. Le concept de la source, basé sur les méthodes décrites dans les Chapitres 2 et 3, est de soit :

- Bombarder le cristal (propre et froid) avec des positrons issus d'une source radioactive β^+ pour créer un faisceau de positrons modérés de basse-énergie.
- Déposer une mono-couche d'hydrogène sur le cristal (propre et froid) puis de le bombarder avec des électrons de basse-énergie pour créer un faisceau de protons de basse-énergie grâce à l'ESD.

Dans chacune des configurations le cristal doit en premier lieu être nettoyé et recuit sous vide, directement dans le spectromètre. La procédure de nettoyage est décrite en détail dans la Section 7.1.2 et requiert de chauffer le cristal à une température d'environ 1900 °C. Un support complexe pour le cristal a été créé pour réaliser le chauffage et le refroidissement du cristal et permettre le bon fonctionnement de la source dans ses deux configurations.

D.6.1. Conception de la source

Le système CALIPSO est contenu dans une boîte modulaire de $60 \times 60 \times 80$ mm^3 en aluminium et inox 316 montrée sur la Figure 6.1. Le cristal est situé dans son support dédié à l'arrière de la boîte, comme montré sur les Figures 6.1 et 6.2. Entre le cristal et la sortie de la source se tiennent plusieurs composants : les deux électrodes de dérivation, le capillaire pour l'arrivée du gaz, la source de positron ^{22}Na et la source d'électrons de basse-énergie. Une fois les particules de basse-énergie créées et extraites de CALIPSO elles sont accélérées par la différence de potentiel entre CALIPSO et le potentiel du spectromètre. L'ensemble des connections requises pour faire fonctionner CALIPSO est listée dans le Tableau 6.1.

La Figure 6.4 schématise le fonctionnement de la source dans sa configuration positron. Les positrons rapides émis par la source radioactive bombardent le cristal de tungstène. Une partie des positrons frappant le cristal est alors thermalisée, diffuse près de la surface du cristal et est ré-émise par la fonction de travail positronique négative du tungstène. Ces positrons sont extraits de la source à l'aide d'un champ $\mathbf{E} \times \mathbf{B}$ créé par les deux électrodes de dérive.

La source primaire de positrons est une source ^{22}Na d'environ 1 mCi contenue dans une capsule en titane décrite sur la Figure 6.6. Un peu moins de deux positrons sur trois sortent de la capsule après avoir été créés. Une simulation du champ électrique de dérive créé par les deux électrodes $\mathbf{E} \times \mathbf{B}$ est visible sur la Figure 6.7 et le drift induit sur la Figure 6.8.

Dans sa configuration proton, les éléments de CALIPSO sont identiques à ceux de la configuration positron à l'exception de la source de positron primaire qui est remplacée par une source d'électrons de basse-énergie. Etant donné la faible intensité du champ magnétique qui règne au sein d'*a*SPECTino les protons de basse-énergie issus de CALIPSO ne peuvent pas être complètement confinés. Ainsi seuls les protons qui sont émis parallèles ou presque aux lignes de champ magnétique du spectromètre ont une chance de pouvoir atteindre le détecteur. Comme les protons émis par ESD sont émis préférentiellement normaux à la surface du cristal, si on assume une distribution angulaire conservatrice (FHWM = 20°) alors les simulations montrent que plus de 65% des protons désorbés atteignent le détecteur d'*a*SPECTino.

D.6.2. Support du cristal

Le support du cristal est une pièce critique de CALIPSO. Il est composé de nombreuses petite pièces fragiles et doit subvenir à différents besoins :

- **Refroidissement du cristal de tungstène :** Comme décrit précédemment l'adsorption d'hydrogène sur le cristal de tungstène (110) doit être réalisée à basse température pour maximiser la production de protons par ESD. De plus la dispersion en énergie du faisceau de positrons modérés est directement liée à la température du modérateur.

- **Chauffage rapide du cristal :** Les deux configurations de CALIPSO nécéssitent un cristal de tungstène propre pour pouvoir opérer dans de

bonnes conditions. La procédure de nettoyage du cristal requiert de chauffer le cristal de tungstène jusqu'à 1900 °C.

- **La rotation du cristal :** La rotation du cristal autour de l'axe détaillé sur la Figure 6.2 permet d'ajuster l'angle du cristal indépendamment de la boîte de CALIPSO. Elle permet aussi de réduire la charge thermique par radiation sur la source radioactive ^{22}Na lorsque le recuit du cristal est réalisé.

La Figure 6.10 présente une vue éclatée du support du cristal de CALIPSO. Le support du cristal est fixé à la structure de CALIPSO avec un axe rotatif contrôlé par un moteur piezo-électrique.

Le cristal est refroidi à l'aide de la source froide. Il s'agit d'un bloc de cuivre situé dans le volume sous vide du spectromètre à travers lequel passe directement du LN_2. Une tresse en cuivre, fixée sur ce bloc, rejoint ensuite l'arrière du support du cristal et permet ainsi d'évacuer la chaleur de CALIPSO.

Un bombardement électronique est utilisé pour chauffer le cristal. Une cathode chaude, émettant des électrons, est située derrière le cristal. En mettant le crystal à un potentiel de +2 kV par rapport à la cathode chaude, les électrons émis par la source sont accélérés vers le cristal et le frapper, le chauffant alors très rapidement. La température du cristal est monitorée grâce à un thermocouple type C, découplé du potentiel du cristal à l'aide une fine céramique possédant une bonne conduction thermique, comme détaillé sur la Figure 6.13.

D.7. Résultats et perspectives

Des tests prélimaires ont été réalisés sur plusieurs éléments de la source CALIPSO et les résultats attendus de la source, notamment pour comparer des potentiels électrostatiques, ont été dérivés à partir des simulations.

D.7.1. Tests préliminaires du support du cristal

Ces tests ont été effectués en installant le support du cristal seul au sein du spectromètre *a*SPECTino et ont été dédiés au refroidissement et au chauffage du cristal et de son support. L'installation de ce système est visible sur la Figure 7.1.

Pour refroidir le cristal un flux constant d'azote (liquide ou gazeux) a été mis en place dans la ligne prévue à cet effet. Comme indiqué sur la Figure 7.2 la température de la partie arrière du support du cristal est descendu, au plus bas, a environ 200 K. Cette température, supérieure aux attentes, peut s'expliquer par diverses raisons, comme un mauvais contact thermique entre la tresse en cuivre et les deux blocs en cuivre (respectivement sur la ligne de LN_2 et sur le support du cristal) ou encore un trop fort rayonnement thermique du spectromètre sur le support du cristal. Des solutions à ce problèmes ont été mises en place et nécéssitent d'être testées. Néanmoins le fonctionnement de CALIPSO, que ce soit en configuration proton ou positron, n'est pas fortement impacté par une telle température de refroidissement (voir Chapitres 2 et 3).

La procédure de nettoyage et de recuit du cristal est détaillée sur la Figure 7.4. Afin de pouvoir chauffer le cristal par bombardement électronique il est nécessaire d'utiliser une source de courant pouvant fournir plusieurs centaines de mA avec un potentiel d'environ 2 kV. Une telle source n'ayant pu être disponible lors de ces tests, le chauffage du cristal n'a pu être testé dans son intégralité et seule la cathode chaude, sans potentiel d'accélération, a pu être étudiée (voir les Figures 7.5, 7.6 et 7.7).

D.7.2. Procédure pour la comparaison des potentiels

Une des principales sources de motivation pour la création de la source de positron modérés est la comparaison de potentiels électrostatiques avec une précision $\leq$ 10 mV. Une simulation a été réalisée pour estimer la précision qui peut être atteinte ainsi. La simulation se compose du spectromètre *a*SPECTino et de la source CALIPSO. Une électrode cylindrique est installée au niveau de l'AP du spectromètre et seuls les positrons ayant une énergie suffisante peuvent traverser cette barrière et être comptés avec le détecteur. Le potentiel d'accélération de CALIPSO peut être varié pour ainsi scanner cette barrière de potentiel.

La simulation est découpée en deux étapes : un premier scan est réalisé pour une valeur donnée de la barrière de potentiel puis on refait ce scan mais cette fois-ci en appliquant un potentiel plus élevé de 10 mV. Les simulations ont été faites avec une température théorique du cristal de tungstène de 200 K avec 50k positrons par point de mesure pour un total de 600k positrons modérés. Les résultats de cette simulation sont visibles sur le Tableau 7.1. En intégrant le bruit de fond typique pour ce genre d'expérience (environ 0.1 Hz), on arrive a déterminer cette différence de potentiel entre les deux mesures avec une précision bien meilleure que 10 mV :

$$b1 = 176.757(1)\ \text{V},$$
$$b2 = 176.767(1)\ \text{V},$$

avec $b1$ et $b2$ le résultat respectif de l'analyse des deux configurations de potentiel.

En utilisant un tel résultat et les spécificités d'un spectromètre comme *a*SPECT, on peut alors estimer qu'il suffit de seulement quelques heures pour déterminer avec précision la différence de potentiel entre deux électrodes sur l'ensemble de la région d'intérêt (voir Figure 7.9).

D.7.3. Comportement sous champ magnétique intense

Afin d'utiliser la source CALIPSO dans une expérience de spectroscopie du proton, la source doit être adaptée pour les champs magnétiques intenses. Dans le cas du spectromètre *a*SPECT la source opérera dans un champ magnétique de 2.2 T. Dans un tel environnement les protons de basse-énergie et les positrons de haute-énergie sont bien confinés.

Pour la configuration positron le principal avantage est le confinement des positrons de haute-énergie émis par la source ^{22}Na. En installant la source de positrons primaire à plusieurs centimètres du cristal de tungstène (mais dans sa ligne de vue directe) le taux de positrons créés qui atteignent le cristal est grandement augmenté et donc la quantité de positroins modérés ré-émis également. Il faut néanmoins augmenter fortement le champ électrique de dérive pour permettre une extraction correcte des positrons.

Dans sa configuration proton le problème ainsi que la solution sont similaires. La source d'électrons de basse-énergie doit faire face au cristal : les trajectoires des électrons seront superposées avec les lignes du champ magnétique. De ce fait le champ de dérive pour les protons désorbés est nécessaire afin qu'ils évitent la source d'électrons et soient extraits de CALIPSO. Les trajectoires simulées des électrons de basse-énergie ainsi que les protons désorbés sont visibles sur la Figure 7.10.

D.8. Conclusion

Cette thèse a été dédiée au design et à la réalisation du spectromètre *a*SPECTino et de la source de calibration de basse énergie CALIPSO. Ce travail est motivé par la nécéssité de mesurer, in-situ et avec une grande précision, les potentiels électrostatiques au sein des expériences de spectroscopie du proton dans la décroissance du neutron libre afin d'atteindre un niveau de précision de l'ordre de 10^{-4}. La possibilité de développer également une source de protons de basse énergie ne dégradant pas la qualité du vide est un atout important pour la calibration in-situ des détecteurs de protons.

Les simulations requises pour la conception et l'optimisation à la fois du spectromètre et de la source de calibration ont été dévelopées à l'aide des librairies Geant4. Les champs magnétiques et électriques de ces instruments ont été générés grâce à différents codes de simulations puis implémentés dans le *particle tracking* afin d'obtenir une description complète du système et de son comportement. Ces simulations sont facilement adaptables aux différentes conditions expérimentales, comme un fort champ magnétique par exemple.

Le spectromètre *a*SPECTino, un banc de test requis pour le développement des sources de calibration de basse énergie, est opérationnel et offre une grande modularité. Son développement a requis la création de nombreux composants :

- Tube à vide, génération et mesure du vide,
- Design et création des bobines résistives,
- Création d'une alimentation multi-canaux,
- Développement, optimisation et caractérisation du système de détection,
- Outils d'analyse de données.

Les tests expérimentaux ont démontrés que le bruit de fond, la résolution du détecteur et la stabilité de la haute-tension suffisent pour assurer la détection de positrons et de protons de basse énergie. *a*SPECTino est un instrument complet et fonctionnel qui est adapté à l'utilisation, l'optimisation et la caractérisation des sources de calibration de basse énergie.

Durant cette thèse le project initial qui consistait à développer deux sources de calibrations distinctes, une de positrons modérés et une autre de protons de basse énergie, a évolué pour donner lieu à la création d'un seul instrument, nommé CALIPSO, capable d'émettre des protons et des positrons de basse énergie en fonction de sa configuration. La source CALIPSO a été conçue autour de deux processus physiques différents utilisant le même élément central : un cristal de tungstène (110). Le design de la source est défini et ses principaux composants ont été créés et assemblés. Des tests préliminaires concernant le traitement du cristal de tungstène (en chauffage et en refroidissement) ont été effectués et ont montrés que plusieurs améliorations devraient être mises en place afin que CALIPSO puisse opérer de façon optimale.

Le travail réalisé durant cette thèse permet de nombreux tests et caractérisations de CALIPSO dans ses deux configurations. En se basant sur la littérature et les simulations on peut attendre de la source un faisceau de plus de 10^4 positrons par seconde dans un champ magnétique fort ainsi qu'une faible dispersion en énergie (FWHM de 30 mV) et une faible dispersion angulaire. Les simulations ont démontrées que CALIPSO pouvait être utilisée dans des champs magnétiques faibles et forts et que la source de positrons modérés va permettre de comparer les potentiels d'électrodes in-situ avec une précision meilleure que 10 mV et avec une échelle de temps de l'ordre de l'heure. La source de proton devrait produire environ 10^4 protons de basse énergie par seconde avec une largeur spectrale de quelques eV et sans déterioration notable du vide pour un système UHV.

CALIPSO devrait donc être capable d'atteindre ses buts ultimes et comparer précisément et in-situ les potentiels électrostatiques ainsi que caractériser les détecteurs de protons.

Bibliography

[A+01] Q. R. Ahmad et al. Measurement of the rate of ed→ppe-interactions produced by B8Solar Neutrinos at the Sudbury Neutrino Observatory. *Physical Review Letters*, 87(7), jul 2001.

[A+02] Q. R. Ahmad et al. Direct evidence for neutrino flavor transformation from neutral-current interactions in the Sudbury Neutrino Observatory. *Physical Review Letters*, 89(1), jun 2002.

[A+03] S. Agostinelli et al. Geant4—a simulation toolkit. *Nuclear Instruments and Methods in Physics Research Section A: Accelerators, Spectrometers, Detectors and Associated Equipment*, 506(3):250–303, jul 2003.

[A+09] I. Antcheva et al. ROOT — A C framework for petabyte data storage, statistical analysis and visualization. *Computer Physics Communications*, 180(12):2499–2512, dec 2009.

[A+12] G. Aad et al. Observation of a new particle in the search for the standard model higgs boson with the ATLAS detector at the LHC. *Physics Letters B*, 716(1):1–29, sep 2012.

[A+13] M. Aguilar et al. First result from the alpha magnetic spectrometer on the international space station: Precision measurement of the positron fraction in primary cosmic rays of 0.5–350 GeV. *Physical Review Letters*, 110(14), apr 2013.

[Abe08] H Abele. The neutron. Its properties and basic interactions. *Progress in Particle and Nuclear Physics*, 60(1):1–81, jan 2008.

[Age94] V.N. Ageev. Desorption induced by electronic transitions. *Progress in Surface Science*, 47(1-2):55–203, sep 1994.

[AHB+97] M. Arnold, G. Hupfauer, P. Bayer, L. Hammer, K. Heinz, B. Kohler, and M. Scheffler. Hydrogen on W(110): an adsorption structure revisited. *Surface Science*, 382(1-3):288–299, jun 1997.

[And33] Carl D. Anderson. The positive electron. *Physical Review*, 43(6):491–494, mar 1933.

[Ant80] Peter R. Antoniewicz. Model for electron- and photon-stimulated desorption. *Physical Review B*, 21(9):3811–3815, may 1980.

[B+69a] E. D. Bloom et al. High-energy inelastic e-p Scattering at 6 degrees and 10 degrees. *Physical Review Letters*, 23(16):930–934, oct 1969.

[B+69b] M. Breidenbach et al. Observed behavior of highly inelastic electron-proton scattering. *Physical Review Letters*, 23(16):935–939, oct 1969.

[B+07] A. Badertscher et al. Improved limit on invisible decays of positronium. *Physical Review D*, 75(3), feb 2007.

[Bas15] M. Shamsuzzoha Basunia. Nuclear data sheets for A = 22. *Nuclear Data Sheets*, 127:69–190, jul 2015.

[Ben75] Jon Louis Bentley. Multidimensional binary search trees used for associative searching. *Communications of the ACM*, 18(9):509–517, sep 1975.

[Bla08] Jean Blachot. Nuclear data sheets for A = 107. *Nuclear Data Sheets*, 109(6):1383–1526, jun 2008.

[BM08] H. Fabio Busnengo and Alejandra E. Martínez. H_2 Chemisorption on W(100) and W(110) surfaces. *The Journal of Physical Chemistry C*, 112(14):5579–5588, apr 2008.

[Bor10] Michael Borg. *The electron antineutrino angular correlation coefficient a in free neutron decay: Testing the standard model with the aSPECT-spectrometer*. PhD thesis, Johannes Gutenberg-Universität, 2010.

[BPT80] G Beamson, H Q Porter, and D W Turner. The collimating and magnifying properties of a superconducting field photoelectron spectrometer. *Journal of Physics E: Scientific Instruments*, 13(1):64–66, jan 1980.

[C+12] S. Chatrchyan et al. Observation of a new boson at a mass of 125 GeV with the CMS experiment at the LHC. *Physics Letters B*, 716(1):30–61, sep 2012.

[Ca16] Hui Chen and al. Progress towards a laser produced relativistic electron-positron pair plasma. *Journal of Physics: Conference Series*, 688:012010, mar 2016.

[CB96] M. Cacciatore and G. D. Billing. Dissociation and atom recombination of H2 and D2 on metallic surfaces: A theoretical survey. *Pure and Applied Chemistry*, 68(5), jan 1996.

[CDM90] K. F. Canter, C. B. Duke, and A. P. Mills. *Ten Years of Low Energy Positron Diffraction*, pages 183–211. Springer Berlin Heidelberg, Berlin, Heidelberg, 1990.

[CEC98] Oleg Chubar, Pascal Elleaume, and Joel Chavanne. A three-dimensional magnetostatics computer code for insertion devices. *Journal of Synchrotron Radiation*, 5(3):481–484, 1998.

[CER17a] CERN. Root home webpage. https://root.cern.ch, 2014/2017.

[CER17b] CERN. The large hadron collider webpage. https://home.cern/topics/large-hadron-collider, 2017.

[CGFE79] J. E. Cunningham, D. Greenlaw, C. P. Flynn, and J. L. Erskine. Adsorbate spectra on metal and oxide surfaces. *Physical Review Letters*, 42(5):328–331, jan 1979.

[CGH13] Vincenzo Cirigliano, Susan Gardner, and Barry R. Holstein. Beta decays and non-standard interactions in the LHC era. *Progress in Particle and Nuclear Physics*, 71:93–118, jul 2013.

[CH05] M. Charlton and J. W. Humberston. *Positron Physics*. Cambridge University Press, October 2005.

[Cha32] J. Chadwick. Possible existence of a neutron. *Nature*, 129(3252):312–312, feb 1932.

[CLPW56] Bruce Cork, Glen R. Lambertson, Oreste Piccioni, and William A. Wenzel. Antineutrons produced from antiprotons in charge-exchange collisions. *Phys. Rev.*, 104:1193–1197, Nov 1956.

[CMY99] Andrzej Czarnecki, Kirill Melnikov, and Alexander Yelkhovsky. α^2 Corrections to parapositronium decay. *Physical Review Letters*, 83(6):1135–1138, aug 1999.

[Col16] Geant4 Collaboration. Geant4 user's guide for application developers. https://geant4.web.cern.ch/geant4/UserDocumentation/UsersGuides/ForApplicationDeveloper/html/, 2016.

[CRM13] Vincenzo Cirigliano and Michael J. Ramsey-Musolf. Low energy probes of physics beyond the standard model. *Progress in Particle and Nuclear Physics*, 71:2–20, jul 2013.

[CSWY55] Owen Chamberlain, Emilio Segrè, Clyde Wiegand, and Thomas Ypsilantis. Observation of antiprotons. *Phys. Rev.*, 100:947–950, Nov 1955.

[Dem18] A. J. Dempster. A new method of positive ray analysis. *Physical Review*, 11(4):316–325, apr 1918.

[DH08] Jerzy Dryzek and Paweł Horodek. GEANT4 simulation of slow positron beam implantation profiles. *Nuclear Instruments and Methods in Physics Research Section B: Beam Interactions with Materials and Atoms*, 266(18):4000–4009, sep 2008.

[Dir28] P. A. M. Dirac. The quantum theory of the electron. *Proceedings of the Royal Society of London. Series A, Containing Papers of a Mathematical and Physical Character*, 117(778):610–624, 1928.

[Dir31] P. A. M. Dirac. Quantised singularities in the electromagnetic field. *Proceedings of the Royal Society A: Mathematical, Physical and Engineering Sciences*, 133(821):60–72, sep 1931.

[Dir78] P. A. M. Dirac. The 1st h. r. crane lecture, 1978.

[EB64] F. Englert and R. Brout. Broken symmetry and the mass of gauge vector mesons. *Physical Review Letters*, 13(9):321–323, aug 1964.

[F+98] Y. Fukuda et al. Evidence for oscillation of atmospheric neutrinos. *Physical Review Letters*, 81(8):1562–1567, aug 1998.

[fEI17] National Centers for Enviromental Information. World magnetic model website. https://www.ngdc.noaa.gov/geomag/WMM/DoDWMM.shtml, 2017.

[FGL85] W. E. Frieze, D. W. Gidley, and K. G. Lynn. Positron-beam-brightness enhancement: Low-energy positron diffraction and other applications. *Physical Review B*, 31(9):5628–5633, may 1985.

[FKNM12] Peter Ferrin, Shampa Kandoi, Anand Udaykumar Nilekar, and Manos Mavrikakis. Hydrogen adsorption, absorption and diffusion on and in transition metal surfaces: A DFT study. *Surface Science*, 606(7-8):679–689, apr 2012.

[FLG86] D. A. Fischer, K. G. Lynn, and D. W. Gidley. High-resolution angle-resolved positron reemission spectra from metal surfaces. *Physical Review B*, 33(7):4479–4492, apr 1986.

[FMM+13] Y Fukaya, M Maekawa, I Mochizuki, K Wada, T Hyodo, and A Kawasuso. Reflection high-energy positron diffraction: the past 15 years and the future. *Journal of Physics: Conference Series*, 443:012068, jun 2013.

[FT97] F.R. Feito and J.C. Torres. Inclusion test for general polyhedra. *Computers & Graphics*, 21(1):23–30, jan 1997.

[Gar67] Milan Wayne Garrett. Thick cylindrical coil systems for strong magnetic fields with field or gradient homogeneities of the 6th to 20th order. *Journal of Applied Physics*, 38(6):2563–2586, may 1967.

[GBB+04] F. Glück, S. Baeßler, J. Byrne, M. G. D. van der Grinten, F. J. Hartmann, W. Heil, I. Konorov, G. Petzoldt, Yu. Sobolev, and O. Zimmer. The neutron decay retardation spectrometer aSPECT: Electromagnetic design and systematic effects. *The European Physical Journal A*, 23(1):135–146, nov 2004.

[GH06] Marcus A. Gagliardi and A.W. Hunt. Monte Carlo simulations of slow-positron production from normal and glancing incident targets. *Nuclear Instruments and Methods in Physics Research Section B: Beam Interactions with Materials and Atoms*, 245(2):355–362, apr 2006.

[GHK64] G. S. Guralnik, C. R. Hagen, and T. W. B. Kibble. Global conservation laws and massless particles. *Physical Review Letters*, 13(20):585–587, nov 1964.

[GJ10] Christoph Garth and Kenneth I Joy. Fast, memory-efficient cell location in unstructured grids for visualization. *IEEE Transactions on Visualization and Computer Graphics*, 16(6):1541–1550, nov 2010.

[GM64] M. Gell-Mann. A schematic model of baryons and mesons. *Physics Letters*, 8(3):214–215, feb 1964.

[GM86] E. M. Gullikson and A. P. Mills. Positron dynamics in rare-gas solids. *Physical Review Letters*, 57(3):376–379, jul 1986.

[GMCB85] E. M. Gullikson, A. P. Mills, W. S. Crane, and B. L. Brown. Absence of energy loss in positron emission from metal surfaces. *Physical Review B*, 32(8):5484–5486, oct 1985.

[GR70] R.L. Gerlach and T.N. Rhodin. Binding and charge transfer associated with alkali metal adsorption on single crystal nickel surfaces. *Surface Science*, 19(2):403–426, feb 1970.

[GVW14] S. Golge, B. Vlahovic, and B. Wojtsekhowski. High-intensity positron microprobe at the thomas jefferson national accelerator facility. *Journal of Applied Physics*, 115(23):234907, jun 2014.

[HA87] J. W. Humberston and E. A. G. Armour, editors. *Atomic Physics with Positrons*. Springer US, 1987.

[Hay09] W. M. Haynes. *CRC handbook of chemistry and physics: a ready-reference book of chemical and physical data*. CRC Press, 2009.

[Hay16] W.M. Haynes. *CRC Handbook of Chemistry and Physics, 97th Edition*. CRC Press, 2016.

[HCWS86] S M Hutchings, P G Coleman, R N West, and R J Stone. A low-distortion slow positron filter. *Journal of Physics E: Scientific Instruments*, 19(4):282–283, apr 1986.

[Her11] Klaus Hermann. *Crystallography and Surface Structure*. Wiley-VCH Verlag GmbH & Co. KGaA, feb 2011.

[HFG08] D. Hanneke, S. Fogwell, and G. Gabrielse. New measurement of the electron magnetic moment and the fine structure constant. *Phys. Rev. Lett.*, 100:120801, Mar 2008.

[Hig64] Peter W. Higgs. Broken symmetries and the masses of gauge bosons. *Physical Review Letters*, 13(16):508–509, oct 1964.

[HL78] Jeffrey L. Hock and David Lichtman. Electron stimulated desorption of negative ions from gases adsorbed on molybdenum. *Surface Science*, 77(1):L184–L186, oct 1978.

[HM82] J. E. Houston and Theodore E. Madey. Core-level processes in the electron-stimulated desorption of CO from the W(110) surface. *Physical Review B*, 26(2):554–566, jul 1982.

[HSS02] C. Hugenschmidt, B. Straßer, and K. Schreckenbach. Investigation of positron work function and moderation efficiency of Ni, Ta, Pt and W(100). *Applied Surface Science*, 194(1-4):283–286, jun 2002.

[I+11] Vladimir Ivanchencko et al. Recent improvements in Geant4 electromagnetic physics models and interfaces. *Progress in Nuclear Science and Technology*, 2(0):898–903, oct 2011.

[IK01] Kh. I. Ibragimov and V. A. Korolkov. Temperature dependence of the work function of metals and binary alloys. *Inorganic Materials*, 37(6):567–572, 2001.

[Jac98] John David Jackson. *Classical Electrodynamics*. John Wiley & Sons Inc, 1998.

[JR76] J. M. Jauch and F. Rohrlich. *The Theory of Photons and Electrons*. Springer Nature, 1976.

[K+12] G Konrad et al. Neutron decay with PERC: a progress report. *Journal of Physics: Conference Series*, 340(1):012048, 2012.

[Kaj10] Khaled Kaja. *Development of nano-probe techniques for work function assessment and application to materials for microelectronics*. Theses, Université Joseph-Fourier - Grenoble I, June 2010.

[KCS+90] R. Khatri, M. Charlton, P. Sferlazzo, K. G. Lynn, A. P. Mills, and L. O. Roellig. Improvement of rare-gas solid moderators by using conical geometry. *Applied Physics Letters*, 57(22):2374–2376, nov 1990.

[KF78] M. L. Knotek and Peter J. Feibelman. Ion desorption by core-hole Auger decay. *Physical Review Letters*, 40(14):964–967, apr 1978.

[KF79] M.L. Knotek and Peter J. Feibelman. Stability of ionically bonded surfaces in ionizing environments. *Surface Science*, 90(1):78–90, dec 1979.

[Kie86] A. Kiejna. On the temperature dependence of the work function. *Surface Science*, 178(1-3):349–358, dec 1986.

[Kit04] C. Kittel. *Introduction to Solid State Physics*. Wiley, 2004.

[KL09] W. J. Kossler and S. S. Long. Positron production at JLab simulated using Geant4. *AIP Conference Proceedings*, 1160(1):133–137, 2009.

[Kon11] Gertrud Emilie Konrad. *Measurement of the proton recoil spectrum in neutron beta decay with the spectrometer aSPECT : study of systematic effects*. PhD thesis, Johannes Gutenberg-Universität, 2011.

[KRBT+05] R. Krause-Rehberg, V. Bondarenko, E. Thiele, R. Klemm, and N. Schell. Determination of absolute defect concentrations for saturated positron trapping – deformed polycrystalline Ni as a case study. *Nuclear Instruments and Methods in Physics Research Section B: Beam Interactions with Materials and Atoms*, 240(3):719–725, nov 2005.

[KRK11] Yu. Khazov, A. Rodionov, and F.G. Kondev. Nuclear data sheets for A = 133. *Nuclear Data Sheets*, 112(4):855–1113, apr 2011.

[KTV74] V.A. Kuzminikh, I.A. Tsekhanovski, and S.A. Vorobiev. Backscattering of positrons from thick targets. *Nuclear Instruments and Methods*, 118(1):269–271, jun 1974.

[L+86] J. Lahtinen et al. High-intensity variable-energy positron beam for surface and near-surface studies. *Nuclear Instruments and Methods in Physics Research Section B: Beam Interactions with Materials and Atoms*, 17(1):73–80, aug 1986.

[Lid00] David R. Lide. *A Century of Excellence in Measurements, Standards, and Technology*. 2000.

[LY94] Jong-Liang Lin and J. T. Yates. Electron gun for producing a low energy, high current, and uniform flux electron beam. *Journal of Vacuum Science & Technology A: Vacuum, Surfaces, and Films*, 12(5):2795–2797, sep 1994.

[Mad73] Theodore E. Madey. Chemisorption of H2 on W(100): Absolute sticking probability, coverage, and electron stimulated desorption. *Surface Science*, 36(1):281–294, apr 1973.

[Mad80] Theodore E. Madey. The role of steps and defects in electron stimulated desorption: Oxygen on stepped W(110) surfaces. *Surface Science*, 94(2-3):483–506, apr 1980.

[Mad94] Theodore E Madey. History of desorption induced by electronic transitions. *Surface Science*, 299-300:824–836, jan 1994.

[Mai14] Romain Maisonobe Maisonobe. *Measurement of the angular correlation coefficient a between electron and antineutrino in neutron beta-decay with the spectrometer aSPECT*. Theses, Université de Grenoble, February 2014.

[Mak60] AF Makhov. Sur la pénétration des électrons dans les corps solides. *Sou. Phys. St. Sol*, 2:1934, 1960.

[Men95] Dietrich Menzel. Thirty years of MGR: How it came about, and what came of it. *Nuclear Instruments and Methods in Physics Research Section B: Beam Interactions with Materials and Atoms*, 101(1-2):1–10, jun 1995.

[MG64a] Dietrich Menzel and Robert Gomer. Desorption from metal surfaces by low-energy electrons. *The Journal of Chemical Physics*, 41(11):3311–3328, dec 1964.

[MG64b] Dietrich Menzel and Robert Gomer. Desorption from surfaces by slow-electron impact. *The Journal of Chemical Physics*, 40(4):1164–1165, feb 1964.

[Mor66] G.M. Morton. A computer oriented geodetic database and a new technique in file sequencing. 1966.

[MPMH92] J Makinen, S Palko, J Martikainen, and P Hautojarvi. Positron backscattering probabilities from solid surfaces at 2-30 keV. *Journal of Physics: Condensed Matter*, 4(36):L503–L508, sep 1992.

[MPSY08] I. N. Meshkov, V. N. Pavlov, A. O. Sidorin, and S. L. Yakovenko. Testing of a cryogenic source of slow monochromatic positrons. *Physics of Particles and Nuclei Letters*, 5(2):92–93, mar 2008.

[MSG+11] Jason L. McLain, Ann L. Sprague, Gregory A. Grieves, David Schriver, Pavel Travinicek, and Thomas M. Orlando. Electron-stimulated desorption of silicates: A potential source for ions in mercurys space environment. *Journal of Geophysical Research*, 116(E3), mar 2011.

[MW05] Werner Martienssen and Hans Warlimont, editors. *Springer Handbook of Condensed Matter and Materials Data*. Springer Berlin Heidelberg, 2005.

[MYKU70] Theodore E. Madey, John T. Yates, David A. King, and Carole J. Uhlaner. Isotope effect in electron stimulated desorption: Oxygen chemisorbed on tungsten. *The Journal of Chemical Physics*, 52(10):5215–5220, may 1970.

[NGS10] Caroline D. Nesaraja, Scott D. Geraedts, and Balraj Singh. Nuclear data sheets for A = 58. *Nuclear Data Sheets*, 111(4):897–1092, apr 2010.

[oM17] University of Michigan. Positron research website. http://positrons.physics.lsa.umich.edu/nanopos/PALS-intro/psitronphysics.htm, 2017.

[OP49] A. Ore and J. L. Powell. Three-photon annihilation of an electron-positron pair. *Physical Review*, 75(11):1696–1699, jun 1949.

[P+08] Christian Piochacz et al. A positron remoderator for the high intensity positron source NEPOMUC. *Applied Surface Science*, 255(1):98–100, oct 2008.

[P+09] Dinko Počanić et al. Nab: Measurement principles, apparatus and uncertainties. *Nuclear Instruments and Methods in Physics Research Section A: Accelerators, Spectrometers, Detectors and Associated Equipment*, 611(2-3):211–215, dec 2009.

[P+16] C. Patrignani et al. Review of Particle Physics. *Chin. Phys.*, C40:100001, 2016.

[PC70] A. Perkins and J. P. Carbotte. Effect of the positron-phonon interaction on positron motion. *Physical Review B*, 1(1):101–107, jan 1970.

[PCTL12] C. M. Poole, I. Cornelius, J. V. Trapp, and C. M. Langton. A CAD interface for GEANT4. *Australasian Physical & Engineering Sciences in Medicine*, 35(3):329–334, sep 2012.

[PN94] M. J. Puska and R. M. Nieminen. Theory of positrons in solids and on solid surfaces. *Reviews of Modern Physics*, 66(3):841–897, jul 1994.

[Red64] P. A. Redhead. Interaction of slow electrons with chemisorbed oxygen. *Canadian Journal of Physics*, 42(5):886–905, may 1964.

[Rei08] Martin Reiser. *Theory and Design of Charged Particle Beams*. Wiley-VCH Verlag GmbH & Co. KGaA, mar 2008.

[Rut11] E. Rutherford. LXXIX.the scattering of and particles by matter and the structure of the atom. *Philosophical Magazine Series 6*, 21(125):669–688, may 1911.

[RY91] R.D. Ramsier and J.T. Yates. Electron-stimulated desorption: Principles and applications. *Surface Science Reports*, 12(6-8):246–378, jan 1991.

[SBP+04] T Soldner, L Beck, C Plonka, K Schreckenbach, and O Zimmer. New limit on t violation in neutron decay. *Physics Letters B*, 581(1-2):49–55, feb 2004.

[Sch85] D. M. Schrader. *SLO85*, (166), 1985.

[Sig14] Adrian Signer. Low-energy precision physics and the high-energy frontier. *Physics Procedia*, 51:25–30, 2014.

[Sim10] M. Simson. *Measurement of the electron antineutrino angular correlation coefficient a with the neutron decay spectrometer aSPECT.* PhD thesis, 2010.

[Sin07] Balraj Singh. Nuclear data sheets for A = 64. *Nuclear Data Sheets*, 108(2):197–364, feb 2007.

[SL88] Peter J. Schultz and K. G. Lynn. Interaction of positron beams with surfaces, thin films, and interfaces. *Rev. Mod. Phys.*, 60:701–779, Jul 1988.

[SOMSC10] J A Sillero, D Ortega, E Muñoz-Serrano, and E Casado. An experimental study of thoriated tungsten cathodes operating at different current intensities in an atmospheric-pressure plasma torch. *Journal of Physics D: Applied Physics*, 43(18):185204, May 2010.

[SSG+13] K. Sudarshan, S. N. Samarin, P. Guagliardo, V. N. Petrov, A. H. Weiss, and J. F. Williams. Angle-resolved energy distribution of re-emitted positrons from a W(100) single crystal. *Physical Review B*, 87(8), feb 2013.

[SW77] S. Sayyid and E.M. Williams. Threshold behaviour in the process of electron stimulated desorption. *Surface Science*, 62(2):431–454, feb 1977.

[Ter37] A.N. Terenin. page 149, 1937.

[TTTM83] Norman H. Tolk, Morton M. Traum, John C. Tully, and Theodore E. Madey, editors. *Desorption Induced by Electronic Transitions DIET I.* Springer Berlin Heidelberg, 1983.

[Tul96] J.K. Tuli. Evaluated nuclear structure data file. *Nuclear Instruments and Methods in Physics Research Section A: Accelerators, Spectrometers, Detectors and Associated Equipment*, 369(2-3):506–510, feb 1996.

[VLSE83] A. Vehanen, K. G. Lynn, Peter J. Schultz, and M. Eldrup. Improved slow-positron yield using a single crystal tungsten moderator. *Applied Physics A Solids and Surfaces*, 32(3):163–167, nov 1983.

[W+11] J. Wolf et al. Investigation of turbo-molecular pumps in strong magnetic fields. *Vacuum*, 86(4):361 – 369, 2011.

[W+15] A. I. Williams et al. Moderation and diffusion of positrons in tungsten meshes and foils. *Journal of Applied Physics*, 118(10):105302, sep 2015.

[WCW+07] Y. C. Wu, Y. Q. Chen, S. L. Wu, Z. Q. Chen, S. J. Wang, and R. G. Greaves. High moderation efficiency positron beamline. *physica status solidi (c)*, 4(10):4032–4035, sep 2007.

[Wei02] Ch. Weinheimer. KATRIN, a next generation tritium decay experiment in search for the absolute neutrino mass scale. *Progress in Particle and Nuclear Physics*, 48(1):141–150, jan 2002.

[Wik16] Wikipedia. Guiding center — wikipedia, the free encyclopedia, 2016. [Online; accessed 30-April-2017].

[Wik17a] Wikipedia. Standard model — wikipedia, the free encyclopedia, 2017. [Online; accessed 21-April-2017].

[Wik17b] Wikipedia. Trilinear interpolation — wikipedia, the free encyclopedia, 2017. [Online; accessed 20-February-2017].

[Yu79] Ming L. Yu. Observation of positive and negative oxygen ions during electron bombardment of oxygen-covered Mo (100) surfaces. *Physical Review B*, 19(12):5995–6000, jun 1979.

[ZBvdG+00] O Zimmer, J Byrne, M.G.D van der Grinten, W Heil, and F Glück. "aspect" – a new spectrometer for the measurement of the angular correlation coefficient a in neutron beta decay. *Nuclear Instruments and Methods in Physics Research Section A: Accelerators, Spectrometers, Detectors and Associated Equipment*, 440(3):548–556, feb 2000.

[ZPZ+10] Kh. Zakeri, T.R.F. Peixoto, Y. Zhang, J. Prokop, and J. Kirschner. On the preparation of clean tungsten single crystals. *Surface Science*, 604(2):L1 – L3, 2010.

[Zwe64] G. Zweig. An SU(3) model for strong interaction symmetry and its breaking. Version 2. In D.B. Lichtenberg and Simon Peter Rosen, editors, *Developments in the quark theory of hadrons. Vol 1. 1964 - 1978*, pages 22–101. 1964.

[ZWG93] Y.B. Zhao, J.E. Whitten, and R. Gomer. Electron stimulated desorption of hydrogen from w(110). *Surface Science*, 286(3):290–296, may 1993.

[ZYY+14] Xiao-Xin Zhang, Qing-Zhi Yan, Chun-Tian Yang, Tong-Nian Wang, Min Xia, and Chang-Chun Ge. Recrystallization temperature of tungsten with different deformation degrees. *Rare Metals*, 35(7):566–570, jun 2014.